THESIS FOR DEGREE OF DOCTOR OF PHILOSOPHY

High Temperature Oxidation and Chlorination of FeCrAl Alloys

Niklas Israelsson

Department of Chemical and Biological Engineering

CHALMERS UNIVERSITY OF TECHNOLOGY

Göteborg, Sweden 2014

Cover:

STEM-HAADF micrograph of a cross-section of a pre-oxidized FeCrAl alloy exposed at $O_2 + H_2O + KCl$ at 600 °C.

Abstract

The constant strive for improved efficiency and lower-cost industrial processes often results in progressively higher temperatures and more aggressive environments. High-temperature corrosion is a well-known problem in biomass- and waste-fired boilers and is one of the obstacles to overcome in achieving a more sustainable society. Alkali- and chlorine- induced corrosion of chromia-forming alloys has been studied by several researchers. However, the literature is scarce on how alumina forming-alloys, e.g. FeCrAl alloys, perform in such an aggressive environment. In this thesis, the KCl-induced corrosion of FeCrAl alloys is studied through well-planned laboratory exposures, detailed analyses and corrosion tests in a full scale waste-fired power boiler.

In the laboratory, the effect of adding small amounts of KCl was investigated on polished FeCrAl samples in O_2 or $O_2 + H_2O$ environments up to 168 hours at 600 °C. Pre-formed alumina scales were prepared on the alloy substrate through pre-oxidation at various conditions. The pre-treated samples were subsequently exposed to $O_2 + H_2O + KCl$ in order to investigate their corrosion resistance. The samples were analysed using TGA, SEM/EDX, XRD, IC, AES, SIMS, BIB cross sections and STEM/EDX. In order to evaluate the validity of the findings in the laboratory studies, corrosion tests were carried out in a full-scale combined heat and power (CHP) boiler.

The study showed that KCl-induced corrosion caused a rapidly growing iron-chromium-rich oxide to form in O_2 and $O_2 + H_2O$ environments at 600 °C. Chromate formation and alloy chlorination were found to initiate the formation of a non-protective oxide scale. Alloy chlorination was greater in O_2 than in $O_2 + H_2O$ resulting in a more porous scale with poor adhesion to the alloy substrate.

Pre-treating the alloy prior to exposure to $O_2 + H_2O + KCl$ mitigated the corrosion, since alumina, itself, is rather inert towards corrosion. However, the corrosion started locally, most likely at flaws/cracks in the alumina scale and then spread laterally until the entire surface suffered from breakaway corrosion. Similar results were obtained in the corrosion tests in the waste-fired boiler. The pre-formed alumina scale failed after only 24 hours in the boiler at both 600 and 700 °C.

Keywords: FeCrAl, high-temperature corrosion, KCl, H_2O, pre-oxidation, kinetics

List of publications

This thesis is primarily based on the following papers, referred to by roman numerals in the text.

Paper I

N. Israelsson, K. Hellström, J-E. Svensson and L.-G. Johansson

KCl-Induced Corrosion of the FeCrAl Alloy Kanthal® AF at 600 °C and the Effect of H_2O

Published online in Oxidation of Metals

Paper II

N. Israelsson, J. Engkvist, K. Hellström, M. Halvarsson, J-E. Svensson and L.-G. Johansson

KCl-Induced Corrosion of an FeCrAl Alloy at 600 °C in $O_2 + H_2O$ Environment: The Effect of Pre-oxidation

Published online in Oxidation of Metals

Paper III

N. Israelsson, K.A. Unocic, T. Jonsson, M. Norell, K. Hellström, J-E. Svensson and L.-G. Johansson

A Microstructural and Kinetic Investigation of the KCl-Induced Corrosion of an FeCrAl Alloy at 600 °C

Submitted to Corrosion Science

Paper IV

K. Hellström, N. Israelsson, M. Halvarsson, S. Canovic, J-E. Svensson and L.-G. Johansson

The oxide scales formed on a dispersion-strengthened powder metallurgical FeCrAl alloy at 900 °C in O_2 and $O_2 + H_2O$

Submitted to Oxidations of Metals

Paper V

K. Hellström, N. Israelsson, N. Mortazavi, S. Canovic, M. Halvarsson, J-E. Svensson and L.-G. Johansson

Oxidation of a dispersion-strengthened powder metallurgical FeCrAl alloy in the presence of O_2 at 1100 °C: The influence of water vapour

Submitted to Oxidations of Metals

Paper VI

N. Israelsson, K.A. Unocic, K. Hellström, J-E. Svensson and L.-G. Johansson

Cyclic Corrosion and Chlorination of an FeCrAl Alloy in the Presence of KCl

Submitted to Corrosion Science

Paper VII

N. Israelsson, K. Hellström, J-E. Svensson and L.-G. Johansson

High-Temperature Corrosion of an FeCrAl Alloy in a Waste-Fired CHP Boiler

Manuscript

Statement of author's contribution

My contribution to the above papers was the following:

Paper I: I performed the TG exposures, XRD and prepared BIB cross-sections and performed the subsequent SEM/EDX analyses. I evaluated all data, prepared the figures and wrote the paper with the assistance of mainly L.-G. Johansson.

Paper II: I performed all of the experimental and analytical work except the AES and SIMS analyses which Josefine Hall did. I evaluated all data (with the exception of AES and SIMS), prepared the figures and wrote the paper with the assistance of mainly L.-G. Johansson.

Paper III: I performed the TG exposures, XRD, BIB cross-sections, SEM/EDX and some of the TEM lift outs, and analysed all the data (with the exception of AES). I prepared all the figures and wrote the paper with the assistance of mainly L.-G. Johansson.

Paper IV: I performed the TG exposures, prepared the figures and was took part in writing and finalizing the article.

Paper V: I performed the TG exposures, prepared the figures and took part in writing and finalizing the article.

Paper VI: I performed the XRD, BIB cross-sections, SEM/EDX and analysed all the data (including STEM/EDS). I prepared the figures and wrote the paper with the assistance of L.-G. Johansson.

Paper VII: I performed the XRD analyses and SEM/EDX of the prepared cross-sections. I analysed the data, prepared the figures and wrote the paper with the assistance of J.-E. Svensson and L.-G. Johansson.

Related work

J. Engkvist, N. Israelsson and U. Bexell
The initial effect of KCl deposit on alumina scales characterized by ToF-SIMS and AES

Proceedings of Surface and Interface Analysis, 29 May 2012, DOI 10.1002/sia.5081

The following reports have been published online but are not included in the thesis.

J. Pettersson, J-E. Svensson, E. Skog, L-G. Johansson, N. Folkesson, J. Froitzheim, S. Karlsson, E. Larsson, N. Israelsson, S. Enestam, J. Tuiremo, A. Jonasson, B. Arnesson, B-Å. Andersson, B. Heikne
KME report, Project KME-411 (2010)
Evaluation of different fuel additives' ability to master corrosion and deposition on steam superheaters in a waste-fired CFB-boiler

J-E. Svensson, L-G. Johansson, K. Hellström, J. Pettersson, N. Israelsson, B. Jönsson, D. Chandrasekaran, R. Norling
KME report, Project KME-414 (2010)
FeCrAl alloys for superheaters in biomass- and waste-fired boilers: A feasibility study

K. Hellström, N. Israelsson, J-E. Svensson, B. Jönsson, D. Chandrasekaran, J. Nockert-Olovsjö, A. Jonasson, B-Å. Andersson, P. Cho, P. Kallner, P. Henderson
KME report, Project KME-507 (2014)
FeCrAl alloys as components in biomass- and waste- fired boilers

Preface

This thesis summarizes the research carried out within the Swedish Competence Centre for High Temperature Corrosion (HTC), from 2010-2014. The work was performed at Environmental Inorganic Chemistry at the Department of Chemical and Biological Engineering, Chalmers University of Technology, Gothenburg, Sweden, under the supervision of Professor Jan-Erik Svensson and Lars-Gunnar Johansson. The work was funded by HTC, Sandvik Heating Technology and the Swedish Energy Agency.

List of acronyms

TGA	Thermo gravimetric analysis
XRD	X-ray diffraction
AES	Auger electron spectroscopy
Tof-SIMS	Time of flight-secondary ion mass spectrometry
IC	Ion chromatography
BIB	Broad ion beam
FIB	Focused ion beam
SEM	Scanning electron microscopy
BSE	Backscattered electron
SE	Secondary electron
EDX	Energy dispersive X-ray
TEM	Transmission electron microscopy
STEM	Scanning transmission electron microscopy
BF	Bright-field
HAADF	High angle annular dark field
t-EBSD	Transmission-electron backscattered diffraction

Table of contents

1 Introduction

The constant strive for improved efficiency and lower-cost industrial processes often results in progressively higher temperatures and more aggressive environments. High-temperature corrosion is a well-known problem in several industrial applications and is one of the obstacles to overcome in achieving a more sustainable society. During the past decade, development has moved towards lowering fossil fuel dependency, and, consequently, renewable fuels, such as biomass and waste, have become attractive options to fossil fuel for power production. There is also an economic benefit from burning waste since the fuel is inexpensive. The energy companies actually get paid to handle domestic waste, which then can then be converted into electricity and district heating. In addition some countries, e.g. Sweden, have economic incentives in order to increase the energy output of renewable energy.

Higher costs are, however, involved in using biomass and waste as fuels in power boilers. Burning biomass and waste results in a more corrosive fireside environment, that contains more alkali chloride and water than fossil fuels [1-9]. Consequently, the corrosion of critical components in a power boiler, e.g. the superheater tubes, is a major challenge. To mitigate corrosion problems, the maximum steam temperature is kept relatively low (typically 350-550 °C depending on the fuel). To increase the competitiveness of this power source, higher operating temperatures are needed, which creates demands for new materials that can cope with such an aggressive environment.

Currently, low-alloyed steels and stainless steels are the material of choice for use in power boilers. The ability of these alloys to withstand high temperatures relies on the formation of a protective, Cr-rich oxide $(Cr,Fe)_2O_3$. Previous studies have shown that certain chemical reactions consume the protective chromia scale and leave a poorly protective iron oxide behind [10-16]. This may result in a sudden increase in the rate of corrosion (breakaway corrosion).

A possible strategy to avoid component failure in a power boiler would be to use a different type of material. FeCrAl alloys are well-known for their good oxidation resistance at elevated temperatures and might be a suitable candidate. FeCrAl alloys form a highly protective alumina scale at higher temperatures which is more protective than the chromia scale formed on stainless steels.

1

1.1 Aim of thesis

The aim of this study is to generate new insights into the oxidation and corrosion of FeCrAl alloys in biomass- and waste-firing environments. KCl-induced corrosion of FeCrAl alloys was investigated at 600 °C. The selected temperature is higher than today's operating temperatures and was chosen to meet the increasing demand from industry.

2 FeCrAl alloys

FeCrAl alloys are ferritic body-centred cubic (bcc) iron-based alloys with approximately 20 wt. % Cr and 1-5 wt. % Al (Fig. 2.1). FeCrAl alloys are primarily used at high temperatures (900-1300 °C) such as heating elements in industrial furnaces, gas burner mats and industrial furnace furniture. The superior oxidation resistance of FeCrAl alloys at higher temperature relies on the formation of a slowly growing and highly protective α-Al$_2$O$_3$ scale. A common view is that α-Al$_2$O$_3$ forms on FeCrAl alloys at temperatures exceeding 1000 °C [17] (see Section 4.3).

Binary solutions of FeAl can also form a protective alumina scale, but if chromium is added to the FeAl matrix the amount of aluminium can be lowered in the alloy and still form an α-Al$_2$O$_3$ scale at elevated temperatures [18]. A lower aluminium content in the FeCrAl alloy also improves its ductility, which is important in processing the alloy into the final product [19].

Minor amounts of reactive elements (RE´s), e.g. Y, Hf, Zr and Ce are usually mixed into FeCrAl alloys to improve oxidation properties at elevated temperatures [19, 20]. The effects of adding reactive elements to FeCrAl alloys will be further discussed in Section 4.4.
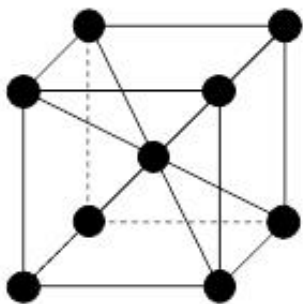
Figure 2.1 Unit cell for ferrite (bcc).

3 Oxidation theory

Metals and alloys are thermodynamically unstable in most conditions, and, depending on the environment, oxides, nitrides, sulphides and chlorides may form. Temperature is an important factor in this process since the rate of the reactions increases with temperature [18]. The corrosion resistance of alloys is of great importance at elevated temperatures in order to avoid component failure. The corrosion resistance of an alloy relies on the formation of a well-adherent and protective oxide scale on the alloy surface.

3.1 Oxide formation and thermodynamics

The oxidation reaction of a metal M and oxygen gas O_2 may be written as:

$$xM(s) + \frac{y}{2}O_2(g) \leftrightarrow M_xO_y(s) \tag{1}$$

The second law of thermodynamics can be used in order to determine if a reaction (e.g. Reaction (1)) will occur or not. During constant temperature and pressure it is often written in terms of Gibbs free energy (G') of a system (2),

$$G' = H' - TS' \tag{2}$$

where H' is the enthalpy and S' is the entropy of a system. At the above conditions a negative value for $\Delta G'$ reveals that a certain reaction is spontaneous, $\Delta G' > 0$ is thermodynamically impossible and an equilibrium condition prevails when $\Delta G' = 0$ [21]. $\Delta G'$ may be expressed as (3) for the chemical Reaction (1)

$$\Delta G' = \Delta G° + RT\ln(\ a_{M_xO_y}/a_M^{\ x}\ a_{O_2}^{\ y/2}) \tag{3}$$

where $\Delta G°$ is the standard free energy change, R is the gas constant, T is the temperature and a represents the thermodynamic activities of products and reactants which describe the deviation from their standard states. The activity of a specie can also be expressed as (4)

$$a_x = p_x\ /\ p_x° \tag{4}$$

where p_x is the vapour pressure of a condensed liquid or the partial pressure of a gaseous specie and $p_x°$ corresponds to the same as p_x but at its standard state.

The standard Gibbs free energy $\Delta G°$ for Reaction (1) can be calculated using the standard molar-free energies of formation for the species involved (Reaction (5)) [21].

$$\Delta G° = G°_{M_xO_y} - xG°_M - \frac{y}{2} G°_{O_2} \tag{5}$$

At equilibrium conditions Reaction (3) reduces to (6) since $\Delta G' = 0$ where K is the equilibrium constant.

$$\Delta G° = - RTln(\ a_{M_xO_y}/a_M{}^x a_{O_2}{}^{y/2}) = -RTln(K) \tag{6}$$

Reaction (7) is of great importance to electrochemical reactions where F is the Faraday constant, n equals the number of electrons involved in a certain reaction and $E°$ is the standard cell potential which expresses $\Delta G°$ in terms of potential in volts.

$$\Delta G° = -nFE° \tag{7}$$

If the change in Gibbs free energy is < 0 for a system, then an oxide will form on a metal surface according to Reaction (1). The initial steps in the oxidation process are illustrated in Figure 3.1.
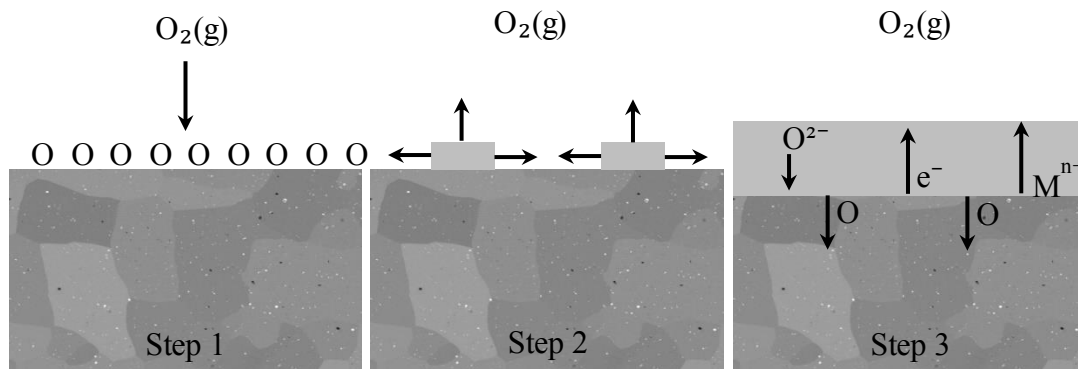
Figure 3.1 The initial formation of an oxide scale.

1. In the first step, gas molecules e.g. O_2 or H_2O from the surrounding environment adsorb on the metal surface. The gas molecule, e.g. O_2, then dissociates into absorbed O on the metal surface.

2. The absorbed O attracts electrons and becomes first chemisorbed and finally forms oxide nuclei on the metal surface, which grow laterally to form a continuous oxide film [21]. Several factors determine the adsorption and the

initial oxide formation. Some of these are surface preparation, crystal defects, temperature and impurities.

3. The oxide film formed in step 2 acts as a barrier and separates the metal from the gas. For further oxidation to occur, metal or oxygen ions must be transported by solid-state diffusion through the film. The oxide will grow mostly outward or inward depending on which specie (oxygen or metal ions) that dominates the transport through the oxide scale. The driving force for thin oxide films may be electric fields in or across the film, and for thick oxide scales, the driving force is the gradient in the chemical potential [17].

Oxidation of alloys involves the same steps as described above for pure metals. Since an alloy consists of several elements, the oxidation mechanism becomes more complex. The relative amounts between the elements, their potential to diffuse and their affinity to oxygen, will determine which type of oxide that forms [17].

In the case of an alloy containing two elements, an oxide film with both elements will form initially. Different types of oxides usually have different growth rates which results in that one of them overgrows the other. During prolonged exposures, a displacement reaction may occur (see Reaction (8)). The less noble element B will react with the metal oxide including the nobler element A.

$$B \text{ (in alloy)} + AO \rightarrow BO + A \text{ (in alloy)} \qquad (8)$$
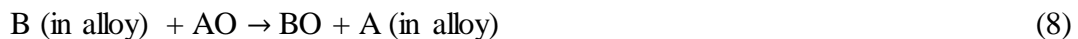
At high concentrations of B, an oxide of pure BO will form, and at very low concentrations an oxide scale of pure AO will be present. A third scenario may occur with intermediate compositions of A and B. Then both AO and BO will be formed simultaneously. Depending on the oxide properties, a mixture of AO and BO may form. AO and BO can be miscible and form a solid solution. AO and BO may also be partly or totally immiscible [17].

3.2 Defects

All crystalline materials contain defects at all temperatures and these defects are needed in order to transport ions and electrons through the oxide scale. A point defect is an imperfection in the crystal structure and is limited to one structural or lattice site. Defects of this type are vacancies and interstitial atoms, which are located between

the regular sites [17]. Foreign atoms, e.g. impurities, are also considered to be point defects. Several point defects may cluster and form larger defect structures. Edge dislocations also occur in crystalline materials when a plane of atoms is terminated in the middle of a crystal. Planar defects comprise stacking faults, e.g. when two crystals with different orientations grow and merge together forming a grain boundary. Nonstoichiometric crystals, e.g. oxides, also contain electronic defects. These consist of electrons and electron holes, which are quite mobile in a crystal.

If a nonstoichiometric oxide is oxygen deficient and the dominating defects are single-point defects, these will form oxygen vacancies. On the other hand interstitial ions will dominate if metal excess exists in the oxide. The positive effect charge build up is cancelled out by the formation of electrons. The above type of oxide is called a negative semiconductor.

If a nonstoichiometric oxide with a metal deficit or excess oxygen is considered, the dominating defects will be metal vacancies and oxygen interstitials. The defects will have negative effective charges which are compensated through the formation of positive electron holes [17, 21]. This type of oxide is called a positive semiconductor.

3.3 Diffusion

As mentioned above, ions and electrons need to be transported through the oxide film by solid-state diffusion if further oxidation is to take place. This could occur through either lattice diffusion (Fig. 3.2) or through grain boundary diffusion.
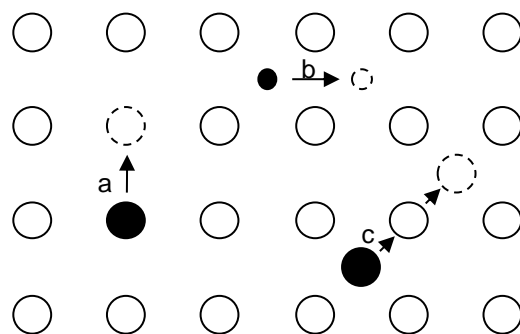
Figure 3.2 Different kinds of lattice diffusion; a) vacancy diffusion, b) interstitial diffusion and c) interstitialcy diffusion [22].

In reality, no oxide film is perfectly dense and micro cracks, or porosity, will contribute to the transport of species through the scale. The grain size in metal oxides can vary greatly from < 100 nm to several μm. Due to this small grain size the total amount of grain boundaries stands for quite a considerable part of the oxide scale. As an example the estimated area of grain boundaries was 5-10 % of the formed oxide on titanium at 500 °C [17]. Grain boundary diffusion is usually dominant at lower temperatures since the activation energy for diffusion along grain boundaries is lower than for lattice diffusion [18]. The oxide grains are also smaller at lower temperatures which will increase the number of grain boundaries. At higher temperatures the oxide grains coarsen and fewer easy diffusion paths are available. The coefficients for lattice diffusion also increase more than the corresponding coefficient for grain boundary diffusion which results in a more homogeneous diffusion at elevated temperatures.

3.4 Oxidation kinetics

Throughout the oxidation of metals and alloys, a weight gain occurs due to oxide formation. The oxidation rate is often described by three different rate equations: parabolic, linear and logarithmic (Fig. 3.3).
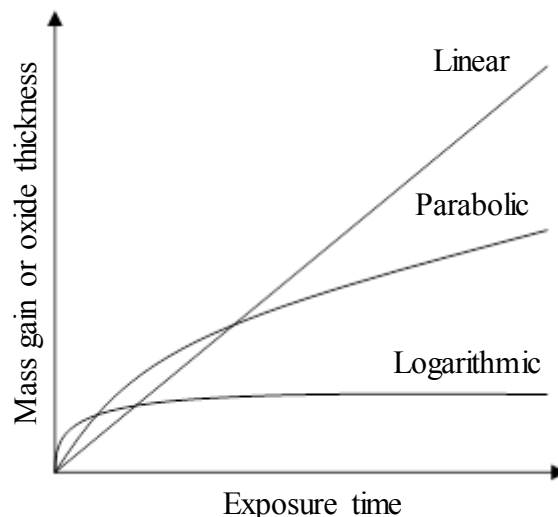
Figure 3.3 Oxidation kinetics for three common rate equations.

Knowledge of reaction rates and kinetics is important in corrosion research, to obtain information about the reaction mechanisms present. The rate equation alone is not enough to figure out which oxidation mechanism is present, but it can be a way of

excluding some alternative mechanisms. Reaction rates and related rate equations depend on several features such as oxygen partial pressure, surface preparation, pre-treatment of the metal/alloy, exposure time and temperature. The kinetics in Figure 3.3 only represents limiting and ideal cases. Usually a combination of different rate equations are needed in order to describe the total oxidation process [17].

3.4.1 Linear rate equation

In some cases the oxidation of metals/alloys proceeds at a constant rate and a linear kinetics is observed (Fig. 3.3).

The linear kinetics is expressed as:

$$\frac{dx}{dt} = k$$

$$x = k_l t + C \tag{9}$$

where x = oxide thickness (which is often assumed to be equal to the measured weight gain), t = time, k_l = linear rate constant and C = integration constant. It is often assumed that x = 0 at t = 0 which gives C = 0. Linear oxidation behaviour is usually observed when the rate-determining step of the oxidation process occurs at the oxide/gas interphase (see Reaction (10) for O_2) [21].

$$O_2\,(g) \rightarrow O_2\,(adsorbed) \rightarrow 2O\,(adsorbed) \xrightarrow{2e^-} 2O^-\,(chemisorbed) \xrightarrow{2e^-} 2O_2^-\,(lattice) \tag{10}$$
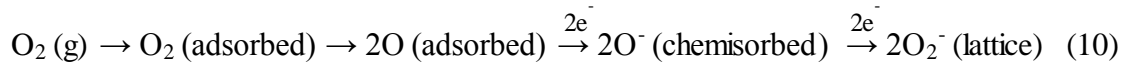
As long as the diffusion through the oxide scale is rapid, the above process will be the rate-determining step. This often occurs when the oxide scale is thin and the oxygen partial pressure is relatively low. High temperature also promotes linear oxidation behaviour.

3.4.2 Parabolic rate equation

At elevated temperatures, the oxidation of many metals/alloys follows the parabolic rate equation. Equation (11) shows the differential and integral forms of the parabolic rate equation.

$$\frac{dx}{dt} = k_p'/x$$

$$x^2 = k_p t + C \tag{11}$$

The latter equation shows that the square of film thickness x, is proportional to time t. C is the integration constant, k_p' and k_p are the parabolic rate constants which are directly proportional to the diffusivity of the rate-controlling ionic species [17]. The formed oxide on the metal surface separates the gas and the metal. As the oxide scale thickens, the diffusion distance increases and the reaction rate declines with time.

Carl Wagner described the above kinetic reaction in the 1930s and the basic assumption was that the lattice diffusion of atoms, ions or electrons through the scale was rate determining in the overall oxidation reaction. The reactions are rapid at the phase boundaries and thermodynamic equilibrium is established between the metal/oxide and the oxide/gas interface. The main driving force for oxidation is the change in free energy which occurs when oxygen reacts with metal to form an oxide (see Section 3.1). A gradient of the oxygen partial pressure exists throughout the oxide scale with a higher partial pressure at the oxide/gas interface. The partial pressure at the metal/oxide interface is so low that it corresponds to the decomposition pressure of the oxide in equilibrium with its metal [17, 21].

3.4.3 Logarithmic rate equation

Logarithmic rate behaviour is applicable at low temperatures, generally below 300-400 °C. Initially, the reaction is rapid and then fades out to low or insignificant oxidation rates. There are two equations that describe this behaviour:

Direct logarithmic: $x = k\log(t + t_0) + A$ (12)

Inverse logarithmic: $\frac{1}{x} = B - k_{il}\log(t)$ (13)

x often represents the thickness of the oxide film but it can also be the amount of metal transformed into oxide or the amount of consumed oxygen per unit surface area. A and B are constants, k and k_{il} are rate constants and t denotes time. The rate determining step is believed to be the transport of electrons or ions from the metal through the oxide to the adsorbed oxygen atoms at the sample surface. Other theories are rate-determining chemisorptions or the formation of cavities in the oxide film [17].

4 High-temperature oxides formed on FeCrAl alloys

All elements may oxidise in an FeCrAl alloy depending on temperature and exposure environment. Initially (during heating) all elements present at the alloy surface will oxidise and form a mixed oxide scale called transient oxide. Different oxides will form depending on the application temperature. Lower temperatures favour the formation of oxides of iron and chromium since the aluminium diffusion is slow and the alumina content is often low (1-5 %) in the alloy. Amorphous Al_2O_3 forms on FeCrAl alloys at temperatures up to 500 °C [21, 23] and at higher temperatures crystalline Al_2O_3 forms, which supresses the partial pressure of oxygen which, later in the oxidation process, may rule out the formation of iron and chromium oxides.

4.1 Iron oxides

When iron is exposed to an oxidizing environment at 600 °C, an oxide film is formed consisting of a mixture of three different oxides, FeO, Fe_3O_4 and Fe_2O_3. The oxide film grows through the outward diffusion of iron, and FeO is located closest to the metal surface and Fe_2O_3 as the outermost layer.

Wüstite, FeO, is highly non-stoichiometric and the high number of cationic vacancies results in the high mobility of cations and electrons via metal vacancies and electron holes. This behaviour makes FeO a p-type semiconductor and it is considered to be a non-protective oxide with an NaCl crystal structure [21].

Magnetite, Fe_3O_4, is more corrosion resistant than FeO and has an inverse spinel crystal structure. This oxide is close to stoichiometric and behaves as a p-type semiconductor with cations diffusing outwards.

Hematite, α-Fe_2O_3, is the most protective iron oxide. Its corundum structure consists of a hexagonal packing of oxygen ions with iron ions that occupy two thirds of the octahedral sites [21]. Hematite is an n-type semiconductor at temperatures between 650-800 °C and a p-type at higher temperatures [17].

4.2 Chromium oxides

Cr_2O_3 is the only stable oxide that forms when chromium is oxidised at elevated temperatures. It has a corundum structure and is miscible with α-Fe_2O_3 and α-Al_2O_3. The protective properties of Cr_2O_3 are especially beneficial at higher temperatures

because its solid state diffusion is very slow. Cr_2O_3 is considered to be a p-type semiconductor with cation vacancies as being the dominant defects [17].

4.3 Aluminium oxides

Al_2O_3 exists in various forms but only α-Al_2O_3 is thermodynamically stable [23]. Other forms of alumina often form at lower temperatures, e.g. γ, δ and θ-Al_2O_3 (Fig. 4.1).
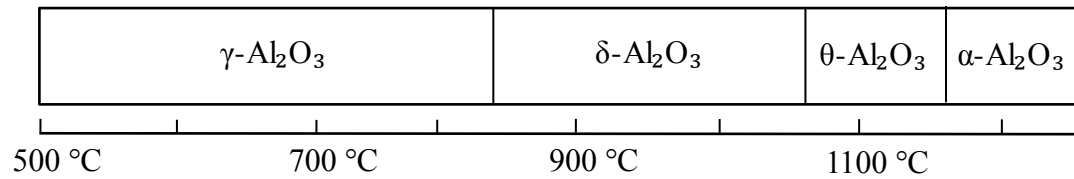
Figure 4.1 Observed transformation temperatures for bulk material of γ-Al_2O_3 [23].

All forms of alumina, except α-Al_2O_3, are termed transient alumina's and are thermodynamically unstable, fast-growing and have fairly poor protective properties. The transient oxides are commonly observed at lower temperatures and may transform to α-Al_2O_3 with time or at higher temperatures since they are metastable [18, 24]. Depending on what substrate the alumina grows on, the phase transformations and temperatures when they occur (see Fig. 4.1), may differ. The addition of 3 % platinum to γ-Al_2O_3 in Figure 4.1 resulted in no formation of δ-Al_2O_3. Instead γ-Al_2O_3 transformed to θ-Al_2O_3 directly at roughly 800 °C [23]. The alumina formation on a FeCrAl alloy is slightly different from the one described in Fig. 4.1 since several additions, such as reactive elements, are present in the alloy (see Section 4.4).

The initial formation of Cr_2O_3 and α-Fe_2O_3 during the oxidation of FeCrAl alloys favours the nucleation of α-Al_2O_3 since all of the oxides have the corundum structure [19]. John Stringer, Wilcox and Jaffee have reported that oxidised RE particles in chromia-forming alloys govern the nucleation of Cr_2O_3 [25], which in turn may ease the formation of α-Al_2O_3 on FeCrAl alloys. Other reports show that an RE, e.g. yttrium, retards the transformation from θ to α-Al_2O_3 [18, 19].

The crystal structure of α-Al_2O_3 consists of oxygen ions that are hexagonally close-packed with two thirds occupied by aluminium ions. α- Al_2O_3 is highly stoichiometric due to its high band gap and high lattice energy. This makes the defect concentration

14

very low and the transport paths for oxygen and metal ions are limited [17]. These properties result in high corrosion resistance even at elevated temperatures. Alumina is more stable than chromia and does not suffer from evaporation at higher temperatures as chromia does. The general opinion about the oxidation of FeCrAl alloys is that α-Al$_2$O$_3$ forms at about 1000 °C [17, 26, 27]. Tatlock *et al.* [28] have detected both transient alumina and α-Al$_2$O$_3$ with XRD after exposing FeCrAl alloys at 800-900 °C, the proportion of transient alumina decreased with higher exposure temperature, and after exposure at 950 °C only α-Al$_2$O$_3$ was detected. Nicholls *et al.* [29] have observed a two-layered alumina scale formed after oxidation at 800 °C with an outward growing transient alumina layer and an inward growing alumina layer which was interpreted as α-Al$_2$O$_3$. In addition Josefsson *et al.* [30] have shown evidence of the formation of α-Al$_2$O$_3$ on FeCrAl alloys after 168 hours in dry O$_2$ at 700 °C.

4.4 The RE effect on Al$_2$O$_3$ forming alloys

Alumina scales are often susceptible to spallation and mechanical failure induced by e.g. growth stresses and thermal stresses. In order to improve the scale properties, small amounts (0.01-0.5 wt. %) of reactive elements (RE's, *e.g.*, Y, Zr, Hf, La) can be added to FeCrAl alloys, as mentioned above. The reactive element effect was first discovered in 1937 by L. B. Pfeil and has since then been extensively studied by several researchers. Many of the reported results are covered in reviews by Whittle and Stringer [20], Quadakkers and Singheiser [31], Pint [32], Hou [33] and Chevalier [34].

Below follows the core findings of the review article by Peggy Y Hou [33]. The reactive element effect can be summarized as follows: RE enhances the selective oxidation of aluminium, RE reduces the rate of scale growth, RE reduces the outward diffusion of Al^{3+}, RE improves the adhesion of an alumina scale to the alloy.

4.4.1 Enhanced selective oxidation

The enhanced selective oxidation of aluminium on FeCrAl alloys means that a protective alumina scale can form faster than without the addition of an RE. The amount of Al necessary to develop the protective alumina scale could also be reduced in the alloy. RE or RE oxide addition alters the microstructure of the alloy substrate. The alloy grain size decreases and the dislocations increase. In addition Pint, Garratt-

Reed and Hobbs [35] have discovered that subgrain structures were created when RE oxide dispersion was used, which further enhanced the diffusion of aluminium to the surface.

4.4.2 Reduced growth rate

RE addition has been observed to reduce the growth rate of α-Al_2O_3 by at least a factor of 2 [36].

4.4.3 Reduced outward diffusion of Al^{3+}

Two-stage oxidation tests on FeCrAl alloys using oxygen isotopes have shown that RE addition reduces the outward diffusion of Al^{3+} through the alumina scale, but does not seem to affect the inward diffusion of O^{2-}. Several researchers have observed that RE segregates to the alumina grain boundaries in the scale and also accumulates at the scale/gas interface. This segregation has been observed for RE added to alloys both in metallic form and as oxide dispersions. The segregated RE amount in the alumina grain boundaries has been quantified to be about 0.2 monolayer [33]. In addition, high resolution TEM studies by Buban *et al.* [37] and first principal calculations on simplified alumina grain boundaries by Milas, Hinnenmann and Carter [38] suggest that Y and Hf would segregate to Al grain boundary sites, and, consequently, hinder the outward transport of Al^{3+} but not the inward transport of O^{2-}.

4.4.4 Improved scale adhesion

The low amount of sulphur often present in alloys (about 3-30 ppm) diffuses to the alumina/alloy interface during oxidation if RE is absent in the alloy [39]. This is generally referred to as the "sulphur effect" [40, 41] and was first observed on chromia-forming alloys weakening the bond between the scale and alloy, often leading to spallation. Reactive elements are strong sulphide formers, thus the addition of RE to alloys lowers the amount of "free" sulphur in the alloy; thereby preventing it from segregating to the interface. The RE addition has also been reported to reduce the formation of voids at the alloy/oxide interface, contributing to increased adhesion of the scale [33].

5 The effect of H₂O and chlorine-containing species on high temperature corrosion

As mentioned in the introduction, biomass and waste contain more water- and chlorine-containing species than fossil fuel, which influences the corrosion [1-9]. Severe corrosion attacks have been recorded shortly after switching the fuel from coal to biomass/waste. Superheaters and water walls, in particular, suffer from fireside corrosion. This corrosive environment results in lower operating temperatures in order to increase the lifetime of the superheaters. While coal-fired power boilers operate at maximum steam temperatures of about 650 °C, the maximum steam temperatures are considerably lower in biomass- and waste-fired boilers, (~550 °C) and (~450 °C) respectively [42].

The flue gas becomes rather different when using waste and biomass as a fuel compared to coal. This is not so surprising since the composition of the fuels differ significantly. In general, the water vapour content, HCl(g), KCl(g), NaCl(g) increases, while the SO_2(g) content is reduced when the fuel is shifted from coal to biomass and waste.

5.1 The effect of H₂O on the oxidation of FeCr, FeCrNi and FeCrAl

Water vapour has a significant effect on the oxidation behaviour of chromia-forming steels. Some common observations include increased oxidation and a breakdown of the protective scale. There are different theories about the course of events in this process, but one theory connects the breakdown of the protective scale with the formation of chromic acid [43]. Chromia reacts with oxygen and water to form chromic acid according to Reaction (14). With time Reaction (14) will deplete the protective oxide scale of chromia and leave behind a poorly protective Fe_2O_3 scale. Reaction (14) is significant at temperatures as low as 600 °C.

$$^1/_2Cr_2O_3(s) + {}^3/_4O_2(g) + H_2O(g) \rightarrow CrO_2(OH)_2(g) \tag{14}$$
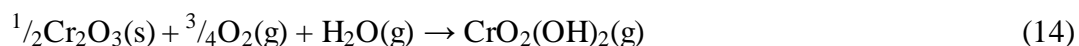
The literature is scarce on how water vapour influences the oxidation of FeCrAl alloys at 600 °C. Liu *et al.* [44] have nevertheless, shown that water vapour accelerates the mass gain of an FeCrAl alloy at 900 °C. A two-layered α-Al₂O₃ scale formed in dry O₂ while an inner layer of α-Al₂O₃ and an outer layer of γ-Al₂O₃ formed

in O_2 + H_2O. In other words, water vapour retarded the formation of α-Al_2O_3 at 900 °C.

5.2 Chlorine-induced corrosion on FeCr, FeCrNi, FeCrAl alloys

Chlorine-containing compounds like KCl, NaCl, HCl and Cl_2 are common corrosive species in waste- and biomass- fired boilers [45].

McNallan, Mayer, Rapp, Hupa, Grabke, Spiegel and others (see [45]) have investigated how Cl_2 and HCl influence corrosion in an oxidising environment. They all share one common hypothesis and it is called active oxidation or the chlorine cycle, which states that metal chlorides form at the interface between the alloy and the oxide. Cl_2 or HCl is believed to diffuse through the oxide scale to the alloy/oxide interface and form metal chlorides according to Reaction (15) or (16).

$$x/2\ Cl_2(g) + Me(s) \rightarrow MeCl_x(s) \tag{15}$$

$$Me(s) + xHCl \rightarrow MeCl_x(s) + x/2H_2 \tag{16}$$

Metal chlorides, e.g. $FeCl_2$ and $CrCl_2$, are stable at the alloy/oxide interface since the partial pressure of oxygen is low. The vapour pressure of metal chlorides is however relatively high at elevated temperatures and they are believed to diffuse out to the oxide/gas interface. The metal chlorides will react with oxygen to form metal oxide according to Reaction (17) due to the higher oxygen partial pressure.

$$yMeCl_x(g) + z/2O_2(g) \rightarrow Me_yO_z + xy/2Cl_2(g) \tag{17}$$
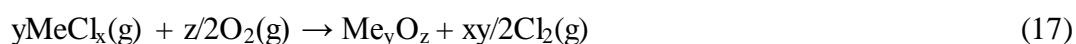
The chlorine formed in the above reaction may then migrate back into the oxide and start a new cycle [46]. The "chlorine cycle" has however some problems like the inward transport of Cl_2 or HCl to the metal/scale interface where low oxygen activity is postulated to prevail. It is argued that the low oxygen activity at the metal/scale interface would be very difficult to maintain, because cracks and pores open to Cl_2 and HCl diffusion must also be open to O_2 diffusion. It is also considered improbable that the highly reactive chlorine molecule would be able to reach the metal/scale interface without being reduced by the oxide *en route* e.g. with Fe^{2+} ions in the scale.

Water vapour will always be present (roughly 20-25 %) together with about 5 % O_2 when using biomass and waste as the fuel in boilers. Even if Cl_2 forms in a boiler

most of it will react with water to form HCl according to the reversed deacon process (Reaction 18) [17].

$$2H_2O(g) + 2Cl_2(g) \rightarrow 4HCl(g) + O_2(g) \tag{18}$$

Several researchers have investigated the effects of solid alkali salts on corrosion. Experiments with KCl have shown that the cat ion K^+ also plays an important role in the breakdown of the protective chromia-rich scale on FeCr, FeCrNi and FeCrAl alloys [14, 15, 47-50]. It has been reported that $K_2CrO_4(s)$ and HCl(g) are formed according to Reaction (19) which depletes the protective Cr-rich $(Cr,Fe)_2O_3$ oxide scale in chromia, resulting in a poorly protective Fe_2O_3 scale.

$$^1/_2Cr_2O_3(s) + {}^3/_4O_2(g) + H_2O(g) + 2KCl(s) \rightarrow K_2CrO_4(s) + 2\ HCl(g) \tag{19}$$
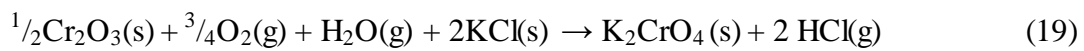
The complex environment in a waste-fired boiler may result in the presence of molten species at the component surfaces. As an example, the melting temperature of pure NaCl and KCl is 801 °C and 772 °C [45] while the eutectic mixture of NaCl-KCl has a lower melting temperature of 657 °C, which could be relevant in this study.

6 Experimental techniques

6.1 The investigated materials

The materials were supplied by Sandvik Heating Technology (see Table 1 for nominal chemical composition). Kanthal® AF and APMT are both commercial ferritic alloys and are in the following pages referred to as alloy AF and alloy APMT.

Table 1. Nominal chemical composition of the investigated alloys.

Element (wt. %)	Cr	Al	Mo	Mn	Si	C	Fe	Re
Kanthal® APMT	21.0	5.0	3.0	≤0.4	≤0.7	≤0.08	bal.	Y,Zr,Hf,Ti
Kanthal® AF	21.0	5.3	-	≤0.4	≤0.7	≤0.08	bal.	Y,Zr

The main difference between the two alloys is how they are produced. Alloy AF is a wrought alloy which is conventionally produced by melting followed by hot-rolling, pickling and cold rolling, giving a grain size of roughly 20 μm. One drawback with alloy AF at higher temperatures is its rather low mechanical strength. This issue is diminished in alloy APMT through the modification of the production route. Dispersion strengthening and grain size control are used in order to increase the mechanical strength of the alloy. Alloy APMT is called a rapidly solidified powder (RSP) alloy and it contains small refractory inclusions of oxides, carbides and nitrides homogeneously dispersed in the FeCrAl matrix [51, 52]. These small inclusions (20-200 nm) prevent grain growth at temperatures up to 1200 °C and allow the grain size of alloy APMTs grain size to be in the range of 10-20 μm (see right image in Fig. 6.1).
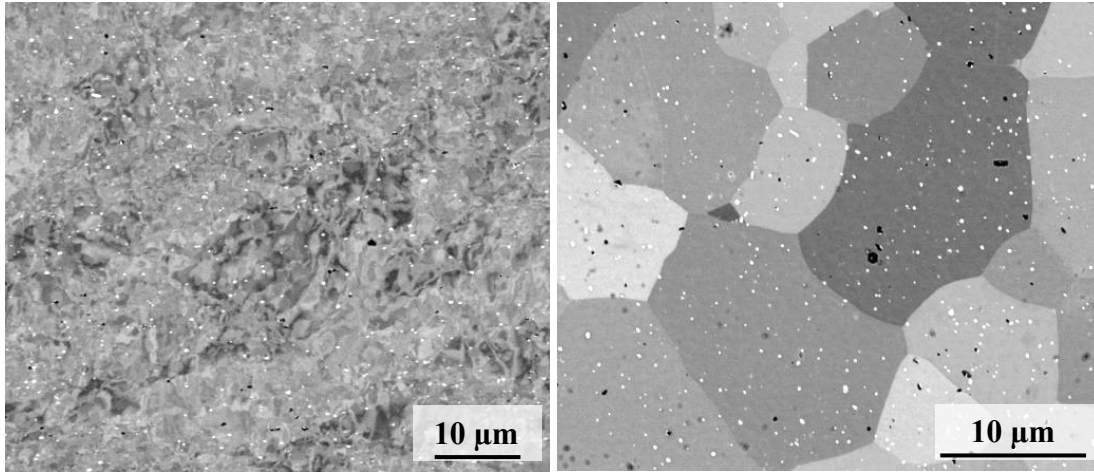
Figure 6.1 SEM-BSE images of unexposed alloy APMT (left image) and alloy APMT exposed to 900 °C for 1 hour in dry O_2 (right image).

These properties give alloy APMT better mechanical strength than alloy AF at elevated temperatures (see Fig. 6.2).
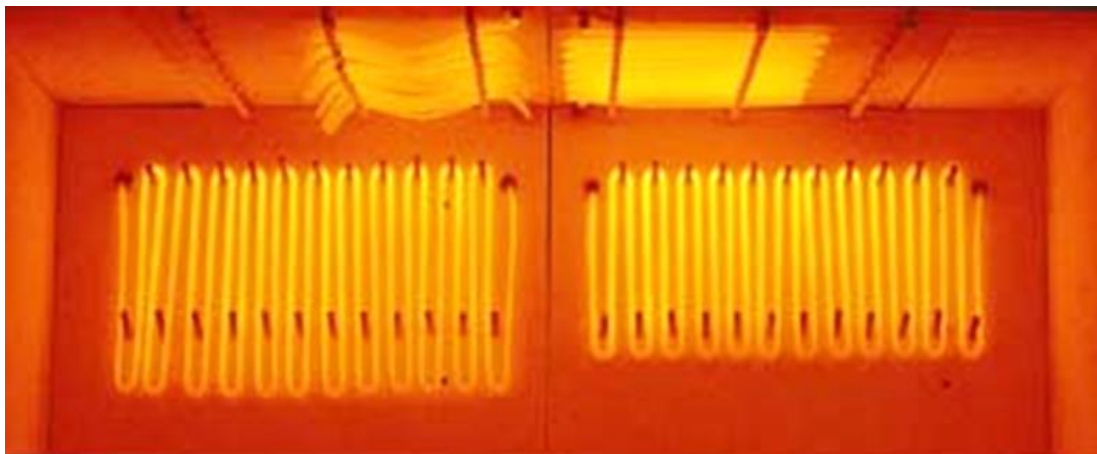
Conventional FeCrAl alloy   RSP FeCrAl alloy

Figure 6.2 Heating wires of conventional (left) and RSP FeCrAl (right) alloys exposed for 500 hours at 1300-1400 °C. Reproduced with permission from Sandvik Heating Technology.

Tubes made of alloy APMT are produced through several steps including melting the raw material, powder production, hot isostatic pressing and hot extrusion as is illustrated in Figure 6.3 [51].

Powder Production-Gas Atomisation	Filling of Capsule	Hot Isostatic Pressing (HIP)	Machining of Billet	Hot Extrusion	Pickling and Pre-oxidation
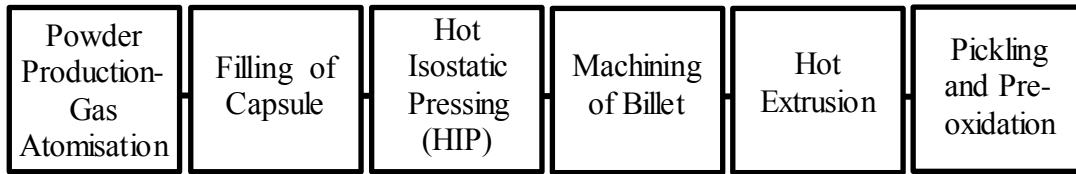
Figure 6.3 Schematic illustration of the production route for alloy APMT tubes [51].

The received APMT alloy was not manufactured according to Figure 6.3. The three first steps in the above described process were the same, however after the hot isostatic pressing the material was hot-rolled into strips. The grain size was very small (≤ 3 μm) in the as-received alloy compared to alloy AF (see Fig. 6.1). Figure 6.1 also shows a cross-section of the alloy substrate of an APMT sample which was exposed to 900 °C for 1 hour in dry O_2. It is clear that the grain size has grown considerably up to 10-20 μm, which could be compared to the last pre-oxidation step in Figure 6.3 in which the alloy had been exposed to 1050 °C for 8 hours.

6.2 Sample preparation

The alloys were delivered by Sandvik Heating Technology as alloy strips which were cut into coupons with the dimensions 15 x 15 x 2 mm^3. A hole (1.5 mm in diameter) was drilled in the samples which would be exposed to the KCl containing environment. The hole was used to hang each sample during the addition of KCl. The samples were ground with 320 grit SiC paper and polished in three steps using a 9, 3 and 1 μm diamond suspension. The samples were degreased and cleaned using ultrasonic agitation in water, acetone and ethanol. The polished samples were dried with flowing air (~35 °C).

To investigate the effect of KCl, a saturated solution of KCl in water/ethanol was used to add KCl to the sample surface prior to exposure. The specimen was alternately sprayed with the solution and dried with flowing air (~35 °C) to avoid the formation of large droplets. The samples with 0.05 (AF) and 0.1-0.2 mg/cm^2 (APMT) KCl were then allowed to stabilize in a desiccator before their weight was recorded on a six-decimal Sartorius balance. The typical size of the KCl crystals was 10-100 μm (Fig. 6.4). KCl was also detected between some salt crystals (right image in Fig. 6.4). The effect of pre-oxidation prior to exposure with KCl was also studied. Alloy APMT was pre-treated at 700 °C, 900 °C and 1100 °C in order to establish alumina scales with different oxidation resistance (see Paper II and VI).
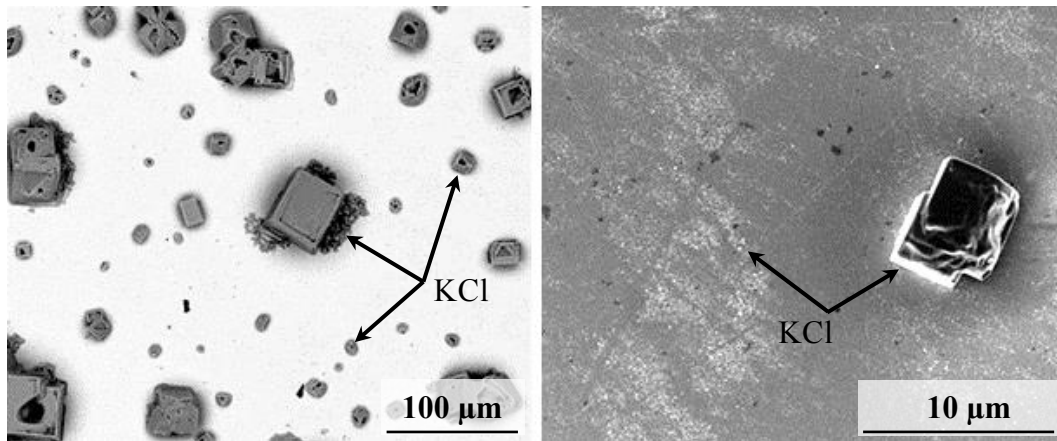
Figure 6.4 SEM-BSE image (left) and SEM-SE image (right) of unexposed polished alloy APMT with 0.1 mg/cm^2 KCl added to the surface.

6.3 Laboratory exposures

Two types of exposure systems were used in the present study; conventional horizontal tube furnaces (Fig. 6.5) and thermal gravimetric analysis (TGA see Fig. 6.6). The TGA was used to obtain the kinetics of the entire oxidation process. Horizontal tube furnaces were used to validate the TGA data and to obtain samples for the different analyses.

6.3.1 Ex-situ oxidation

Isothermal exposures were carried out in horizontal tube furnaces fitted with silica tubes (inner Ɵ 45mm). The samples were exposed to 5 % O_2 (~10 ppm H_2O), or 5 % O_2 + 40 % H_2O balanced with nitrogen at 600 ± 2 °C for 1, 3, 9, 24, 72 and 168 hours. The samples were inserted into a hot furnace at the beginning of the exposure to minimize the heating period in the experiments. The heating period was conducted in dry gas in order to avoid condensation on the samples when H_2O was present in the exposures. After the exposure the samples were air cooled in a desiccator. At least two exposures were performed at each measuring point with three samples in each experiment. The samples were mounted vertically on an alumina sample holder. The samples were placed parallel to the direction of the gas flow (1000 ml/min which corresponds to 3 cm/s) to avoid interaction between the samples. To obtain the desired gas mixture (with water vapour), the dry gas was bubbled in distilled water (79 °C) and cooled to the desired dew point (76.3 °C). The dry flow rate was calibrated using a Bios DC2 Flow Calibrator. All parts of the system were kept above 80 °C to prevent the condensation of H_2O.
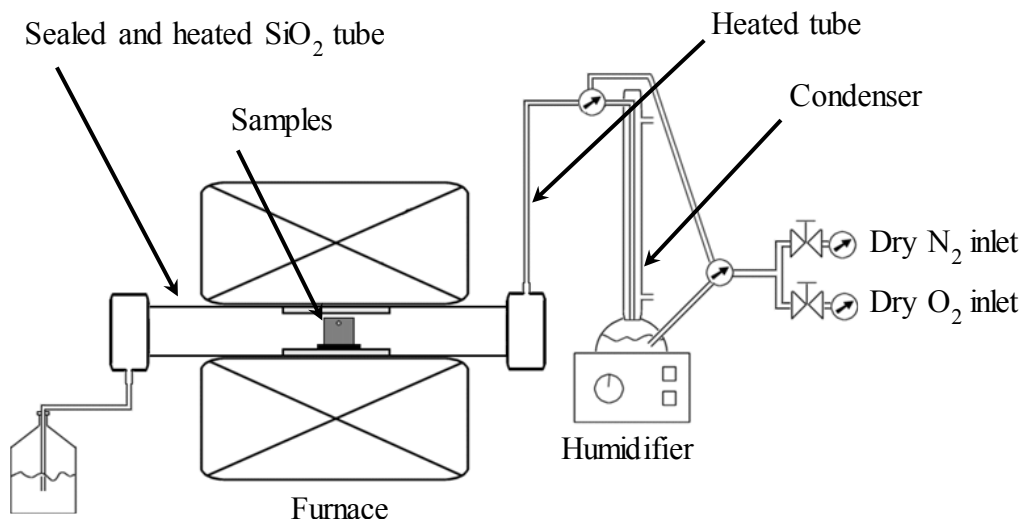
Figure 6.5. Schematic image of a horizontal tube furnace with a humidifier.

6.3.2 In-situ oxidation: Thermo Gravimetric Analysis (TGA)

A Setaram TAG thermo-balance was used to study the oxidation kinetics. The TGA was operated at 600-1100 °C and the exposure times varied up to 168 hours. The thermo-balance comes equipped with a double symmetrical furnace, where an Al_2O_3 sample with the same dimension as the FeCrAl sample was used as a reference in order to reduce the buoyancy effects (Fig. 6.6). The ex-situ weight changes were recorded to validate the system, using a six-decimal Sartorius balance. The gas flow was 15 ml/min in each furnace, which corresponds to 0.3 cm/s and consisted of 5 % O_2 or 5 % O_2 + 40 % H_2O balanced with N_2. A humidification system similar to the horizontal tube furnace experiments was used. The specimens were heated at 99 °C/min to the isothermal exposure temperature. The data was plotted from the time point at which the isothermal exposure temperature was reached.
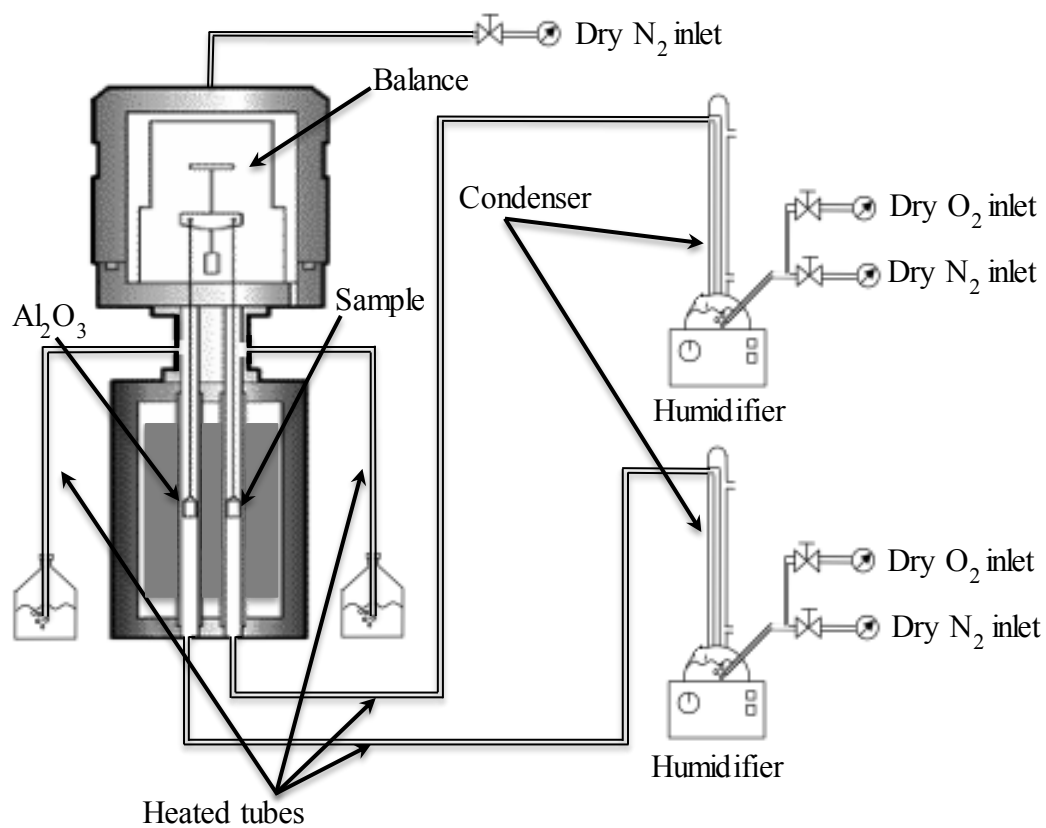
Figure 6.6 Schematic image of the TGA system equipped with humidifiers.

7 Analytical techniques

Various analytical techniques often give slightly different information. Some techniques are quick and harmless to the sample, e.g. SEM/EDX which gives elemental information and an idea about appearance. If one is interested in crystalline information, XRD might be a useful option. Problems could occur if crystalline phases are present in low amounts, then TEM would be the best technique. Different analytical techniques are complementary and a combination of techniques is often suitable in order to study the corrosion behaviour of alloys.

7.1 Scanning Electron Microscopy (SEM)

A Scanning Electron Microscope (SEM) is an instrument that scans a specimen with a finely focused electron beam. This method gives rise to a number of signals when it interacts with the specimen and these can be used to produce an image of the object of interest. Some signals, in addition to showing size and shape, can give information about topography, atomic number, elemental composition, and surface structure. The most commonly used signals are Secondary Electrons (SEs), Backscattered Electrons (BSEs) and X-rays. These signals may escape from a certain volume in the specimen (see Fig. 7.1).
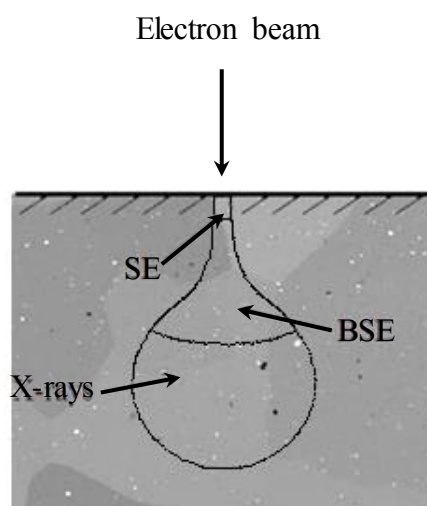
Figure 7.1 Illustration of the interaction volume in a specimen. The relative volume from which specific signals may escape is shown.

The size and shape of the interaction volume depends on the atomic number/numbers of the analysed specimen and the acceleration voltage. Figure 7.2 shows Monte Carlo

simulations of electron trajectories in four different solids at an accelerating voltage of 8 kV. The simulations were created using the program Casino v2.48. Depending on the composition of the analysed sample (and accelerating voltage) the collected information originates from a certain volume.
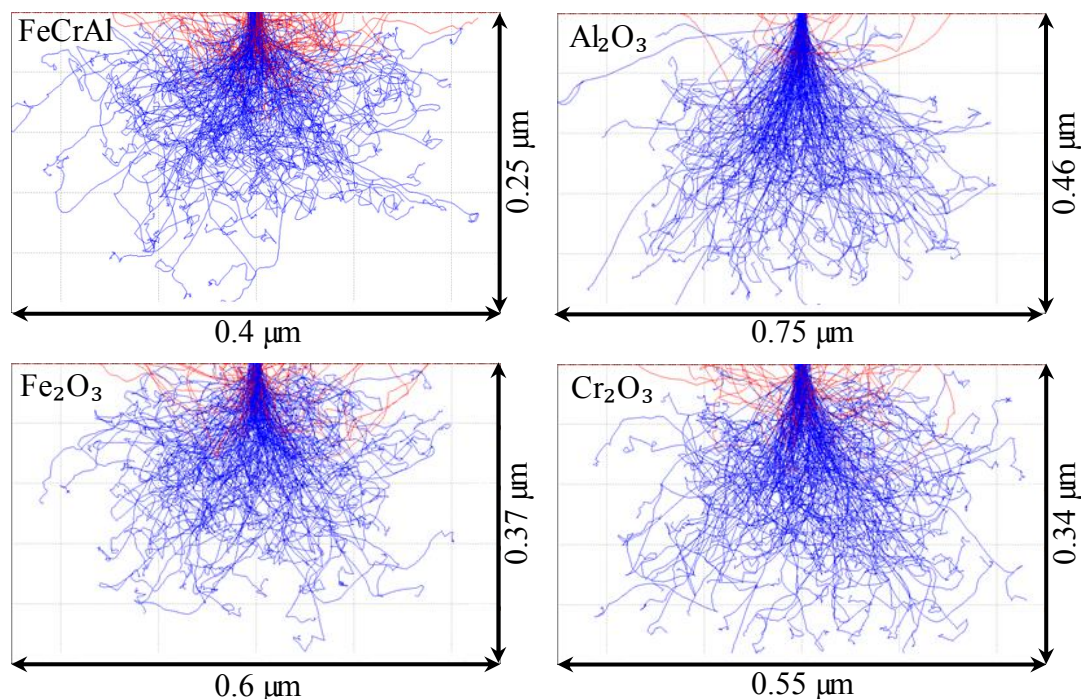
Figure 7.2 Monte Carlo simulations of the interaction volume in a Fe 20Cr 5Al alloy and three common oxides. The simulations were performed at an accelerating voltage of 8 kV.

An inelastic collision between an electron beam and a specimen can result in loosely bound outer shell electrons being removed from the specimen. These are called secondary electrons (SEs) and have low kinetic energy, less than 50eV. Depending on where these electrons are created, they either get captured by a nearby-ionized atom or may be emitted into the vacuum of the sample chamber. The secondary electrons that form at a depth less than 10 nm have the ability to reach the vacuum if an ionized atom does not capture it. This results in the signal from the SEs being representative of a small volume in the specimen, and which is often used for high-resolution surface images and to obtain topographical information. The topographical contrast originates from the fact that edges on the surface emit more SEs than a flat surface.

Backscattered electrons (BSEs) originate from the primary electron beam, which is deflected in a series of elastic scattering events. Depending on how many collisions an electron experiences before it returns to the vacuum, the energies for the emitted

BSEs will range from the primary beam energy (the accelerating voltage) down to the level of secondary electrons. The backscattered electron yield is proportional to the atomic number of the sample. This means that elements with a high atomic number appear brighter than elements with a lower atomic number. Consequently, imaging with BSEs offers compositional contrast.

X-rays are generated in a two-step process. In the first step one of the sample atom electrons is knocked out, causing an empty low energy position. The second step consists of a relaxation, when an outer electron falls into the lower energy state. This step causes an energy release through X-ray emission. The energies of the produced X-rays are specific to a certain kind of atom; consequently chemical identification is possible [53, 54].

Microscopy analysis in this study was performed in an FEI Quanta 200 FEG ESEM operated in high vacuum mode. The instrument comes equipped with an Oxford Inca Energy Dispersive X-ray (EDX) system, which was used for chemical quantification and elemental mapping. The ESEM was operated at 3-30 kV. A Leo ULTRA 55 FEG SEM was also used together with an in-lens SE detector for imaging at high magnification.

7.2 Transmission Electron Microscopy (TEM) and Scanning Transmission Electron Microscopy (STEM) with EDX

The Transmission Electron Microscopy (TEM) and Scanning Transmission Electron Microscopy analyses were performed by Ph. D Kinga A. Unocic (Papers III and VI), by Professor Mats Halvarsson and Ph. D Sead Canovic (Papers IV and V). A brief presentation of the technique is presented below.

TEM and STEM were used on selected samples in order to obtain detailed information on the corrosion products. In analogy to the SEM, an electron beam probes a sample but, in this case, transmitted electrons are detected instead of BSE and SE electrons. This requires the sample to be very thin, about 100 nm, and the accelerating voltage to be high, typically 200-300 kV. The electron transparent samples were prepared by using FIB/SEM work stations (see Section 7.3 below).

In order to image the sample Bright Field (BF), High Annular Dark Field (HAADF) imaging modes were used. In the bright field mode the weakening of the direct beam

by its interaction with the sample is imaged. In this manner, the sample thickness and diffraction contrast contribute to the image. Thick areas, areas enriched in heavy elements, and crystalline areas will appear with darker contrast in bright field imaging mode. In contrast voids will appear as white areas since the direct beam passes the sample without any interaction. The HAADF imaging mode has the benefit that it shows variations in the atomic number of atoms in the sample (Z-contrast). In other words, heavy elements appear bright in the HAADF image and lighter elements obtain a darker contrast.

Chemical analyses were performed by STEM/EDX. The STEM/EDX analysis works in a way similar to SEM/EDX, but with the difference that the thin TEM foil gives a lateral resolution of about 5 nm compared to 0.5 μm in the SEM (at 10 kV) [55]. Four different TEM instruments were used in this research and are described in Papers III-V and VI.

7.3 Focused Ion Beam / Scanning Electron Microscope (FIB/SEM)

In order to prepare electron transparent samples of selected features, two different FIB/SEMs were used. Platinum was deposited to the area of interest in the FEI Strata DB 235M first with electrons, and, subsequently, with ions in order to protect the oxide scale of interest during the sample preparation. In the Hitachi NB5000 workstation, however, carbon was deposited first, and, subsequently, tungsten in order to protect the area of interest. An electron transparent area (~15 μm wide, ~5 μm deep and about 100 nm thick) of the oxide scale and the subjacent metal was produced by milling with Ga ions in both workstations. The ion current was successively decreased from 20 nA to 100 pA during the milling in order to create a smooth electron transparent area. During the final step, the sample was tilted 1-3° in order to obtain a sample with parallel sides.

7.4 Transmission-Electron Backscattered Diffraction (t-EDSD)

The t-EBSD analyses were performed by Nooshin Mortazavi (Papers IV and V). A brief presentation of the technique is presented below.

Electron Backscattered Diffraction (EBSD) is a microstructural-crystallographic technique used to measure the crystallographic grain orientation in SEM. EBSD was used in this study to determine the crystalline phases present in the TEM samples

(Paper V). Instead of performing the rather time consuming diffraction of single grains in the TEM, EBSD can be used to map a larger area and obtain the crystalline phases present in the investigated area. In this manner, the EBSD technique gives information from many grains, which improves the statistics in the analysis.

The t-EBSD was carried out on the FIB-thinned samples (TEM sample) using an HKL Channel 5 EBSD system with a Nordlys II detector. In contrast to conventional EBSD, the foil was tilted 15° away from the phosphor screen and a shorter working distance (3.5 mm) was chosen. A Zeiss Ultra 55 FEG SEM was used in the high current mode with an acceleration voltage of 30 kV and an aperture size of 120 μm.

7.5 Broad Ion Beam (BIB) milling

A Gatan Ilion$^+$ Broad Ion Beam (BIB) system was used to prepare cross-sections by sputtering argon ions. The instrument is a good option when conventional grinding and polishing are difficult due to water sensitivity or because a sample is fragile. The final cross-section is comparable to a Focus Ion Beam (FIB) cross-section, but it is wider (roughly 500-1000 μm). A shield plate was used to obtain a smooth cross-section. The specimen was mounted so that it stuck out about 50 μm outside the shield plate (Fig. 7.3). The area outside the shield plate was then be sputtered away with argon ions and a cross-section was obtained. The ion gun was operated at 6 kV and the sputter time was 2-3 hours.

Since corrosion products are often porous and do not adhere well to an alloy, for this reason, some preparations were made before using the instrument. A 0.5 mm silicon plate was glued to the corroded sample with TEM glue (M-bond 610). The sample was then cut with a low speed saw without lubrication. An optical microscope was then used to find an area of interest and finally the sample was mounted to the shield plate with silver glue.
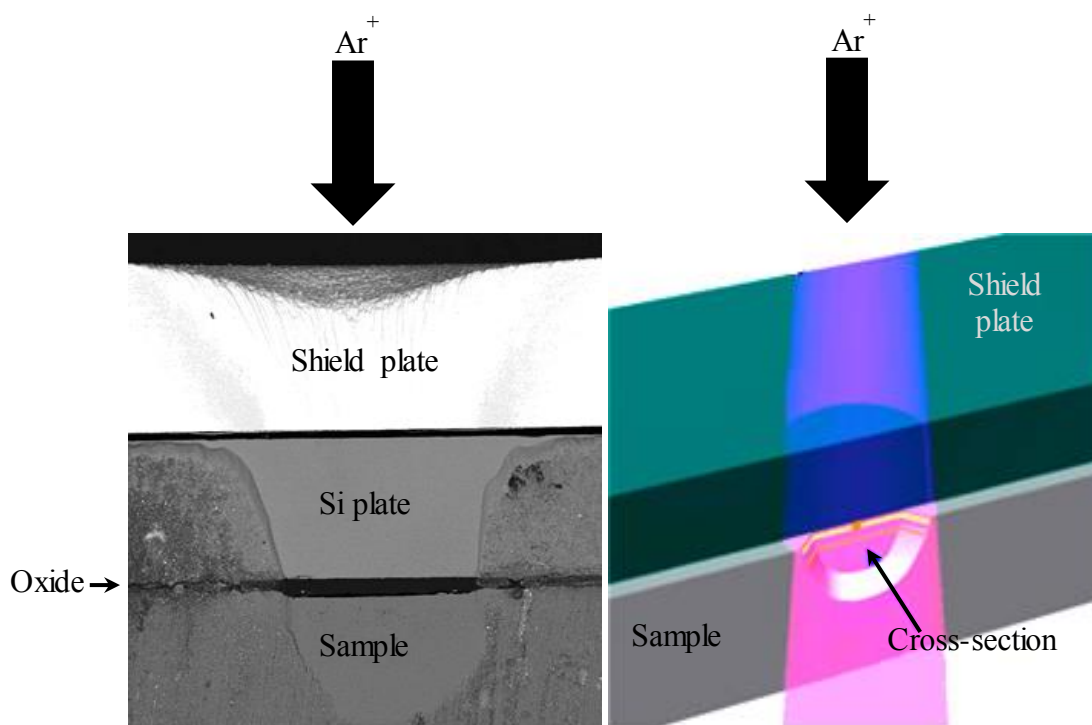
Figure 7.3 SEM-BSE image (left) and an illustration of a BIB cross-section (right).

7.6 Auger Electron Spectroscopy (AES)

Auger Electron Spectroscopy (AES) analyses were performed by Ph. D Josefin Hall (Papers I, II) and Ph. D Mats Norell (Paper III). A brief presentation of the technique is presented below.

Auger electrons can be used to obtain chemical information. The generation of auger electrons is similar to the formation of X-rays (described in Section 7.1), but instead of an X-ray, a loosely bounded electron is released. The kinetic energy of the released electrons contains chemical information from the atomic orbital it has left. Auger electrons can only escape from the topmost layers of atoms in a specimen, making the analysis very surface sensitive.

AES was used in Papers I and II to estimate oxide thickness and to determine elemental depth distribution. The AES analyses were performed with a PHI 660 Scanning Auger Microprobe (SAM) using an accelerating voltage of 10 kV and a beam current of 200 nA. AES depth profiling was performed using ion sputtering with 3.5 keV Ar^+. Two areas were analysed; one smaller 10 x 10 μm^2 and one larger 90 x 120μm^2. They exhibited almost the same oxide thickness and elemental depth distribution. Only the results from the small areas are shown in this study.

Quantitative analyses were performed using the peak-to-peak height of the auger transitions of a specific element together with sensitivity factors provided by PHI, except for the Al and O, which were calibrated against pure Al_2O_3. Since the sensitivity factor for oxygen in Cr_2O_3 and Fe_2O_3 is different from that for Al_2O_3, the oxygen signal will be slightly off when mixtures of the oxides are present [56]. The computer software PHI-Matlab and Linear Least Square (LLS) routines were used to separate the oxide and metal components in the depth profiles. This ensures that the detected Fe, Cr and Al in the oxide part of the depth profiles really are in oxidized form, and, consequently, do not originate from the metal substrate.

In addition, AES was conducted on the nano-scale one of the BIB cross-sections in Paper III. The instrument used was a ThermoFisher Microlab 350 with an accelerating voltage of 10 kV and a beam current of about 1 nA, which gave a nominal lateral resolution down to 12 nm. The area of interest was etched with 1 keV Ar^+ before the compositional analyse was performed, in order to remove contaminants (carbon).

7.7 Time of Flight-Secondary Ion Mass Spectrometry (Tof-SIMS)

Tof-SIMS analyses were performed by Ph. D Josefin Hall (Paper II). A brief presentation of the technique is presented below.

Secondary ion mass spectrometry is a useful technique for analysing small amounts of an element. It is also a good complement to AES to solve e.g. overlaps in the auger energies. The Tof-SIMS analyses were performed with a PHI TRIFT II instrument using a pulsed Liquid Metal Ion Gun (LMIG) enriched with $^{69}Ga^+$ ions. Depth profiles were obtained by sputtering a surface area of 50 x 50 μm^2 with a continuous non-pulsed beam with a primary ion energy of 15 kV and a current of 20 nA. Positive and negative static SIMS modes were used to analyse an area of 25 x 25 μm^2 at the centre of the sputtered area. All SIMS spectra were calibrated using the exact positions of peaks with a known mass/charge ratio, such as aluminium ($^{26}Al^+$), chromium ($^{52}Cr^+$), iron ($^{56}Fe^+$) and the Ga primary ion ($^{69}Ga^+$). In this method, intensities are expressed as peak areas rather than peak heights, because the energy distribution is not the same for all secondary ions. Before imaging the sample surfaces, an optimum sputtering time to remove surface contamination while at the same time preserving the remnants of previous surface deposit was 6 minutes using 2

nA, 25 kV ^{69}Ga$^+$ rastered over a 200 x 200 μm^2 area. The images were acquired during a sampling time of 8 minutes in both positive and negative modes.

7.8 X-Ray Diffraction (XRD)

X-rays are short-wavelength, high-energy electromagnetic radiation. When the formed X-rays are directed towards a sample surface they collide with the electrons of the sample atoms. When a periodic pattern, e.g. a crystalline material scatters radiation coherently, the total constructive interference at a specific angle is called diffraction. Bragg's law (20) from 1913 describes a simple way of understanding and predicting diffraction from a crystal.
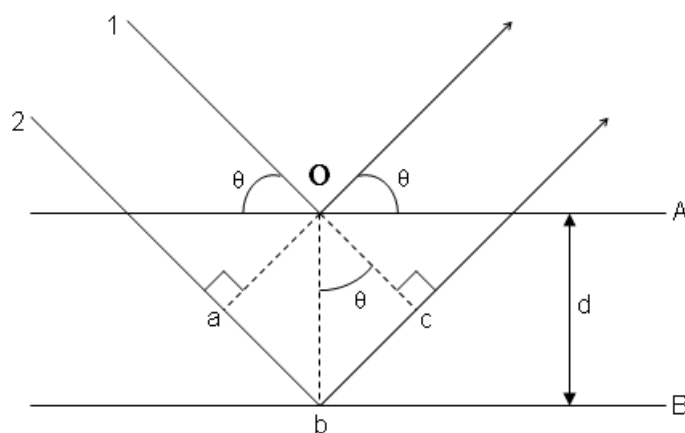
Figure 7.4 Schematic illustration of diffraction from a series of crystal planes according to Bragg's law.

A and B in Figure 7.4 illustrate two crystallographic planes with incoming X-ray beams. It is assumed that both incident waves are in phase and that they are scattered by both planes to derive the expression below. The second wave has to travel a distance abc longer than the first wave. In other words, all waves that are scattered from planes underneath A will be phase-shifted, causing interference. Constructive interference occurs when the distance abc equals n times the wavelength (λ) of the incident beam, thus the integer multiple of λ which results in Equation (20).

$$n\lambda = 2d\sin\theta \qquad (20)$$

Grazing incidence X-ray diffraction technique is common in corrosion science since it is surface sensitive. The X-ray beam is fixed and positioned almost parallel to the

sample surface to increase surface sensitivity. A detector is scanned through a range of angles and collects diffraction intensities [57].

To determine the crystalline corrosion products, a Siemens D5000 powder diffractometer was used. The instrument was equipped with a grazing-incidence-beam attachment together with a Göbel mirror. The sample was exposed to a source of CuK_α radiation (λ = 1.5418 Å) with an incident angle of 0.5-1.5°. The moving detector collected data in the range of 5° < 2θ < 70° with a step size of 0.05°. Silicon powder was added to the sample surface for calibration. The background was subtracted from the diffraction measurements. The diffractograms were compared with a database with known compounds to determine the present phases.

7.9 Ion Chromatography (IC)

Ion chromatography is a method for determining the concentrations of water-soluble ions in a solution. Ion chromatography separates ions based on the charge and size of the analysed ions. The solution of interest is separated in an analytical column. The separation emerges because different types of ions have unequal affinity to the basic functional groups within the column. To determine the concentration of the different ions, conductivity measurements are made after the column and compared with solutions of known concentrations of the ions of interest.

The exposed samples were leached in 5 ml Milli-Q water using ultrasonic agitation for 10 + 10 min. A Dionex ICS-90 system was used to establish the amount of water-soluble anions (CrO_4^{2-}, Cl^-). The anions were analysed with an IonPac AS4A-SC analytic column, and 1.8 mM Na_2CO_3/1.7mM $NaHCO_3$ was used as elution.

To determine the remaining amount of water-soluble cations (K^+), the samples were analysed with a Dionex ICS-900 system with an IonPac CS12A analytic column. The elution was 20 mM sulfonic acid and the flow rate was 2 ml/min for both anions and cations. The detection limits for the different species were: Cl^- = 0.03 µmol, K^+ = 0.03 µmol and CrO_4^{2-} = 0.01 µmol.

8 Results and Discussion

To determine the effect of KCl, the oxidation in O_2 and $O_2 + H_2O$ was first evaluated to the relevant temperature (600 °C). As mentioned earlier, the formation of α-Al_2O_3 is not favoured at lower temperatures, and it could be difficult to obtain a protective alumina scale at 600 °C. This obstacle could be circumvented by the usage of pre-formed alumina scales prior to the exposure with KCl. For this reason, oxidation tests were conducted at 700, 900 and 1100 °C in order to understand the protective properties of the formed alumina scales.

8.1 Oxidation in O_2 and $O_2 + H_2O$, (Papers I, II, IV and V)

8.1.1 Oxidation at 600 °C, (Papers I, II)

Oxidation at 600 °C resulted in nominal mass gains after 168 hours of exposure at 600 °C in O_2 and $O_2 + H_2O$. Initially, the oxidation rate was rapid for Kanthal®APMT in both environments and then slowed down with time due to the formation of a protective oxide in both environments (Fig. 8.1). The mass gain was slightly accelerated in the presence of water vapour on both alloys.
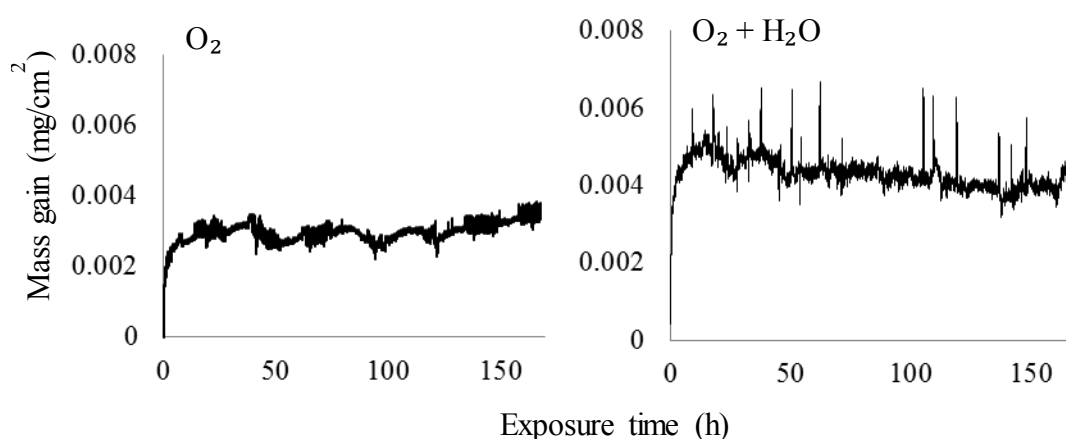
Figure 8.1 TGA curves (In-situ mass gain vs. exposure time) for alloy APMT exposed to O_2 and $O_2 + H_2O$ at 600 °C for 168 hours.

The surface of alloy APMT after exposure was smooth and featureless in both environments after the exposure at 600 °C (see Paper II). AES analyses of both alloys showed that the oxide film was dominated by aluminium with significant amounts of

iron and chromium present in both environments (Fig. 8.2 and Papers I and II). Chromium was enriched in a band in the middle of the oxide film and iron oxide was consistently found outside the chromium enrichment. The AES depth profiles showed that the formed oxide scales were somewhat thicker on alloy AF in both environments than on alloy APMT. The AES depth profiles also showed that the formed oxide scale became slightly thicker on both alloys when water vapour was present (see Fig 8.2 for alloy APMT).
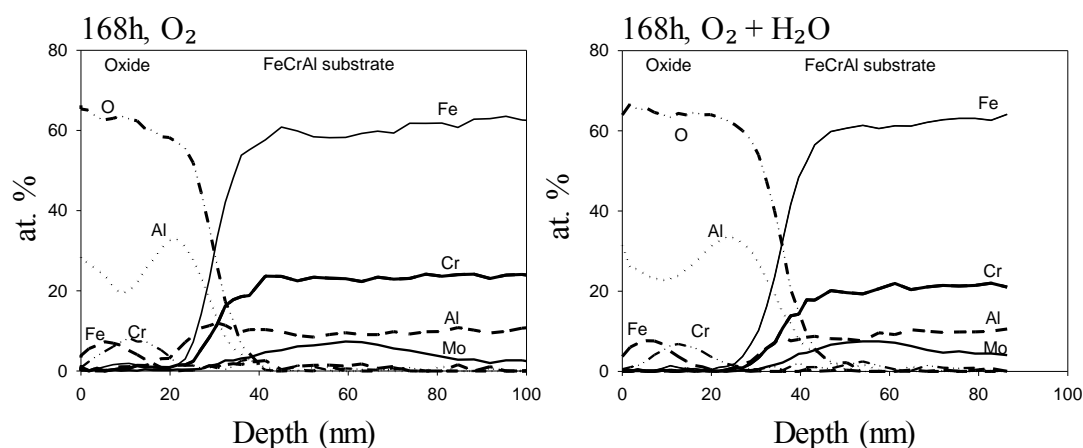
Figure 8.2 AES depth profiles of alloy APMT exposed to O_2 and $O_2 + H_2O$ at 600 °C for 168 hours.

Although the oxide film was dominated by aluminium oxide, no crystalline aluminas could be detected with XRD. Instead, a corundum-type chromium-rich $(CrFe)_2O_3$ was detected at all exposure times on both alloys. It is suggested that the iron and chromium in the Al-rich oxide film had entered the scale during transient oxidation, i.e., during and immediately after the heat-up of the sample.

Similar observations have been observed on FeCrAl alloys at 500-800 °C in O_2 and $O_2 + H_2O$ [30, 58, 59]. In those studies α-Al_2O_3 was detected at 700 °C with XRD while no crystalline forms of aluminas were detected at lower temperatures.

8.1.2 Oxidation at 700 °C, (Paper II)

A mild form of pre-oxidation was conducted on alloy APMT in O_2 for 24 hours at 700 °C. As expected, a thin and smooth aluminium-rich oxide scale formed which was similar to the one formed at 600 °C, except that it was thicker and more Al-rich (Paper II). XRD showed evidence of Cr_2O_3 while no crystalline alumina phases could be identified.

8.1.3 Oxidation at 900 °C, (Paper IV)

The mass gains from the tube furnace exposures were quite low after the exposures in the O_2 and $O_2 + H_2O$ environments for up to 72 hours at 900 °C (Fig. 8.3). Mass gain was relatively high during the first hours of the exposure and then slowed down appreciably with time. Mass gain was accelerated in the presence of H_2O, the effect being most marked up to 24 hours.
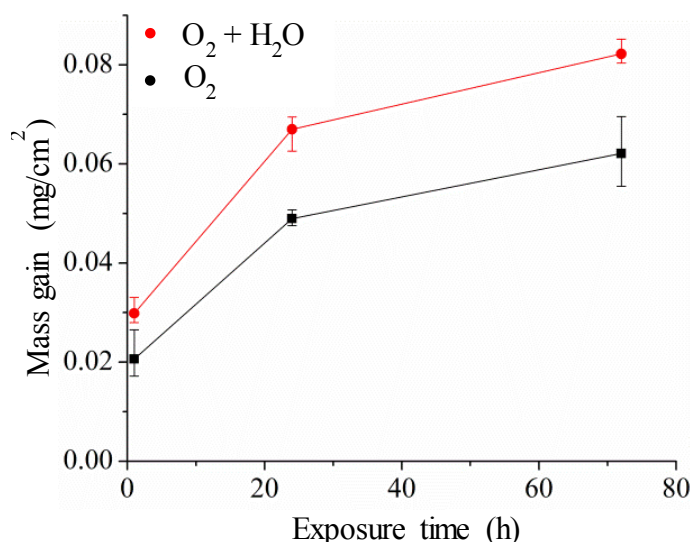
Figure 8.3 Mass gain of alloy APMT exposed to O_2 and $O_2 + H_2O$ at 900 °C for 1, 24 and 72 hours.

The in-situ mass gains shown in Figure 8.4 are somewhat contradictory to the ex-situ exposure (Fig 8.3), since the TG exposures did not show any enhanced oxidation in the $O_2 + H_2O$ environment. It should be noted that three similar exposures were conducted in O_2 and $O_2 + H_2O$ in the TG. The fairly low mass gains overlapped in some of the exposures between O_2 and $O_2 + H_2O$, but the trend was, nevertheless, that the mass gain did not not accelerate in the presence of water vapour. When comparing the in-situ and ex-situ mass gain curves it may also be noted that the in-situ mass gain measurements started after reaching 900 °C. This means that the mass gain during the 9-minute heat-up period was not recorded. This implies that the mass gains recorded in-situ can be expected to be slightly lower than the ex-situ mass gains.
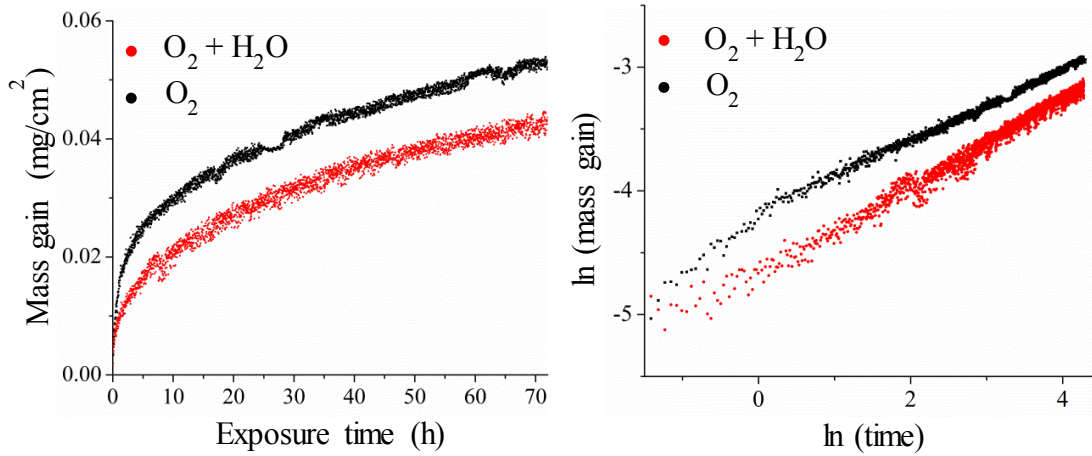
Figure 8.4 In situ TGA measurement showing mass gain vs. exposure time (left graph) for alloy APMT exposed to O_2 and $O_2 + H_2O$ at 900 °C for 72 hours. The data was logarithmised (right graph) in order to evaluate the kinetics.

The kinetics of the mass gain curve in Figure 8.4 can be further elucidated by displaying the data on an $\ln(m)$ vs. $\ln(t)$ plot. Assuming that the mass gain is proportional to the exposure time, the slope will correspond to $1/\alpha$ where α is the exponent in the kinetic Equation (21), a constant mass gain corresponding to $\alpha = 1$ and parabolic oxidation gives $\alpha = 2$.

$$m^\alpha \propto t$$

$$\alpha \ln(m) \propto \ln(t)$$

$$\ln(m) \propto 1/\alpha \ln(t) \tag{21}$$

The $\ln(m)$ vs. $\ln(t)$ graph in Figure 8.4 shows that the oxidation kinetics follows a straight line in $O_2 + H_2O$ during the entire exposure, which was close to cubic oxidation kinetics. The oxidation kinetics in dry O_2 slowed down with time from parabolic (first hour) to close to cubic. This suggests that the initial oxidation (heating period) was faster in $O_2 + H_2O$ than in the O_2 environment since a slower oxidation kinetics was obtained earlier in the presence of H_2O. This could be the reason why the mass gain was lower in $O_2 + H_2O$ than in the O_2 environment in Figure 8.4.

TEM samples were prepared after 1 hour of oxidation in O_2 and $O_2 + H_2O$ environments in order to investigate the initial oxidation more in detail. The microstructure of the oxide scales was quite similar in both environments after 1 hour of exposure at 900 °C (Fig 8.5). A thin and well-adherent alumina scale was formed after only one hour of exposure in both environments (Fig. 8.5). In accordance with

40

the ex-situ gravimetric data, the alumina scale formed in the $O_2 + H_2O$ environment was somewhat thicker than in the O_2 environment.
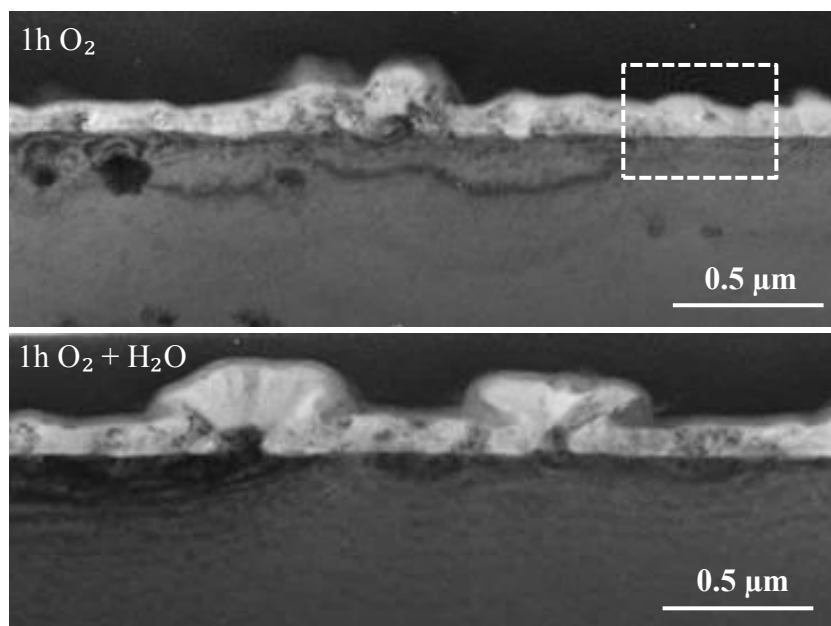
STEM-BF image of the cross-sections of the oxide scale formed on alloy APMT, exposed to O_2 and $O_2 + H_2O$ at 900 °C for 1 hour.

In both environments, oxidation produced an oxide scale that contained two alumina layers after one hour of exposure. While the bottom alumina layer was rather even with a thickness of about 20 nm in both environments, the top alumina layer varied substantially in thickness over the surface (8.5). The boxed area in Figure 8.5 represents a location with a thin oxide scale and is illustrated in Figure 8.6 in higher magnification. The two-layered alumina scale is clearly shown with the much thicker top part in the figure. The alumina layers were separated by Cr-rich rounded particles immersed in the alumina scale (Fig. 8.6). The areas in the top alumina layer, which show bright contrast in Figure 8.6, had been enriched in iron. Both the Cr-rich particles and iron are suggested to be remnants from the initial oxidation. The fact that Cr-rich particles formed rather than being dispersed in the alumina, is suggested to reflect the very limited solubility of chromia in α-alumina at 900 °C [60]. Liu *et al.* [61] have suggested that the presence of iron in the outer part of the top alumina can be attributed to that iron (Fe^{2+}) has a higher mobility in the alumina scale than chromium (Cr^{3+}).

The remaining part of the top alumina layer consisted of oxide nodules with up to four times the thickness of the thin top layer (Fig. 8.7). The oxide nodules were more

41

pronounced in O_2 + H_2O than in the O_2 environment. This could explain the higher recorded mass gains (ex-situ, Fig. 8.3) in the presence of water vapour.
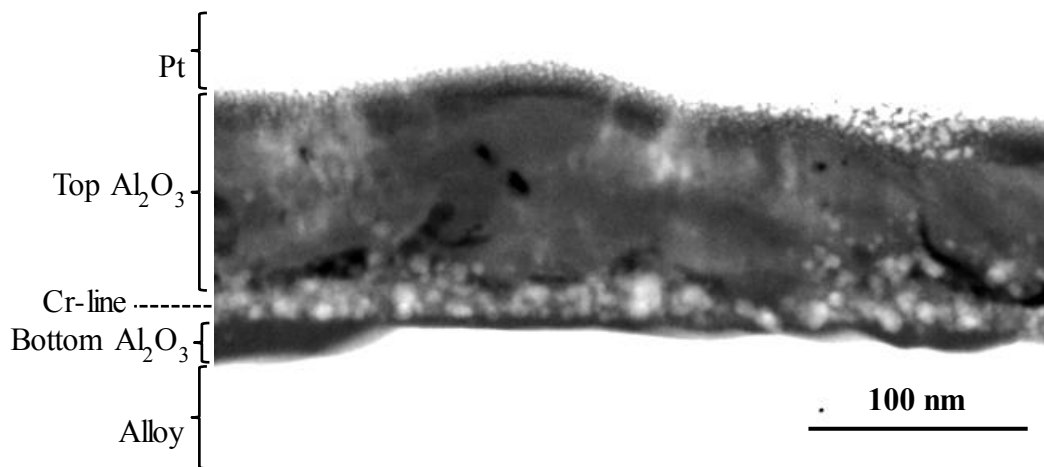
Figure 8.6 STEM-HAADF image of the cross-section of the oxide scale formed on alloy APMT, exposed to O_2 at 900 °C for 1 hour.

One of the oxide nodules formed in the O_2 environment at 900 °C after one hour is shown in Figure 8.7. The strong image contrast suggests that there is a metal protrusion sticking up from the alloy into the oxide nodule and clearly reaches above the chromium-rich particles which was suggested (see above) to be the initial alloy surface. STEM/EDX analyses suggest that the protrusion is metallic and made up of a composition that matches the alloy.
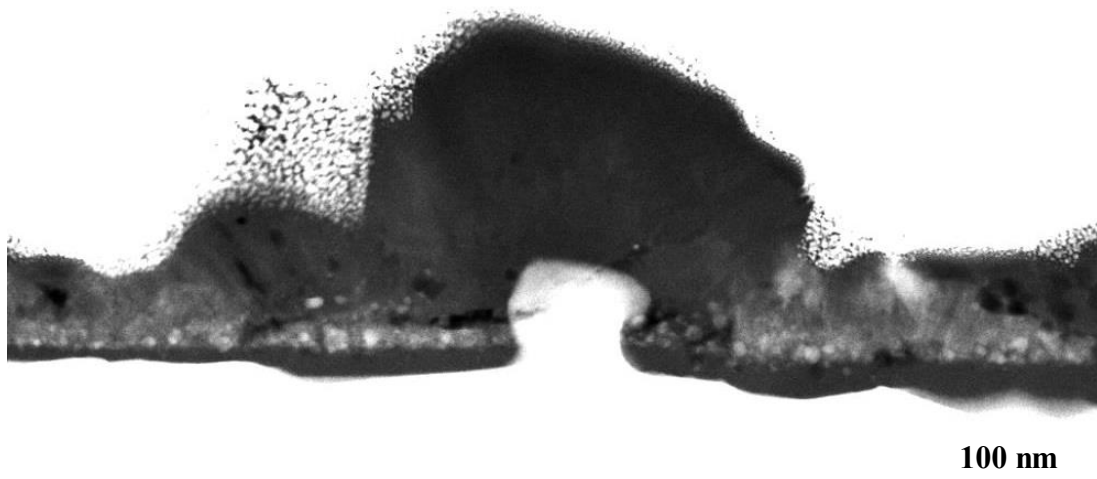
Figure 8.7 STEM-HAADF image of the cross-section of the oxide scale formed on alloy APMT, exposed to O_2 at 900 °C for 1 hour.

It is suggested in Paper IV that the metallic protrusions were formed by a reduction of Fe and Cr oxide caused Al in the metallic substrate. Several types of iron oxides could be reduced in this way; the reduction of FeO is shown in Reaction (22).

$$2 \text{ Al(alloy)} + 3 \text{ FeO(s)} \rightarrow \text{Al}_2\text{O}_3(s) + 3 \text{ Fe(s)} \tag{22}$$
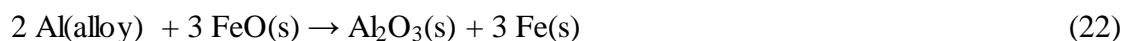
It may be noted that a prerequisite for Reaction (22) to occur is direct contact between FeO in the oxide layer and the alloy substrate, i.e. the reaction will cease once the inward-growing alumina layer has become fully established. To support this hypothesis, the formed oxide nodule in Figure 8.7 has a darker contrast, indicating a lower amount of iron in the alumina.

α–Al_2O_3 was detected with XRD after all exposure times in both O_2 and $\text{O}_2 + \text{H}_2\text{O}$ environments at 900 °C. In addition, the phase composition of the top and bottom layers was determined with Convergent Beam Electron Diffraction (CBED). All diffraction patterns were indexed as α–Al_2O_3 (see Paper IV). No metastable alumina phases were identified with XRD and CBED after one hour of exposure, neither in O_2 nor in $\text{O}_2 + \text{H}_2\text{O}$. Thus, if any metastable aluminas were formed during the initial oxidation they were transformed into α–Al_2O_3 within the first hour of exposure.

Paper IV showed that the top alumina layer does not grow significantly after exposure times exceeding 1 hour in both environments. Thus, scale growth occurs with time in the bottom alumina layer, resulting in the formation of columnar grains. The microstructure of the formed alumina scales was not strongly dependent on the presence of water vapour, the cross-sections in Figure 8.8 showing almost the same scale thickness after 24 hour exposure.
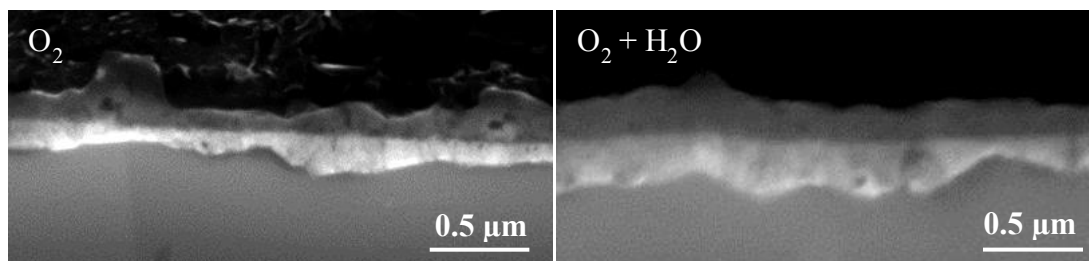
Figure 8.8 SEM-SE image of the cross-section of the oxide scales formed on alloy APMT, exposed to O_2 and $\text{O}_2 + \text{H}_2\text{O}$ at 900 °C for 24 hour.

8.1.4 Oxidation at 1100 °C, (Paper V)

Alloy APMT and AF were exposed at 1100 °C in O_2 and $O_2 + H_2O$ environments for 1, 24 and 168 hours. The mass gains were slightly higher for alloy AF than for alloy APMT in both environments (see Paper V). The XRD analyses showed that $\alpha–Al_2O_3$, was the dominant crystalline product on both alloys after all exposure times.

Figure 8.9 shows in-situ TGA data of alloy APMT in dry O_2 and $O_2 + H_2O$ environments. Similar to the ex-situ mass gains (Paper V), the oxidation was somewhat higher in the presence of water vapour. Figure 8.9 also shows an ln(mass gain) vs. ln(time) graph. The oxidation kinetics was close to parabolic in the $O_2 + H_2O$ environment throughout the entire exposure (Fig. 8.9). The oxidation kinetics slowed down with time from parabolic to sub parabolic. In the dry O_2 environment the slope was initially steeper corresponding to a lower value of α (0.6) and became parabolic after about 7 hours. The low value of α actually implies that the oxidation accelerated during the initial oxidation period.
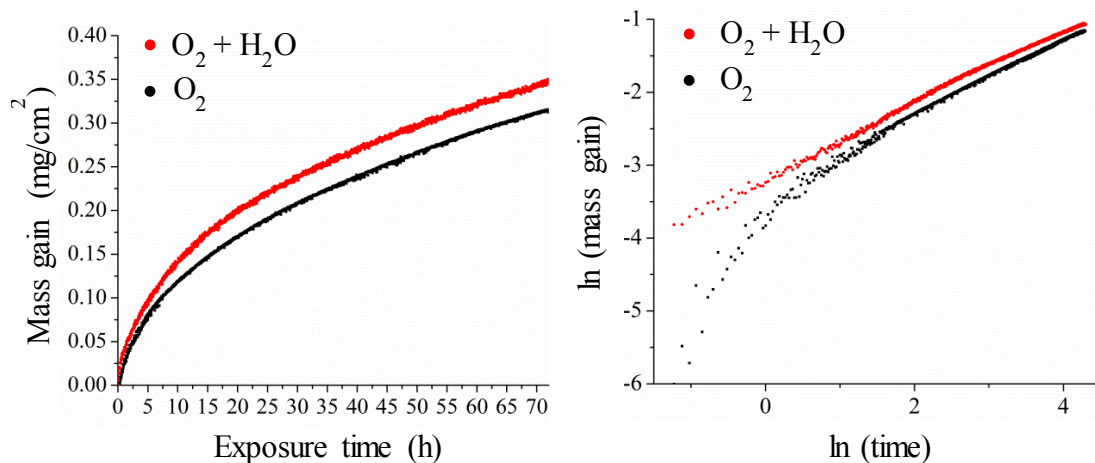
Figure 8.9 In situ TGA measurement showing mass gain vs. exposure time (left graph) for alloy APMT exposed to O_2 and $O_2 + H_2O$ at 1100 °C for 72 hours. The data was logarithmised (right graph) in order to evaluate the kinetics.

Sub parabolic oxidation kinetics is expected if the rate of scale growth on a metal is limited by grain boundary diffusion across an oxide that exhibits grain growth [17]. The shift from parabolic to sub parabolic oxidation kinetics was attributed to oxide grain growth at the bottom of the scale during the exposure (see Figure 8.10 below).

Figure 8.9 shows that water vapour only had an initial effect on the rate of isothermal oxidation of alloy APMT at 1100 °C. Thus, while the mass gain after 168 hours was somewhat accelerated in the presence of water vapour, oxidation kinetics were nearly

parabolic in both environments and the corresponding parabolic rate constants were essentially the same.

The initial accelerating effect of water vapour on oxidation is evident in Figure 8.9. The oxidation became diffusion controlled faster in the presence of water vapour than in the dry exposure. In the absence of H_2O, the transport of species across the oxide scale only became rate limiting at a relatively late stage (about 7 hours), implying that the rate of oxidation was initially limited by a surface reaction. It is suggested that the initial rate-limiting reaction in the O_2 environment is the reduction of O_2 on the scale surface.

The initially faster oxidation in $O_2 + H_2O$ than in O_2 implies that the reduction of water on the surface along with O_2 reduction, contributed to metal oxidation. This means that the formation of a protective oxide scale is faster in the presence of water vapour. In accordance with this idea, Åkermark and Hultquist [62], working with early stages of oxidation of a FeCrAl alloy in O_2 and H_2O environments, have reported that exposure in an $O_2 + H_2O$ environment at 920 °C resulted in the simultaneous reduction of O_2 and H_2O, the reduction of water by the alloy being evidenced by H_2 evolution.

SEM/EDX analyses were performed on the cross-sections of both alloys after all exposure times. Kanthal® APMT and AF formed a two-layered alumina scale in both the dry and the humid environments. The two alumina layers were separated by a relatively straight interface, presumably the original sample surface. It was assumed that the top alumina layer had grown by the outward diffusion of cations, that the bottom layer had grown by the inward diffusion of oxygen ions and, consequently, that the interface between the two layers corresponded to the original metal surface.

Scale thickness measurements using SEM showed that the top alumina layer was thinner on alloy APMT than on alloy AF. The alumina scale grew predominantly inward with time on both alloys in the dry and humid environments. The top layer did not grow much in thickness on alloy APMT after the initial oxidation while the top layer increased in thickness on alloy AF (see Paper V).

The limited outward growth of alloy APMT compared to alloy AF is suggested to be attributed to the difference in RE element addition. In other words, while alloy APMT

contained RE's in the form of oxide dispersion, the RE's were added to alloy AF in elemental form. It has been reported by several authors that the outward growth of alumina scales is reduced more effectively by adding RE's in the form of an oxide dispersion than in the elemental form [20]. The two alloys also differ with respect to the RE's present. Thus, alloy APMT contains Zr, Y and Hf while alloy AF contains Zr and Y.

STEM was used to investigate the microstructure more in detail on alloy APMT exposed to O_2 and $O_2 + H_2O$ for 168 hours at 1100 °C. Figure 8.10 shows the two-layered alumina scales formed in the dry and humid environments, the interface between the top and bottom layer are indicated by the dotted lines. The alumina scale was slightly thicker in the presence of water vapour.
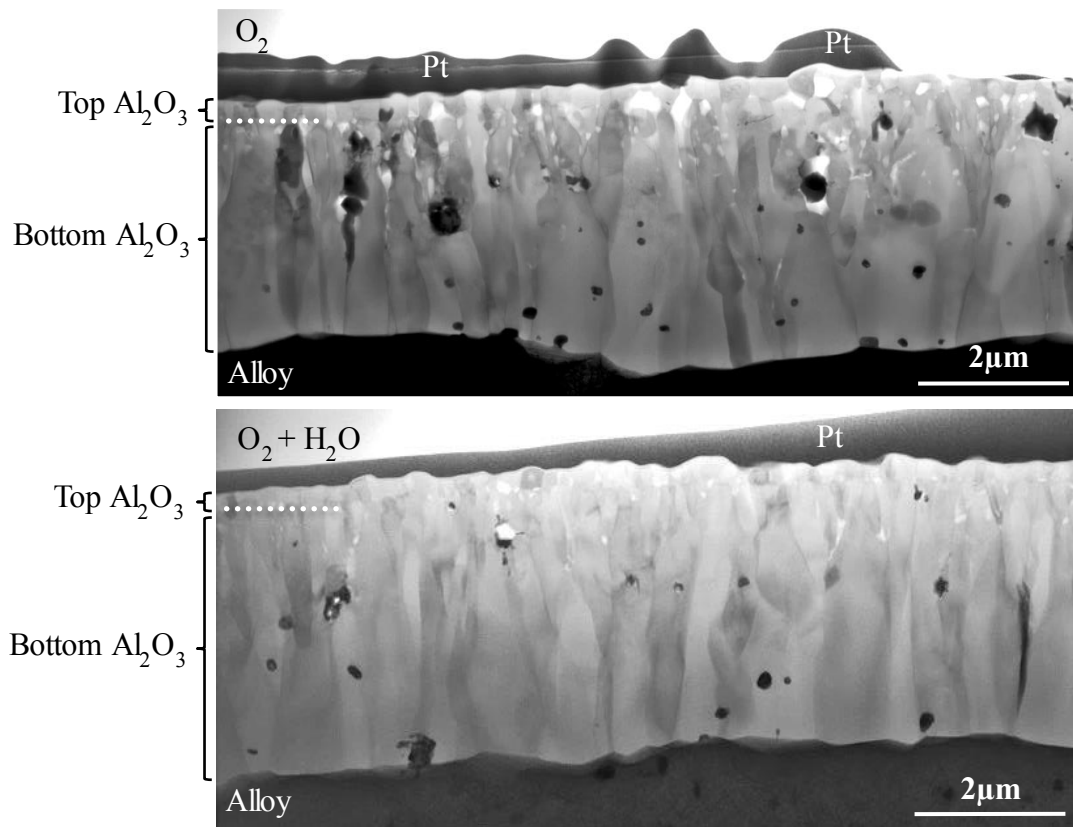
Figure 8.10 STEM-BF images of the cross-section of the oxide scales formed on alloy APMT, exposed to O_2 and $O_2 + H_2O$ at 1100 °C for 168 hour.

The alumina grains in the top layer were equi-axed in both environments with the same size as the layer thickness, and it was found that the outer layer was one grain thick. The bottom alumina layer consisted of columnar grains which were wider at the bottom of the scale than at the top. This means that the diameter of the columnar

alumina grains increased as they grew inward in both environments. This evidence of grain growth in the bottom layer supports the sub parabolic oxidation kinetics observed in Figure 8.9 after longer exposure times.

The bottom part of the scale contained RE particles (dark contrast) in the range from <0.1 to 0.5 μm in diameter. The distribution, size, and position of the RE particles in the oxide layer were similar in both environments. The porosity (white areas in Figure 8.10) was lower in $O_2 + H_2O$ than in the dry environment. The pores were distributed in the same way, and were located mainly in the outer part of the bottom layer; at the interface between the bottom and top layers, and in connection to the larger RE particles.

8.2 The influence of O_2 + KCl at 600 °C, (Paper I)

Potassium chloride strongly influenced oxidation behaviour in dry O_2 (Fig. 8.11). After 72 hours the mass gain had accelerated about 100 times compared to the samples exposed in the absence of KCl (compare Figs. 8.1 and 8.11).
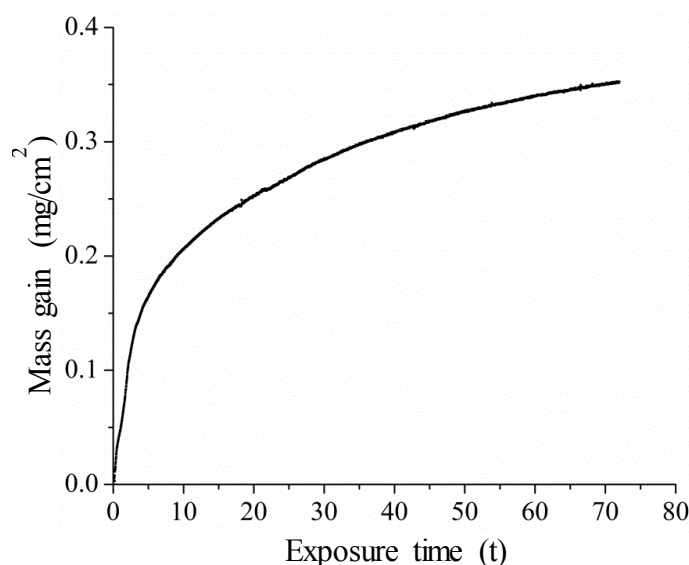
Figure 8.11 In-situ TGA (mass gain vs. exposure time) for alloy AF exposed at to O_2 at 600 °C with added KCl for 72 hours.

Mass gain was large compared to the added amount of salt and it was relatively rapid during the first 24 hours and then continued at a slower pace, indicating that a somewhat protective oxide was formed with time (see Paper I). The corrosion became increasingly complex when KCl was added to the exposure. The in-situ mass gain in

Figure 8.11 is suggested to include alloy oxidation, potassium chromate formation by Reaction (19), alloy chlorination as well as the volatilization of KCl and metal chlorides. Obviously, several of these processes can occur simultaneously throughout the experiment. Initially a chromium-rich corundum-type oxide $(FeCr)_2O_3$ was formed on the surface which became more iron-rich with time, and after 72 hours pure Fe_2O_3 could be detected with XRD (Paper I). K_2CrO_4 formed after 1 one hour and was detected after longer exposure times as well. The majority of the KCl was consumed or vaporised rapidly in the dry O_2 environment at 600 °C. The IC analysis agrees well with the XRD results showing that the amount of chlorine decreased with exposure time (Paper I). Chromate (VI) was detected after all exposure times and the amount decreased with longer exposure times.

The corrosion was complex in O_2 + KCl with several parallel reactions occurring on the surface (Paper I). Early in the oxidation process (after 1 hour) a thin and smooth oxide covered most of the surface (see left image in Fig. 8.12).
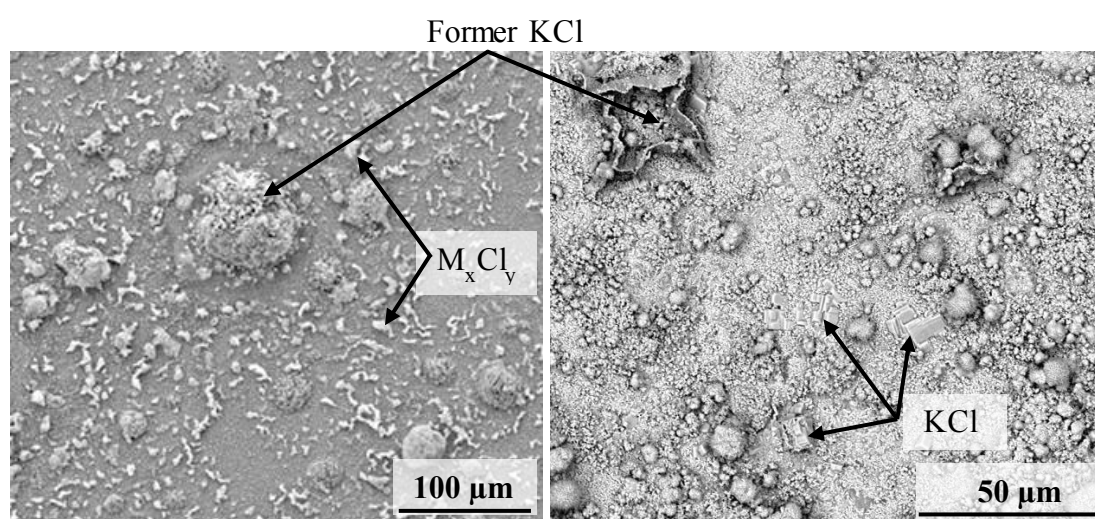
Figure 8.12 SEM-SE image (left) and SEM-BSE (right) of alloy AF exposed at 600 °C for 1 hour (left) and 3 hours (right) in O_2 with KCl.

The thin oxide had, however, failed at places where former salt particles had been replaced with iron-rich corrosion product agglomerates. In addition numerous metal chloride particles of the alloying elements were present on the surface after 1 hour of exposure in dry O_2 + KCl (Fig. 8.12). After only 3 hours, the majority of the surface was covered with a rough iron-rich oxide (see right image in Fig. 8.12) with a few K_2CrO_4 particles and KCl crystals on top of the surface. The same oxide

48

morphologies were present after 24 and 72 hours, as described after 3 hours except that KCl was no longer detected.

A cross-section after a 24-hour exposure showed that a porous and multi-layered oxide scale was present with an Oxidation Affected Zone (OAZ) in the alloy substrate, which contained particles enriched in aluminium and nitrogen (Fig. 8.13). The four sub scales consisted of oxides made up of Al, Fe and Cr. It is proposed that each of these thin layers corresponds to an external scale that was once protective. Obviously, only the innermost layer is still protective at this stage. The outermost layer at the oxide/gas interface contained more aluminium in the bottom part. It is suggested that this layer was once the initial alloy surface. Metal chloride was detected at the alloy/oxide interface in connection to alloy grain boundaries (see Fig. 8.13).
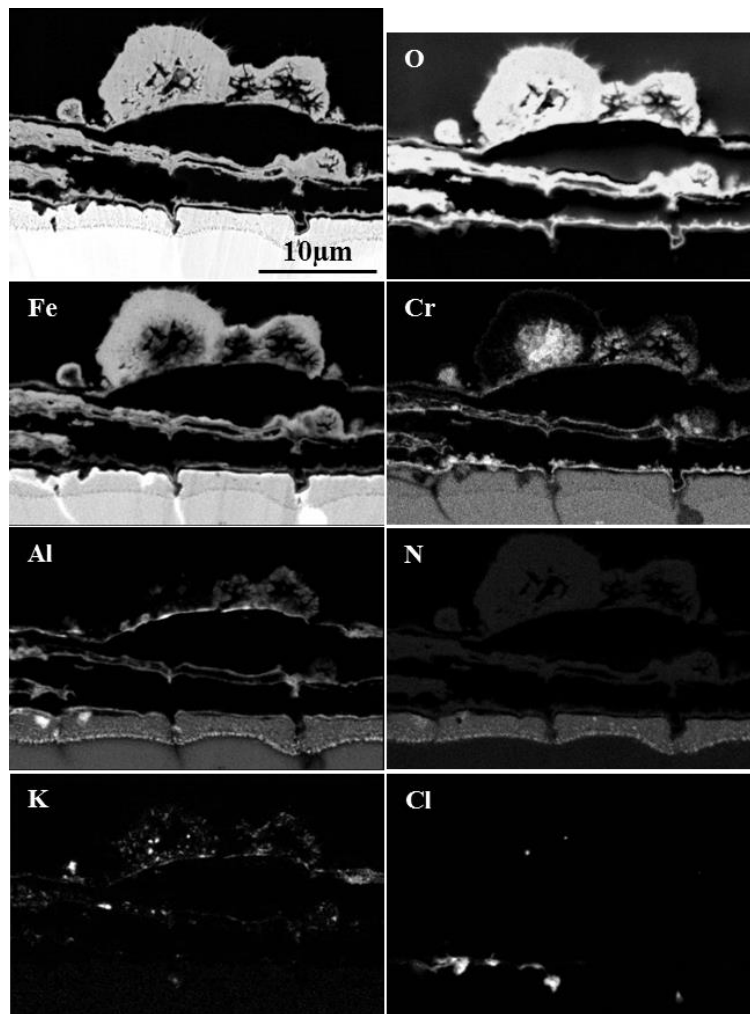
Figure 8.13 SEM-BSE image and EDX elemental maps of the cross-section of alloy AF exposed at 600 °C for 24 hours in O_2 with KCl.

The high degree of alloy chlorination in O_2 + KCl is suggested to be connected to the low amount of water vapour in the exposure environment (Paper I). It has been reported by Pettersson *et al.* that chromate formation by Reaction (19) is favoured by the presence of water vapour on the commercial stainless steel 304L in the presence of KCl at 600 °C [63]. The low water vapour content in the dry O_2 environment (~10 ppm) results in less consumption of KCl through Reaction (19). Consequently KCl will be available on the surface, resulting in a high degree of alloy chlorination. The formation of metal chlorides at the metal/oxide interface is suggested to create the porous multi-layered oxide scale observed in Figure 8.13. It was shown in Paper I that the commonly used sources for chlorine formation in the presence of KCl do not form the necessary amounts of Cl_2 needed for alloy chlorination in the present environment. It is concluded that a new model is needed to explain the observed alloy chlorination. It is proposed that the problems in the chlorine cycle mechanism (see section 5.2) can be resolved by applying an electrochemical mechanism for alloy chlorination similar to the one described in Section 3.1.

The association of K and Cr was attributed to K_2CrO_4, which was mainly considered to be formed through Reaction (19). However, it is suggested that K_2CrO_4, may also form as part of the following electrochemical reaction:

Scale surface: $2KCl(s) + 5/4\ O_2(g) + 1/2Cr_2O_3(s) + 2e^- \rightarrow K_2CrO_4(s) + 2Cl^-$

Scale/alloy interface: $Fe(s) \rightarrow Fe^{2+} + 2e^-$

Σ: $2KCl(s) + 5/4\ O_2(g) + 1/2Cr_2O_3(s) + Fe(s) \rightarrow K_2CrO_4(s) + FeCl_2(s)$ (23)
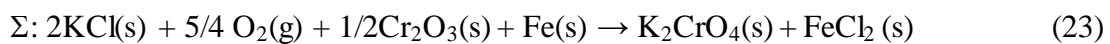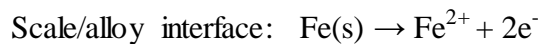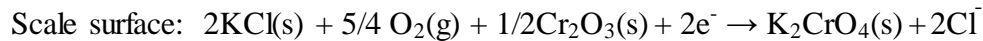
The thermodynamic calculations show that the reaction is favoured in the present environment (Paper I). The corresponding reactions with Cr and Al provide even higher thermodynamic driving forces. The above electrochemical mechanism requires a conducting scale for both ions and electrons. Cationic conduction through oxide scales is known to be dominated by grain boundary transport at 600 °C [18]. Thus, the ionic transport in the electrochemical cell is suggested to occur in the oxide grain boundaries. In such a scenario, the relative transport rates of chloride ion and metal ions would determine whether the metal chloride forms on top of the scale or at the scale/alloy interface. The poor adherence of the oxide layers in Figure 8.13 is suggested to be connected to the presence of transition metal chloride at this interface.

8.3 The influence of O_2 + H_2O + KCl at 600 °C, (Papers I, II and III)

KCl accelerates the corrosion of both alloy AF and APMT in the presence of O_2 + H_2O + KCl in line with the dry exposures. However, the appearance of the mass gain curves differs from those for the dry exposure (compare Figs. 8.11 and 8.14). In other words, in O_2 + H_2O, the TG curve was linear after the initial oxidation. Subsequently, the mass gain accelerated rapidly, which indicates breakaway corrosion. Interestingly, breakaway corrosion occurred earlier on alloy AF than on alloy APMT, even though twice as much KCl was added to the latter. After breakaway, the TG curve becomes rather flat. It is noted that no linear part of the TG curve was observed in the dry O_2 environment (Fig. 8.11).
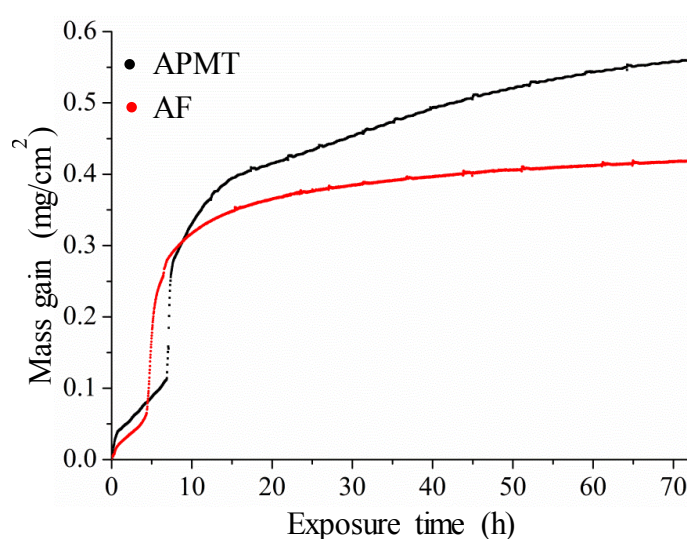
Figure 8.14 In-situ TGA (mass gain vs. exposure time) for alloys AF and APMT at 600 °C in O_2 + H_2O with KCl.

The same crystalline corrosion products were identified as in the corresponding dry exposure (see Papers I and II). K_2CrO_4 was detected after all exposure times except at 168 hours, and the peak intensities were higher than in the dry exposures. In addition, weak peaks were detected on both alloys, indicating the presence of Cr-rich $(FeCr)_2O_3$ or Cr_2O_3.

The IC results showed that chlorine was lost more rapidly from the surface and that the chromate formation was faster than in the corresponding dry exposures (see Papers I and II). As in the dry experiments, the amount of chromate decreased > 24 hours similar to the dry exposures, but the decrease was more pronounced in O_2 + H_2O. This suggests that H_2O was involved in the loss of K_2CrO_4. Similar amounts of chromate were detected on the sample surface after 1 hour of exposure on both AF

51

and APMT even though twice as much KCl was added to alloy APMT than to alloy AF. This suggests that the rate of Reaction (19) is initially not limited by the amount of KCl.

The surface morphology was quite different in $O_2 + H_2O$ than in O_2 when KCl was present. Similar to dry O_2 with KCl, the surface was initially covered by a thin and smooth oxide scale in $O_2 + H_2O$. The numerous metal chloride particles detected in dry O_2 with KCl were, however, replaced with small convex K_2CrO_4 particles (1-3 µm) scattered all over the surface on both alloys (see Fig. 8.15, Papers I and II). Kanthal® AF and APMT show similar corrosion behaviour in $O_2 + H_2O$, and the only detected difference was connected to the greater alloy grain size of AF (see Section 6.1). Chlorides of the alloying elements were detected on AF in the alloy grain boundaries while no such observation was made on alloy APMT (Fig. 8.15). Small amounts of chlorine were, however, detected in the smooth oxide between the K_2CrO_4 particles on APMT after 1 hour of exposure (Fig. 8.15).
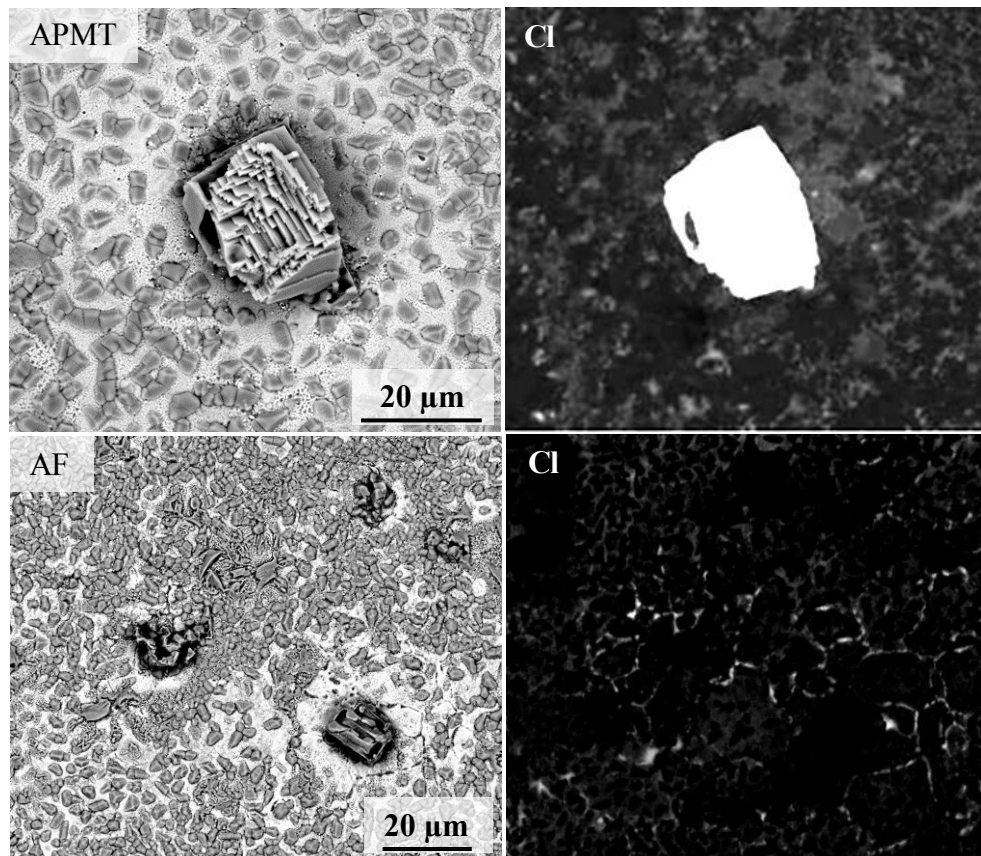
Figure 8.15 SEM-BSE images and EDX chlorine maps of alloy APMT exposed for 1 hour (top) and AF for 3 hours (bottom) at 600 °C in $O_2 + H_2O$ with KCl.

The linear behaviour in Figure 8.14 has been attributed to the K_2CrO_4 formation seen in Figure 8.15. It is argued that the greater chromate formation detected with IC on alloy APMT is connected to the longer linear section seen in Figure 8.14. This is not so surprising since KCl will be present for a longer time on alloy APMT than on AF. With time, breakaway oxidation occurred on both alloys and iron-rich oxide started to grow on the surface. The iron-rich oxide growth appeared to start between the K_2CrO_4 particles; both inward and outward to the adjacent aluminium rich oxide (see Fig. 8.16). An OAZ started to form in the alloy substrate similar to the one observed in dry O_2 with KCl (compare Figs. 8.16 and 8.13). Needle-like particles enriched in aluminium and nitrogen were detected in the OAZ in the $O_2 + H_2O + KCl$ environment.
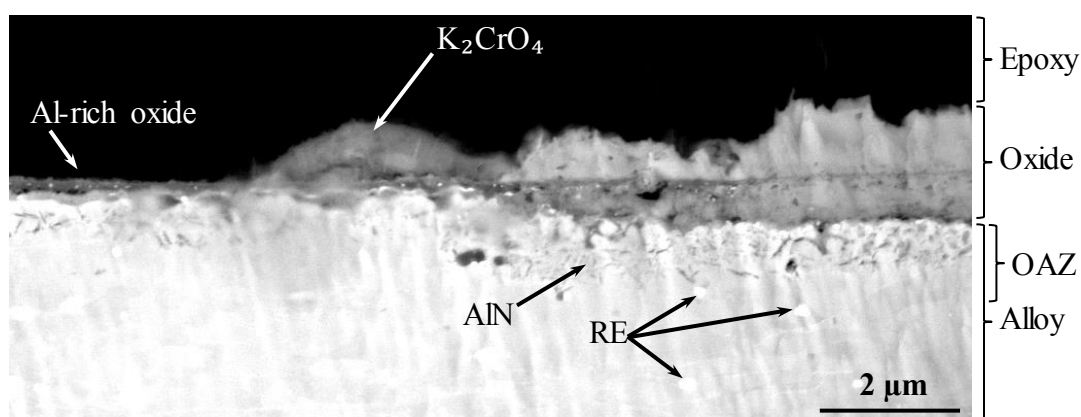
Figure 8.16 SEM-BSE image of alloy APMT exposed at 600 °C for 9 hours in $O_2 + H_2O$ with KCl.

After 24 hours of exposure, thick iron-rich oxide covered most of the surface on both alloys, the oxide thicknesses were similar on alloys AF and APMT (see Papers I, II and III). It was difficult to analyse the elemental distribution in the layered oxide scale with SEM because of the relatively large lateral interaction volume of the electron beam (~0.5 μm), when operated at 10 kV. Consequently, TEM was used to investigate alloy APMT exposed to $O_2 + H_2O + KCl$. Since the TEM foil is very thin (~100 nm) the information from the elemental analysis will originate from a much smaller volume than if SEM/EDX is used (see Section 7.2).

The porous and multi-layered oxide scale formed in $O_2 + KCl$ after 24 hours was replaced with a much denser oxide scale in $O_2 + H_2O + KCl$ for both alloys (Fig. 8.17, Papers I and II). The dense oxide scale seen in Figure 8.17 has a complex layered structure, the upper 2/3 being dominated by iron oxide. The STEM/EDX analyses

showed that the upper part of the scale consisted of almost pure iron oxide. It is suggested that this part corresponds to α-Fe_2O_3, as identified with XRD. In the middle of the iron oxide layer there was an enrichment of Al and Cr together with some K and Si. This enrichment corresponds to the dark band in the middle of the thick oxide to the right in Figure 8.16. It is assumed that this band is remnants from transient oxidation, e.g. during sample heat up. The bottom 1/3 was dominated by chromium oxide, most likely Cr_2O_3. Diffraction lines tentatively attributed to Cr_2O_3 were present in the XRD difractograms (see Paper III). The lower part of the chromia layer was enriched in aluminium. Nitridation of the alloy was present after 24 hours as well as in the dry exposure with KCl. STEM/EDX and nano-AES were used to analyse the small AlN particles (see Paper III).
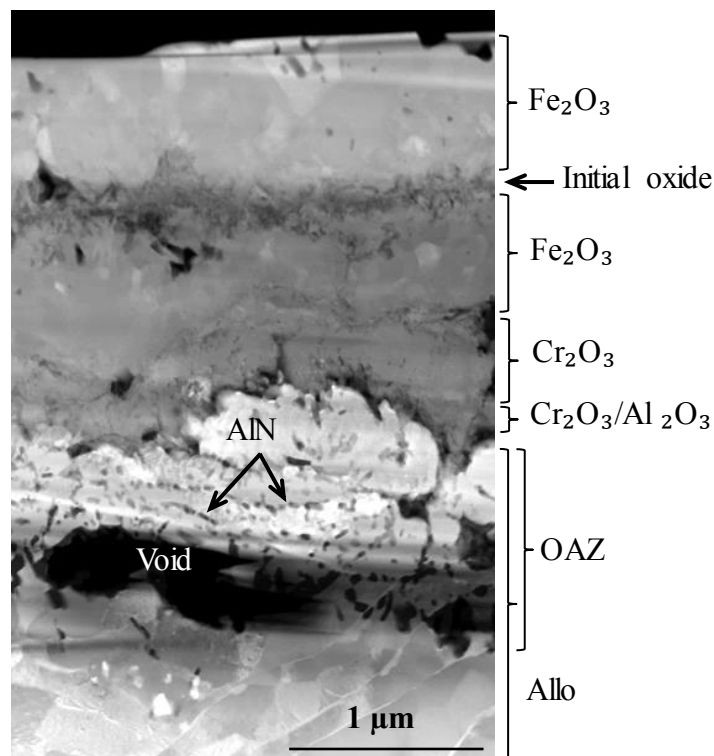
Figure 8.17 STEM-HAADF image of a cross section of alloy APMT exposed at 600 °C for 24h in $O_2 + H_2O$ with KCl.

The formation of nitrides was not detected when the investigated alloys were exposed to $O_2 + H_2O$ in the absence of KCl. AlN particles were observed after exposure times exceeding 1 hour in $O_2 + H_2O$ with KCl at 600 °C. While the amount of nitride and the penetration depth increased between 9 and 24 hours, the nitridation of the alloy appeared not to have progressed further between 24 and 168 hours.

54

The STEM micrographs in Figure 8.18 show the alloy substrate directly beneath the oxide after 168 hours exposure. It appeared that AlN had been partly converted to alumina at this stage. Figure 8.18 shows that the needle-like AlN particles were located further down in the alloy while larger alumina particles (with a dark contrast) that tended to align were present in the upper part of the OAZ. The needle-like particles were larger and fewer in numbers after 168 hour than after 24 hours. The STEM/EDX analyses showed that some of the particles consisted of a mixture of Al_2O_3 and AlN.
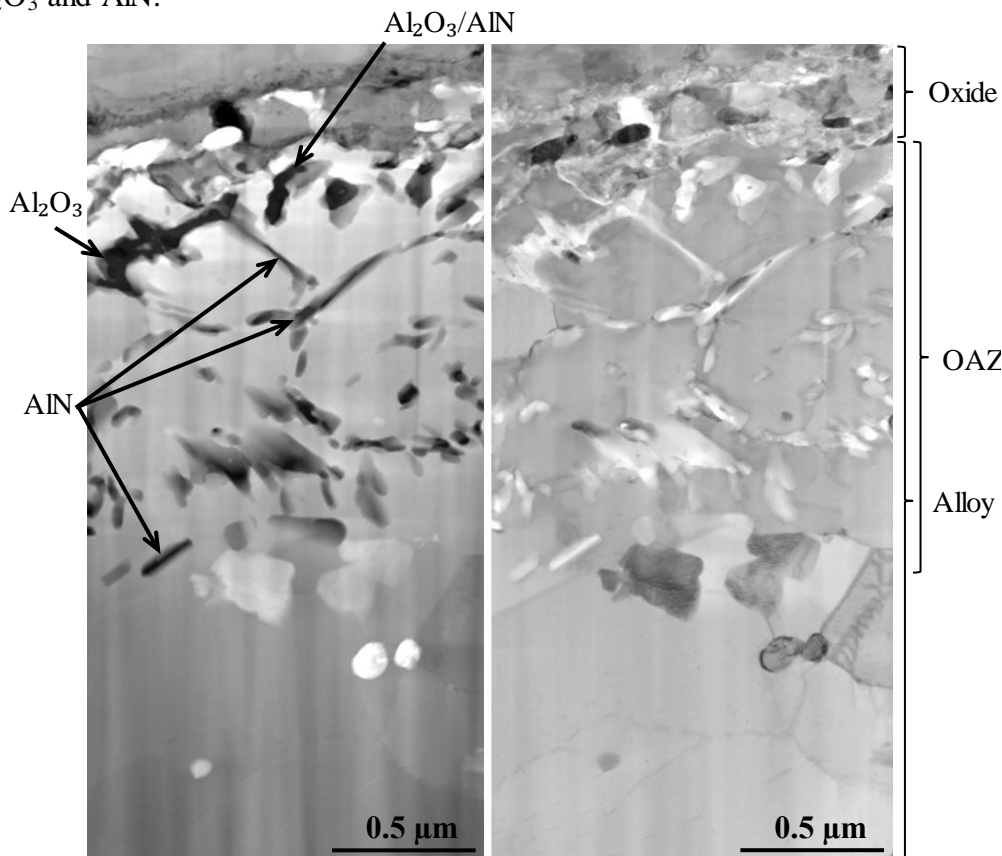
Figure 8.18 STEM-HAADF image (left) and STEM-BF (right) of a cross section of alloy APMT exposed at 600 °C for 168 hours in $O_2 + H_2O$ with KCl.

The N_2 molecule is quite stable and only dissociates with difficulty on oxide surfaces at 600 °C, alloy nitridation implies that the oxide scale was permeable to N_2 molecules. It is argued that the rapid corrosion attack creates pathways for N_2 molecules to penetrate through the oxide scale. The N_2 molecules that penetrate the scale subsequently dissociates at the metal surface and dissolve into the alloy. The present results show that nitridation interferes with the oxidation behaviour of the

alloy. Thus, as a result of the depletion Al in the alloy substrate due to AlN precipitation, the alloy will have less chance to form a protective alumina scale.

Minor amounts of chlorine were detected on the samples exposed to 1, 9 and 24 hours in O_2 + H_2O + KCl (Fig. 8.15 and Papers I, II and III). The degree of alloy chlorination was much less than in dry O_2 with KCl.

While Reactions (19) and (23) both contribute to the formation of chromate, it is suggested that the main source of chromate formation in the present case is Reaction (19) because it is favoured by a high concentration of water vapour. It is believed that Reaction (19) consumes almost all the available KCl on the surface and diminishes the abilities of Reaction (23) to chlorinate the alloy. Thus a lower degree of alloy chlorination is expected when water vapour is present.

Several researchers have reported that high temperature alloys can be chlorinated in O_2-containing gases with HCl(g) [45, 64]. One may argue that alloy chlorination is caused by the HCl(g) formed through Reaction (19). This is not considered to be valid since the flowing gas will dilute the HCl generated through Reaction (19) and transport it away from the sample.

8.4 The effect of pre-oxidation on KCl-induced corrosion, (Papers II and VI)

8.4.1 Pre-oxidation at 700 °C - exposed to O_2 + H_2O + KCl at 600 °C, (Paper II)

Pre-treated samples (700 °C, 24h (see Section 8.1.2)) were exposed for 1, 24 and 168 hours to O_2 + H_2O with KCl at 600 °C. Pre-oxidation at this rather low temperature had a strong beneficial effect on the high temperature corrosion of alloy APMT in the presence of KCl. One hour of exposure with KCl at 600 °C produced little change in surface morphology compared to the unexposed sample with the added KCl (compare Figs. 6.4 and 8.19). No additional compounds were detected with XRD and IC after 1 hour but the SEM/EDX analyses showed the presence of a few K_2CrO_4 particles on the sample surface (Fig. 8.19). This is in marked contrast to the alloy not subjected to pre-oxidation where K_2CrO_4 particles were present all over the sample surface after 1 hour (see Fig. 8.15).
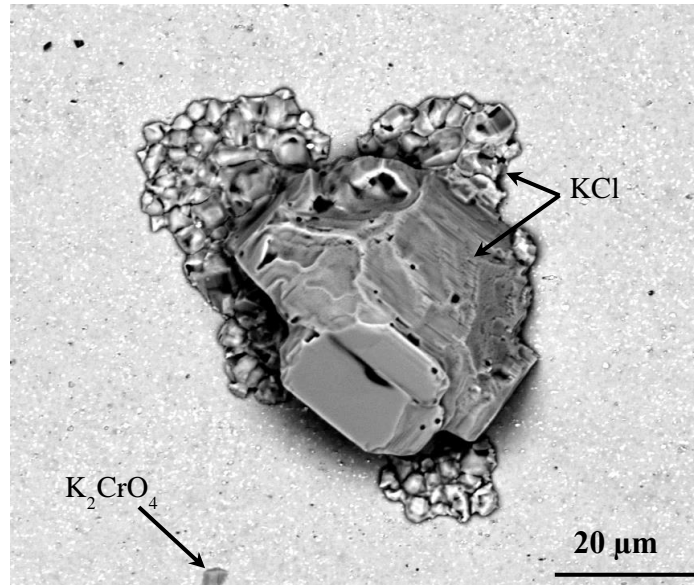
Figure 8.19 SEM-BSE image of pre-oxidised alloy APMT (24h, 700 °C) exposed at 600 °C for 1 hour in $O_2 + H_2O$ with KCl.

The samples appeared almost unaffected after 24 hours of exposure with no signs of KCl on the surface (Fig. 8.20 and 8.21). The optical images in Figure 8.20 shows that the protective alumina scale tends to fail in connection to the drilled hole and the edges of the sample.
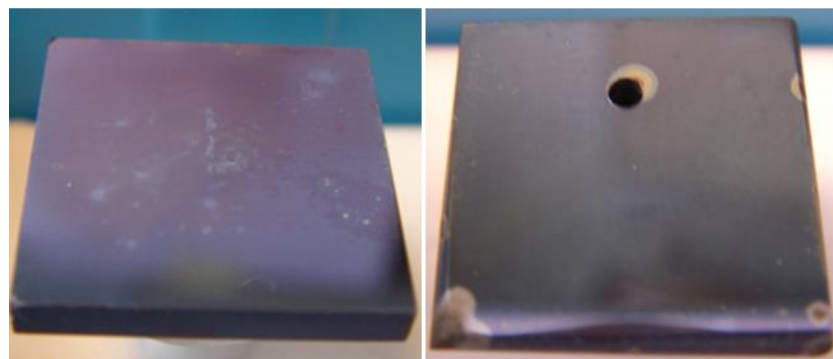
Figure 8.20 optical images of pre-oxidised alloy APMT (24 hours, 700 °C) to the left and subsequently exposed at 600 ° C with KCl for 24 hours in $O_2 + H_2O$ to the right.

The pre-formed aluminium-rich oxide scale was not totally inert to KCl-induced corrosion. K_2CrO_4 particles were scarcely located on the sample surface while no evidence of KCl was found after 24 hours of exposure with KCl (Fig. 8.21). The Cr_2O_3 needed for Reaction (19) to proceed is believed to originate from the chromium enrichment observed in the aluminium-rich oxide scale formed during the pre-oxidation (Paper II).
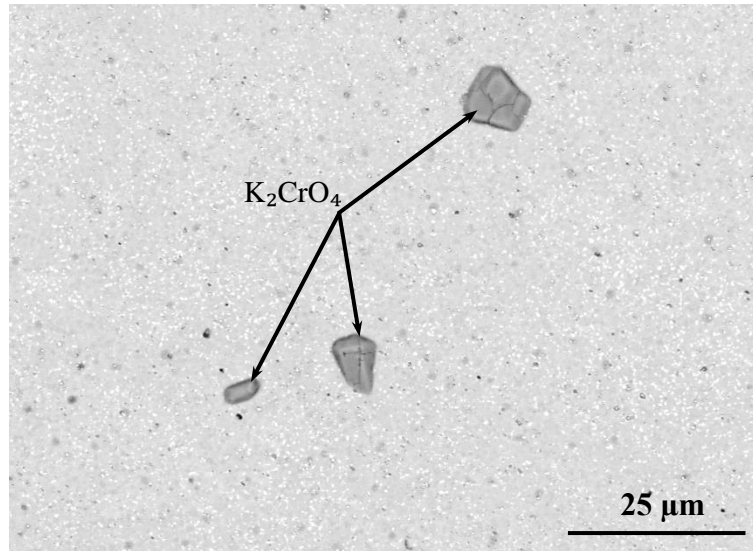
Figure 8.21 SEM-BSE images of pre-oxidised alloy APMT (24 hours, 700 °C) exposed at 600 ° C with KCl for 24 hours in $O_2 + H_2O$.

8.4.2 Pre-oxidation at 900 °C - exposed to $O_2 + H_2O + KCl$ at 600 °C, (Paper VI)

Alloy APMT was pre-oxidized at 900 °C for 1 and 24 hours in $O_2 + N_2$. Micrographs of the cross-sections of the pre-formed alumina scales are shown in Figure 8.22, for detailed information on the alumina scales see Section 8.1.3 and Paper VI. The pre-treated samples were subsequently exposed with KCl in $O_2 + H_2O$ for 24-hour cycles until breakaway corrosion was observed. It should be mentioned that twice as much KCl was used as in the previous experiments in order to accelerate the corrosion process.
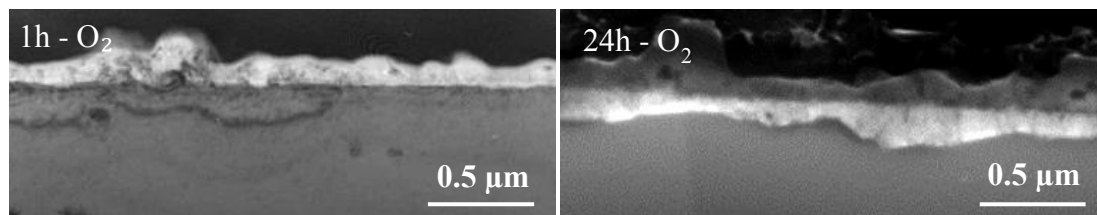
Figure 8.22 TEM-BF (left) and SEM-SE image (right) of cross-sections of pre-oxidised alloy APMT for 1 hour and 24 hours at 900 °C in an O_2 environment.

8.4.2.1 Corrosion of samples pre-oxidized for 1 hour at 900 °C

The alumina scale formed during 1 hour of pre-oxidation at 900 °C failed during the first corrosion exposure. The entire surface of the sample was affected by breakaway oxidation as shown in Figure 8.23.

The top-view micrograph in Figure 8.23 shows a typical area of a corroded surface with a former KCl particle in the middle of the micrograph, surrounded by a cracked

58

alumina scale with an iron-rich oxide on top. Corrosion products similar to the exposure without pre-oxidation in $O_2 + H_2O$ with KCl were observed. Iron-rich oxide, most likely hematite (α-Fe_2O_3), was detected together with potassium chromate particles almost all over the surface of the sample on top of the pre-formed alumina scale. In addition, SEM/EDX point analyses showed high amounts of chlorine together with low amounts of potassium in certain areas in top-view mode. Thus, transition metal chloride is assumed to be incorporated into the scale after the exposure.
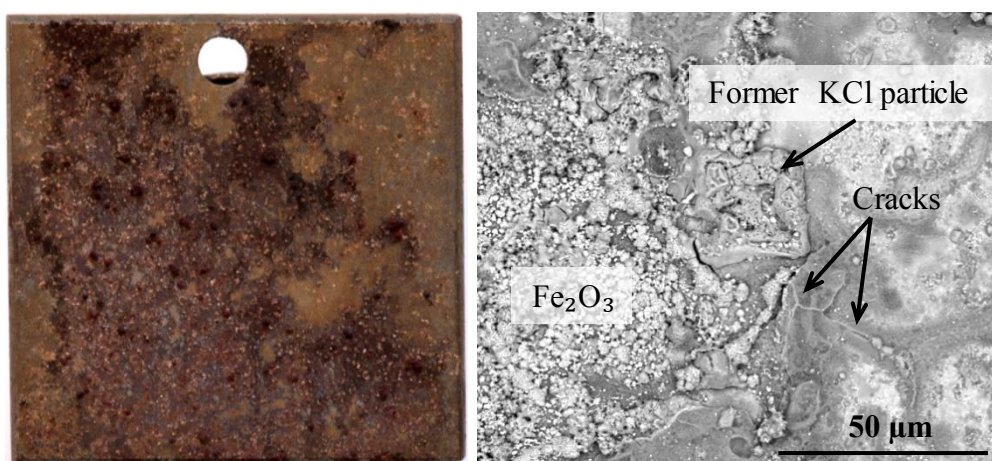
Figure 8.23 Optical image (left) and SEM-BSE image (right) of the pre-oxidized alloy APMT (1 hour, 900 °C) exposed for 1 corrosion exposure ($O_2 + H_2O$ + KCl at 600 °C for 24 hours).

A cross-section of the above corroded sample is shown in Figure 8.24. The layered oxide scale has similarities to the cross-section obtained without pre-oxidation after 24 hours (see Figs. 8.24 and 8.17). The major difference is that the initial oxide in Figure 8.17 has been replaced with the alumina scale from the pre-oxidation stage. However, the alumina layer contained several cracks and relatively thick layers of iron-rich oxide had formed in connection to these cracks, both above and below the alumina, forming a continuous layer in some areas. A layer of chromium-rich oxide was located below the iron-rich oxide closest to the alloy. The K_2CrO_4 particles detected in top view can also be observed in the cross-section in Figure 8.24 and they were always found on top of the cracked alumina layer, and were associated with iron-rich oxide. Just beneath the chromium-rich oxide layer there was an OAZ in the alloy substrate containing small needle-like particles. The needle-like particles are suggested to consist of aluminium nitride (AlN) similar to the findings in Paper III.
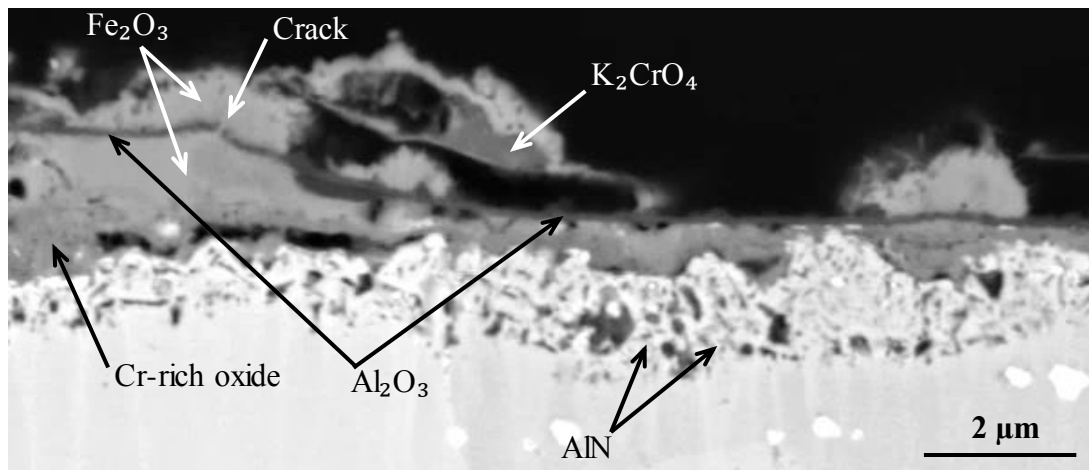
Figure 8.24 SEM-BSE micrograph of a cross-section of the pre-oxidized alloy APMT (1 hour, 900 °C) exposed for 1 corrosion exposure (O_2 + H_2O + KCl at 600 °C for 24 hours).

8.4.2.2 Pre-oxidation at 900 °C for 24 hours

Corrosion resistance was improved substantially by the pre-oxidation of the alloy at 900 °C for 24 hours (compare Figs. 8.25 and 8.23). The surface of the sample was almost featureless, similar to the results after pre-oxidation at 700 °C for 24 hours (Fig. 8.20).
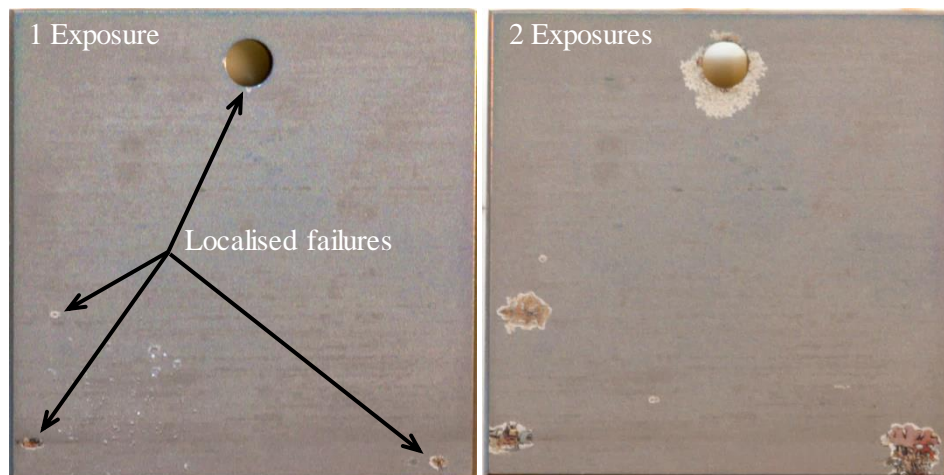
Figure 8.25 Optical images of the pre-oxidized alloy APMT (24 hours, 900 °C) exposed for 1 and 2 corrosion exposures (O_2 + H_2O + KCl at 600 °C for 24 hours).

The alumina scale had, however, failed at a few locations. The failures were located both on the polished surface (down to 1 μm) and in connection to the ground (320 SiC paper) edges.

The second corrosion exposure resulted in the lateral growth of the areas that suffered localised attack during the first corrosion exposure (Fig. 8.25). The areas that exhibited localised corrosion were similar to the areas described above (1 hour pre-

oxidation). Thus, cracks can be seen in the alumina layer, and iron-rich oxide and K_2CrO_4 particles are associated with the cracks (Fig. 8.26). The presence of α-Fe_2O_3 and K_2CrO_4 was verified using XRD (Paper VI).
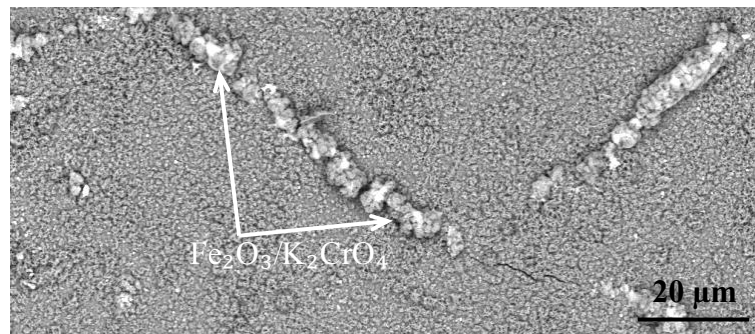
Figure 8.26 SEM-BSE top-view image of the pre-oxidized alloy APMT (24hours, 900 °C) exposed for two corrosion exposures ($O_2 + H_2O + KCl$ at 600 °C for 24 hours).

The end of a newly formed crack far away from the corrosion front was investigated in order to understand how the corrosion spread laterally over the surface of the sample. A TEM specimen was prepared at the crack tip, normal to the direction of the crack. An image of the TEM sample before the final thinning is shown in Figure 8.27, showing a wedge-shaped oxide underneath the alumina layer.
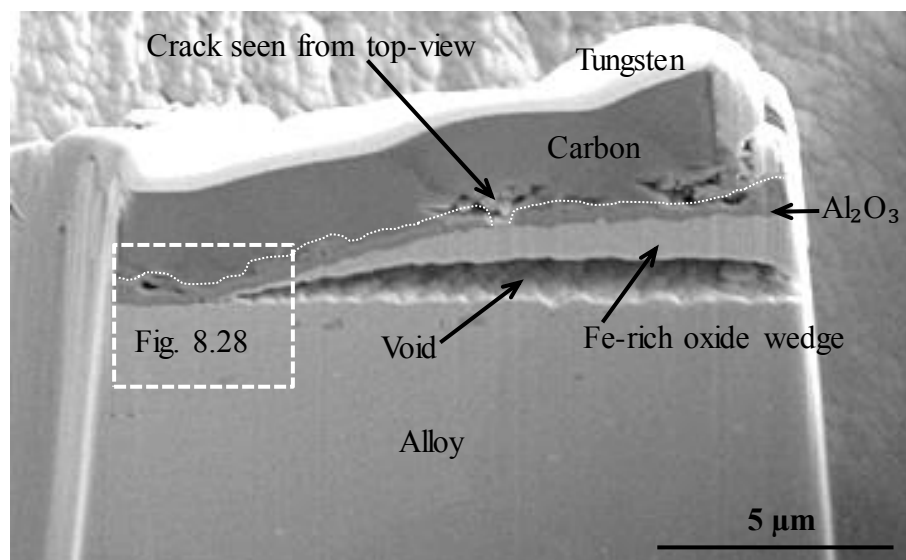
Figure 8.27 SEM-SE image of TEM sample before the final thinning of the pre-oxidized alloy APMT (24 hours, 900 °C) exposed for 2 corrosion exposures ($O_2 + H_2O + KCl$ at 600 °C for 24 hours).

SEM/EDX analysis showed that the oxide wedge was iron-rich. Figure 8.27 shows that the alumina/iron oxide scale has partly detached from the alloy. The point at which the alumina scale has detached from the alloy coincides with the tapered end of

61

the iron rich oxide wedge and is assumed to correspond to the corrosion front. The boxed area in Figure 8.27 is shown in the STEM micrograph of the corrosion front in Figure 8.28.
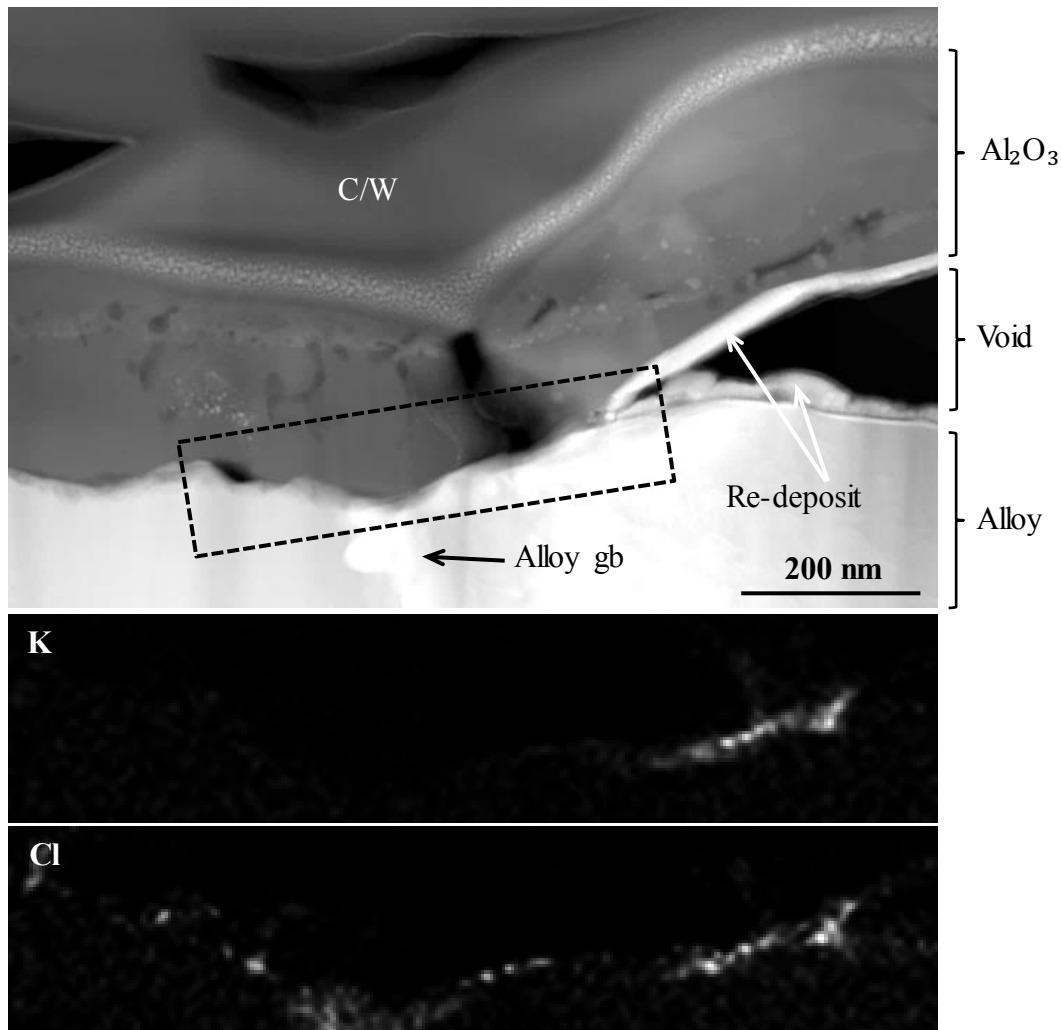
Figure 8.28 Elemental maps of the boxed area in the STEM-HAADF micrograph of pre-oxidized alloy APMT (24 hours, 900 °C), exposed for 2 corrosion exposures ($O_2 + H_2O + KCl$ at 600 °C for 24 hours).

The interface between the alumina scale and the substrate was analysed further close to the corrosion front. The alumina scale was well adherent to the alloy substrate to the left of the corrosion front and no signs of porosity were observed. Potassium and chlorine were detected in the alumina/alloy interface (boxed area in Fig. 8.28) in addition to the signal from the alumina scale and alloy substrate. The STEM/EDS elemental maps in Figure 8.28 show that potassium was enriched at the interface between the alumina scale and the alloy close to the corrosion front, while chlorine was detected throughout the whole alumina/alloy interface. In addition, the chlorine map indicates that chlorine was also enriched at the alloy grain boundary (Fig. 8.28).

62

8.4.3 Pre-oxidized at 1100 °C - exposed to $O_2 + H_2O + KCl$ at 600 °, (Paper VI)

Alloy APMT was pre-oxidised at 1100 °C for 1 and 24 hours in $O_2 + N_2$. The pre-formed alumina scales were two-layered with a scale thickness of 0.4 and 1.5 μm, for additional information see Paper IV and Section 8.1.4. The pre-treated samples were subsequently exposed with KCl in $O_2 + H_2O$ for 24-hour cycles until breakaway corrosion was observed.

8.4.3.1 Corrosion of samples pre-oxidized for 1 hour at 1100 °C

Pre-oxidation at 1100 °C for one hour improved the corrosion resistance of the sample compared to pre-oxidation at 900 °C for 1 hour (Figs. 8.29 and 8.23). The alumina scale had, however, failed during the first corrosion exposure. A substantial amount of the alloy surface has been affected by breakaway corrosion and the oxide scale is no longer considered as protective at this stage. The corrosion products were analysed and it was found that the corrosion attack was similar to the one described above at 900 °C.

Figure 8.29 Optical image of the pre-oxidized alloy APMT (1 hour, 1100 °C) exposed for 1 corrosion exposure ($O_2 + H_2O + KCl$ at 600 °C for 24 hours).

8.4.3.2 Corrosion of samples pre-oxidized for 24h at 1100 °C

Not surprisingly, the sample pre-oxidised at the highest temperature and the longest time showed the highest corrosion resistance towards KCl-induced corrosion. The samples subjected to 24 hours of pre-oxidation at 1100 °C showed no signs of corrosion after the first two corrosion exposures (not shown). However, the third corrosion exposure, shown in Figure 8.30, caused the alumina scale to fail locally; the corrosion morphology was found to be similar to that described for the other pre-oxidized samples (see above). The corrosion seemed to be initiated in connection to

the sample edges. This was in contrast to the samples pre-oxidized for 24 hours at 900 °C in which corrosion sometimes started on the polished surface, far away from the edges. After initiation, the corroded areas grew laterally over the surface; see optical images after the third and fourth corrosion exposures (Fig. 8.30). Again, the corrosion products were analysed and it was concluded that the same corrosion reactions were present as on the other samples (see Paper VI for more detailed information).
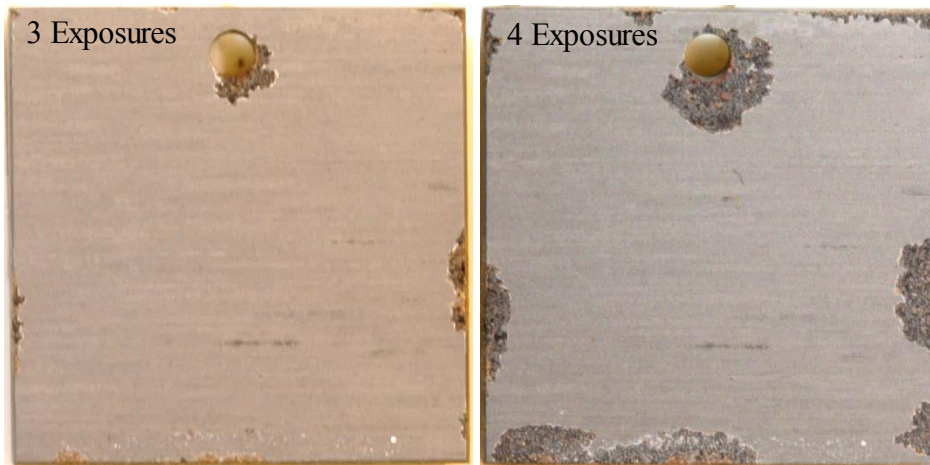
Figure 8.30 Optical images of the pre-oxidized alloy APMT (24 hours, 1100 °C) exposed for 3 and 4 corrosion exposures ($O_2 + H_2O + KCl$ at 600 °C for 24 hours).

A TEM sample was prepared from a location far away from the corroded areas on the sample that experienced 4 consecutive corrosion exposures.
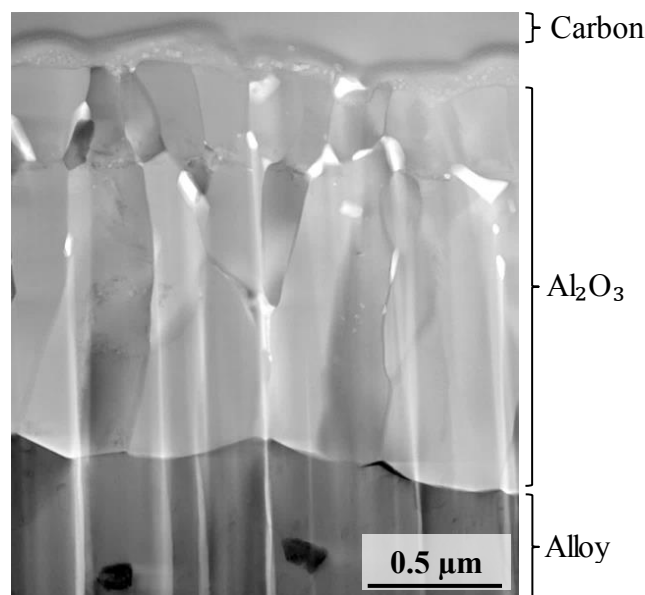
Figure 8.31 STEM-BF micrograph of a cross-section of pre-oxidized alloy APMT (24 hours, 1100 °C), exposed for 4 consecutive corrosion exposures ($O_2 + H_2O + KCl$ at 600 °C for 24 hours). The TEM specimen was obtained far away from the corrosion front.

No signs of cracks were observed in the top-view of the investigated area. Figure 8.31 shows a STEM-BF image of a cross-section showing an adherent alumina layer. No corrosive species, e.g. Cl or K were detected using EDX analyses either at the alumina scale/alloy interface or in the oxide grain boundaries.

8.4.4 Summary/Discussion Pre-oxidation and KCl-induced corrosion

The resistance towards KCl-induced corrosion of the pre-formed alumina scales was: (900 °C, 1 hour) < (1100 °C, 1 hour) < (900 °C, 24 hours) < (1100 °C, 24 hours). Corrosion and the associated break-up of the alumina scales were initially highly localized and much of the sample surface was seemingly unaffected. However repeated exposures with KCl caused the corrosion to spread laterally over the surface. The lateral movement of the "corrosion front" is assumed to be associated with the spreading of cracks in the alumina scale.

The absence of any corrosive species, e.g. potassium and chlorine at the alumina/alloy interface (Fig. 8.31) shows that the pre-formed alumina scale was protective towards KCl-induced corrosion at 600 °C. However, the above results suggest that KCl-induced corrosion is initiated at flaws in the alumina layer and that the intact alumina layer is impermeable to attack. The fact that KCl was detected at the alloy/alumina scale interface close to the corrosion front in Figure 8.28 shows that KCl is highly mobile in the investigated environment. The same image shows that chlorine penetrated far ahead of potassium, which means that transition metal chlorides ($FeCl_2$ and/or $CrCl_2$) were present at the alumina/alloy interface. Chlorination with HCl(g) (generated by Reaction (19)) is not considered to be the source of subscale chloride in this case because the HCl generated by Reaction (19) forms at the scale/gas interface and will be transported away from the sample by the flowing gas. Again, it is suggested that the formation of sub-scale transition metal chloride is part of an electrochemical reaction (Reaction (23), see Section 8.2) involving the alloy substrate, KCl, Cr_2O_3 and O_2.

According to the above observations, the products of Reaction (23) accumulate at the scale/gas interface (K_2CrO_4) and at the scale/alloy interface ($FeCl_2$). It is argued that if all the reactants are present, Reaction (23) cannot run if the α-alumina scale is intact because the alumina scale constitutes an effective barrier towards the diffusion of ions (Fe^{2+}, Cl^-). Once the scale cracks, the situation changes. It is suggested that,

when a crack or similar flaw in the alumina scale is present, KCl immediately enters it by surface diffusion, forming an adsorbed layer on the exposed alumina in the crack. This is illustrated in steps I and II in Figure 8.32.
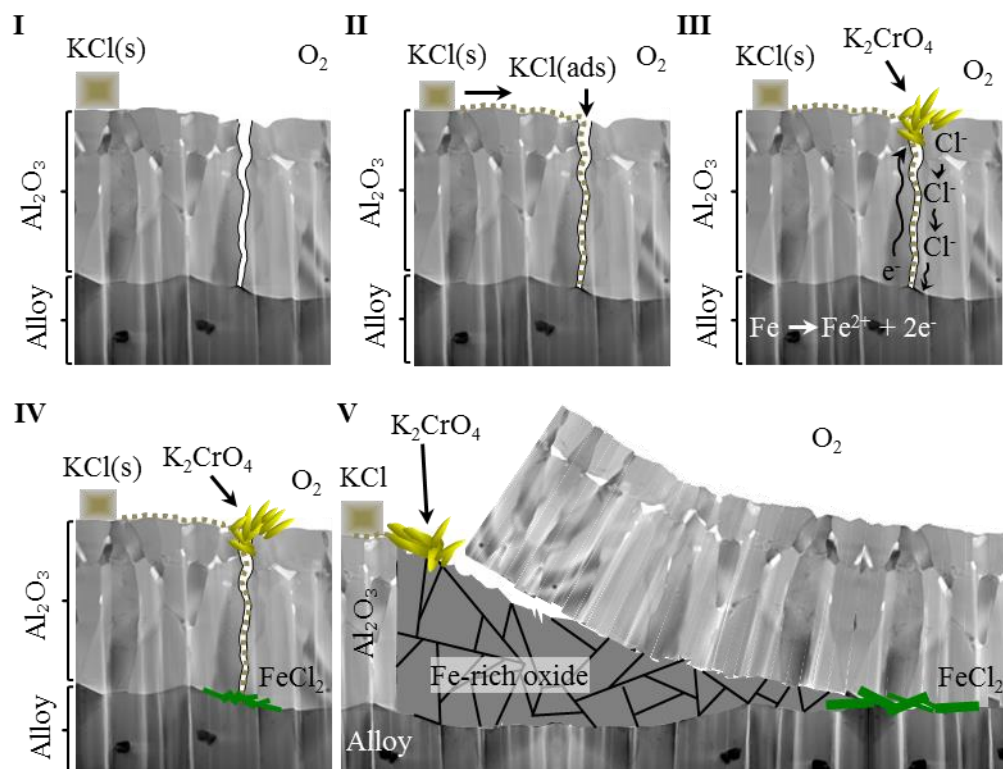
Figure 8.32 Illustration of the initiation of the corrosion attack coupled to Reaction (23).

It is suggested that KCl in the crack provides the medium for the ionic current, i.e., transport of chloride ions, which is necessary for Reaction (23) to run. The electronic current is suggested to be carried by the alumina (Fig. 8.32, step III).

The scenario in Figure 8.32 is based on the physical properties, i.e., conductivities, reported for alkali chlorides and α-alumina (see Paper VI). Thus, in the presence of a KCl "salt bridge" across the scale, the anodic formation of $FeCl_2$ at the scale/alloy interface becomes coupled to the formation of potassium chromate at the scale/gas interface (Fig. 8.32, step IV).

The formation of transition metal chloride at the scale/alloy interface is associated with a large expansion in volume. It is assumed that this is the primary cause behind the cracking and de-cohesion of the alumina scale. The scale de-cohesion and cracking is expected to continue for as long as KCl is present. The region behind the

crack tip becomes exposed to the gas environment after the formation of transition metal chloride, resulting in the rapid growth of iron-rich oxide below the alumina layer. The growth of the iron oxide layer also produces a expansion in volume that further contributes to cracking of the alumina scale (Fig. 8.32, step V).

The fact that the pre-oxidation performed at 900 °C for 1 hour showed the least corrosion resistance of the four conditions might be connected to the oxide nodules that were described in Section 8.1.3. Figure 8.7 clearly shows that the inward-growing α-Al$_2$O$_3$ layer was not continuous all over the surface.

The observation that the KCl-induced corrosion of the pre-oxidized samples mainly started at the sample edges prompted an investigation of the alumina scale formed on the sample edges. The sample pre-oxidized for 24 hours at 1100 °C was investigated further after the pre-treatment. While SEM/EDX top-view imaging of the polished surface showed a very smooth alumina scale, the grinded sample edges revealed small (~5-10 μm in size) iron-rich oxide nodules immersed in the alumina scale (Paper VI, Fig. 12). A cross-section of one of the oxide nodules showed that there was a continuous alumina scale underneath the iron-rich feature. The alumina layer underneath the iron-rich oxide was, however, significantly thinner than the alumina scale in general.

It is argued that if only one of these (an estimated 200 on one sample) Fe-rich features lack a continuous alumina layer underneath, then it would be susceptible to KCl-induced corrosion in a way similar to the one shown in Figure 8.32. In addition pre-oxidation at lower temperatures and shorter times would not favour the formation of a continuous alumina layer underneath the iron-rich features. This might explain why the KCl-induced corrosion resistance of the pre-formed alumina scales was: (900 °C, 1 hour) < (1100 °C, 1 hour) < (900 °C, 24 hours) < (1100 °C, 24 hours).

8.5 Exposures in a waste-fired CHP boiler, (Paper VII)

The environment in a full-scale waste-fired power boiler is much more complex than the environment in a simplified laboratory studies. In order to evaluate the validity of the findings in the laboratory studies, corrosion tests were carried out in a 75MW combined heat and power (CHP) boiler (Fig. 8.33). The outlet steam temperature and pressure at the maximum continuous rate was 450 °C and 65 bar. The fuel consisted mainly of domestic waste (~ 57 %) and industrial waste (~ 38 %), the remaining part

consisted of different types of bio fuels. The FeCrAl alloy APMT and the FeNiCr alloy Sanicro 28 (see Paper VII for the nominal chemical composition) were exposed to the boiler, the latter alloy was added as a reference. The FeCrAl alloy was exposed with and without pre-oxidization prior to exposure. The pre-oxidation time and temperature were chosen to be 24 hours and 1100 °C based on the resistance towards KCl-induced corrosion of the alumina scales studied in the laboratory (see Section 8.4).
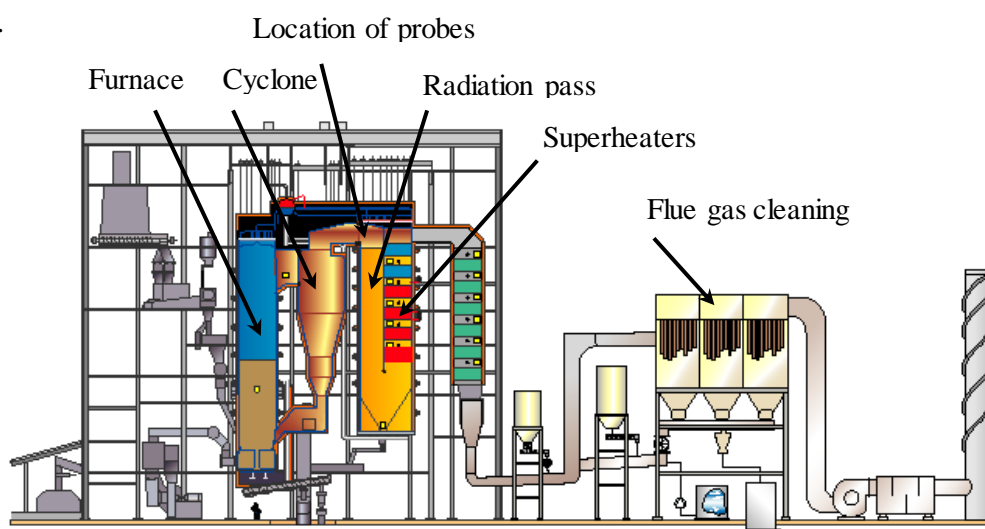
Figure 8.33 Schematic image of the waste-fired 75 MW boiler P14 at Händelö in Norrköping.

Internally air-cooled probe exposures were performed for 24, 400 and 1000 hours at 600 and 700 °C. The probes were installed at the same time in the boiler and were located between the cyclone and the radiation pass, and the corresponding flue gas temperature was about 850 °C (Fig. 8.33). The corrosion probes were not located at exactly the same location since the probes were exposed simultaneously. The amounts of HCl and SO_2 were measured in the flue gas in the boiler with Fourier Transform Infrared Spectroscopy (FTIR) during 24 hours, and it was found that the HCl was quite constant at about 250 ppm and the SO_2 was usually lower than 20 ppm.

The metal loss measurements after 400 and 1000 hours at 600 and 700 °C showed that the rate of corrosion slowed down with time, and that the metal losses were about the same after 400 and 1000 hours. Moreover, a comparison of the metal loss measurements after exposure at 600 and 700 °C (metal temperature) showed that there was no significant influence of temperature on the rate of corrosion. The findings do not show any beneficial effect of pre-oxidation at 1100 °C. Alloy APMT, on the other hand, showed 2-4 times lower metal loss than the reference FeNiCr alloy in all four exposure conditions.

Deposit and corrosion products from the FeCrAl and the pre-oxidised FeCrAl samples were collected, pestled and analysed using XRD. The analysis was dominated by deposit compounds such as NaCl, KCl and CaSO$_4$. In addition, KAlSiO$_4$ was detected in the deposit/corrosion product mixture at the higher exposure temperature. Fe$_2$O$_3$ and Cr$_2$O$_3$ were detected on all samples exposed at 600 and 700 °C while no type of crystalline alumina was recorded.

Figure 8.34 shows a micrograph of a roughly 500 µm thick deposit layer on top of the alumina scale formed during pre-oxidation after 24 hours of exposure in the boiler at 600 °C. The pre-formed alumina scale has detached from the alloy substrate and consequently has lost its protective properties after only 24 hours in the aggressive environment. The detached alumina layer was cracked and an iron, chromium-rich oxide had grown inward and outward adjacent to the pre-formed alumina layer. Minor amounts of metal chlorides were detected below the alumina layer. The deposit layer contained mainly Ca, S, K, Na and Cl according to SEM/EDX, which correlates well with the NaCl, KCl and CaSO$_4$ detected with XRD.
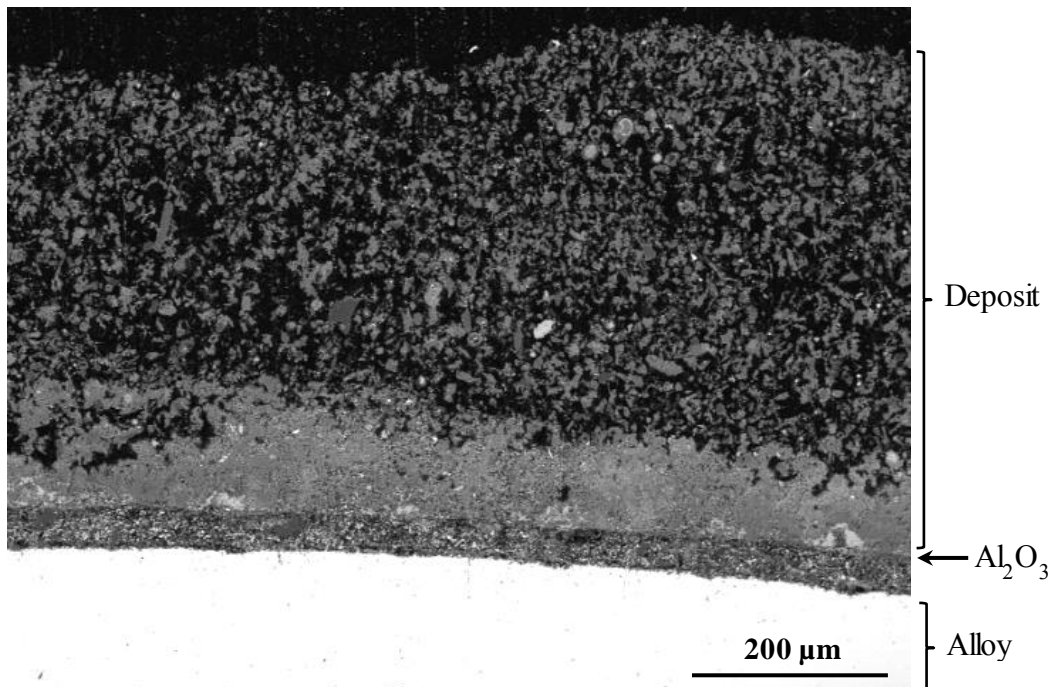
Figure 8.34 SEM-BSE micrograph of a cross-section of the deposit layer on top of the pre-oxidized alloy APMT (24 hours, 1100 °C) exposed for 24 hours at 600 °C.

The pre-formed alumina scale also failed after 24 hours of exposure at 700 °C in the boiler. Iron oxide had been formed, according to SEM/EDX, in connection to cracks in the pre-formed alumina layer, both above and below the alumina (Fig. 8.35 and Paper VII). Below the cracked alumina layer, a complex layered oxide scale was present in the shape of an oxide wedge. The oxide wedge was dominated by iron and chromium underneath the alumina layer in connection to the crack.
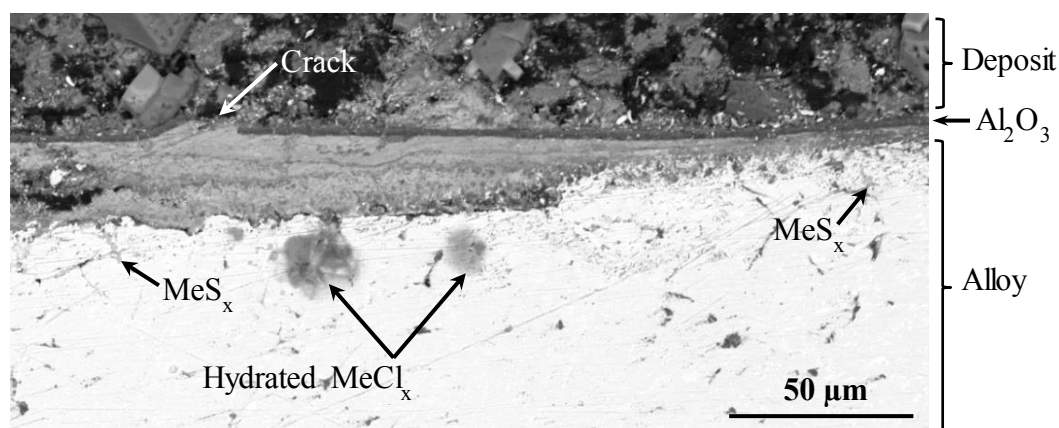
Figure 8.35 SEM-BSE micrograph of a cross-section of pre-oxidized alloy APMT (24 hours, 1100 °C) exposed for 24 hours at 700 °C.

The oxide scale had become enriched in chromium and aluminium closer to the alloy substrate and at the tip of the oxide wedge (far right in Figure 8.35). Minor amounts of hydrated transition metal chlorides were detected in the cross section at the scale/alloy interface. Transition metal sulphide was detected at the scale/alloy interface and in the Cr-rich oxide below the alumina scale to the right in the micrograph in Figure 8.35. The deposit layer present on top of the oxide scale contained the same compounds as after the 600 °C exposure (see above).

No sign of the pre-formed alumina scale was detected after 1000 hours of exposure in the boiler at 600 and 700 °C. The microstructure of the scales was similar on the exposed samples with and without the pre-oxidation. No pure alumina scale was formed at any of the temperatures. Since the alumina scale from the pre-treatment had failed initially, the alloys were expected to corrode in a similar way after longer exposure times.

A mixed oxide of iron, chromium and aluminium was formed after 1000 hours at 600 °C (Fig. 8.36). A thick layer, about 100-200 μm, of transition metal chloride was present between the oxide layer and the alloy substrate (Fig. 8.36 and Paper VII).

70

Large areas lacked the top part of the scale (the layered oxide), i.e. the scale consisted only of the layer of transition metal chloride. Consequently, the present oxide scale is not considered protective at this stage. The SEM/EDX elemental map for sulphur in Figure 8.36 shows that the mixed oxide layer contained sulphur. It is concluded that transition metal sulphide or sulphate had been incorporated into the oxide scale during the exposure.
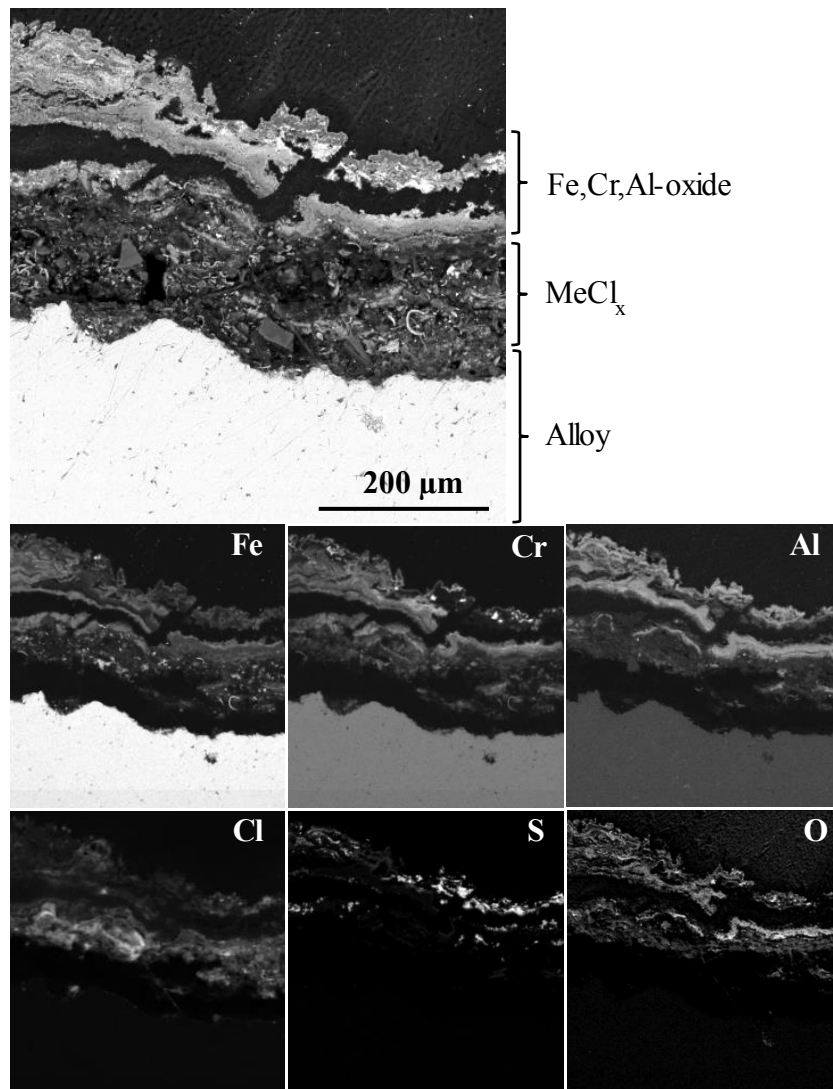
Figure 8.36 SEM-BSE micrograph of a cross-section of alloy APMT exposed for 1000 hours at 600 °C.

A relatively dense oxide scale was observed after 1000 hours of exposure at 700 °C (Fig. 8.37). The scale consisted of three consecutive oxide layers, according to the SEM/EDX elemental maps in Figure 8.37. At the scale/gas interface, an iron-rich oxide layer dominated, overlying a chromium-rich layer, while an aluminium-rich oxide layer was present closest to the alloy. An Oxidation Affected Zone (OAZ) was

71

observed that contained needle-shaped Al–rich particles (see Fig. 8.37). EDX point analysis revealed that the Al-rich particles contained large amounts of nitrogen, indicating that they consisted of AlN. The AlN particles were larger at the bottom of the OAZ. The microstructure of the scale was quite similar to the one formed in the laboratory exposure with KCl at 600 °C (compare Figs. 8.37 and 8.17). Sulphur-rich areas were present at the interface between the oxide scale and the OAZ. SEM/EDX point analyses showed that the larger sulphur-rich areas contained Cr and Fe while no Mo (K_{a1}) signal was present in the analysis. The evidence for chlorine in the scale was scarce in comparison to the exposures at 600 °C. The arrow in the micrograph in Figure 8.37 shows an area where there was evidence of chlorine and sulphur, and that there was an absence of alkali metals. This was interpreted as a mixture of transition metal chlorides and sulphides or sulphates.
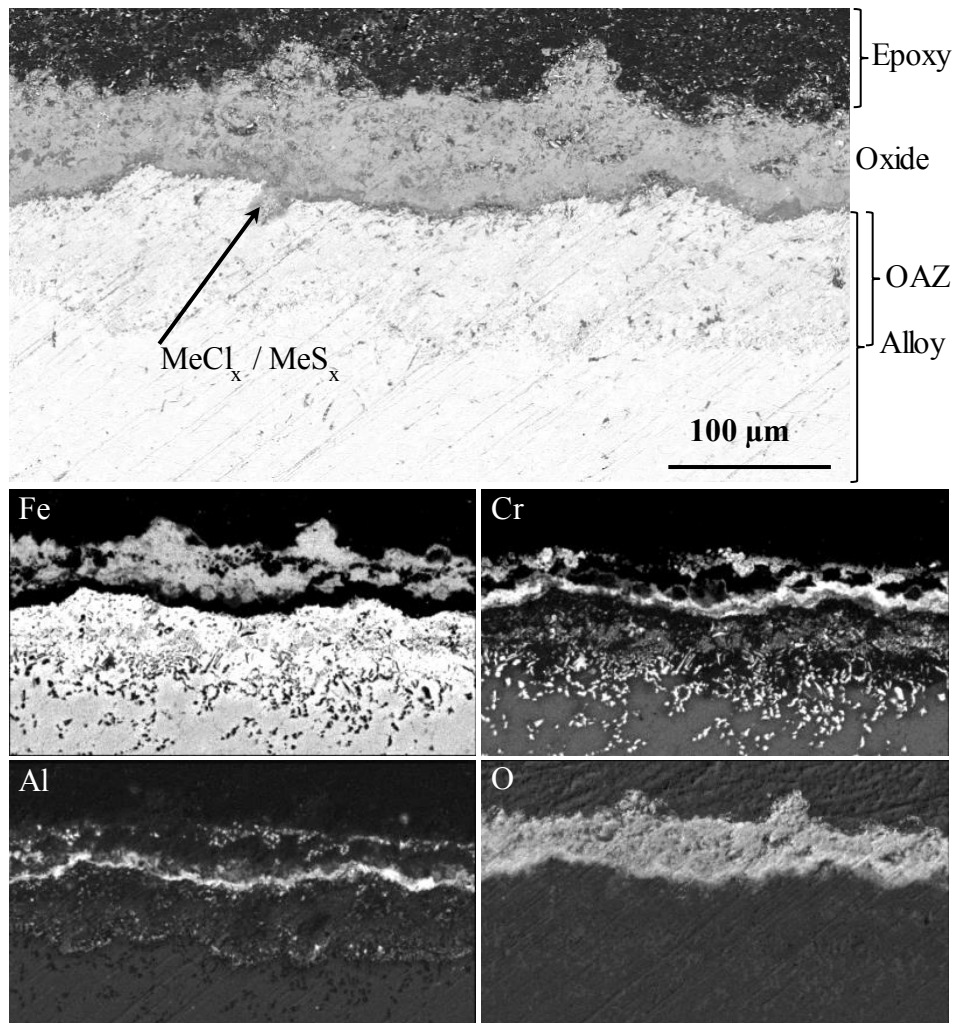
Figure 8.37 SEM-BSE micrograph of a cross-section of alloy APMT exposed for 1000 hours at 700 °C.

The microstructure varied around the sample ring and Figure 8.38 shows another area with a much thicker scale that consisted of several consecutive layers after 1000 hours at 700 °C.
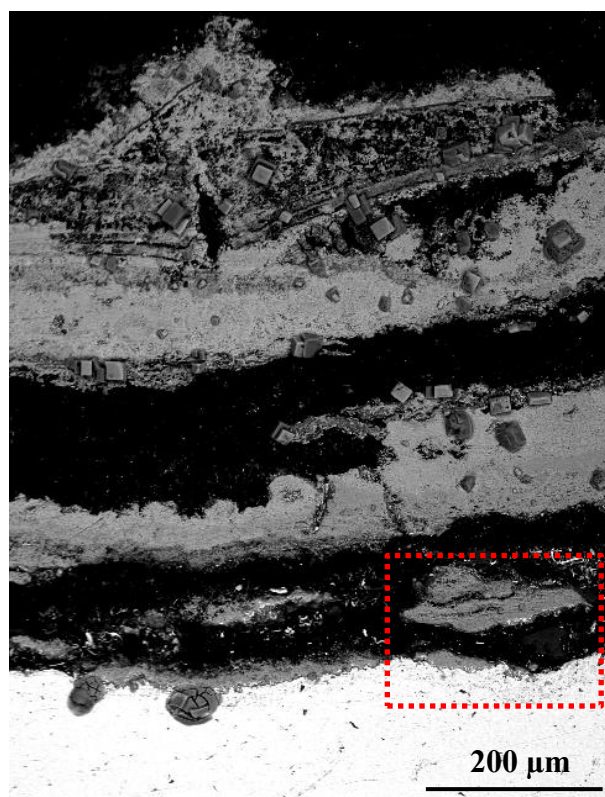
Figure 8.38 SEM-BSE micrograph of a cross-section of pre-oxidized alloy APMT (24 hours, 1100 °C) exposed for 1000 hours at 700 °C.

It is suggested that the oxide scale in Figure 8.37 corresponds to the most recently formed oxide layer seen in Figure 8.38 at the alloy/oxide interface. The boxed area in Figure 8.38 was further analysed in Figure 8.39. The SEM/EDX elemental map for sulphur in Figure 8.39 shows that sulphur was enriched at the alloy/oxide interface and also in the boxed area at the bottom of the spalled oxide lump. It is suggested that transition metal sulphides or sulphates had formed at the oxide/alloy interface and weakened the adherence of the oxide scale, which lead to spallation. Minor amounts of metal chlorides were also detected at the scale/alloy interface at 700 °C. The degree of alloy chlorination was much greater at 600 °C than at 700 °C. This can be explained by the high vapour pressure of transition metal chlorides at 700 °C.

It is suggested that a somewhat protective oxide scale had formed after exposure in the boiler at 600 and 700 °C. This oxide scale is similar to the one formed in the presence of KCl at 600 °C (Fig. 8.17). The scale was layered with an iron-rich top

73

part, a chromium-rich middle part and an aluminium-enriched oxide closest to the alloy substrate.

Poor scale adhesion is suggested to be due to the extensive formation of transition metal chloride along with the formation of metal sulphide/sulphate formation at 600 °C in the boiler. Poor scale adhesion at 700 °C is mainly attributed to formation of metal sulphide/sulphate at the alloy/oxide interface.
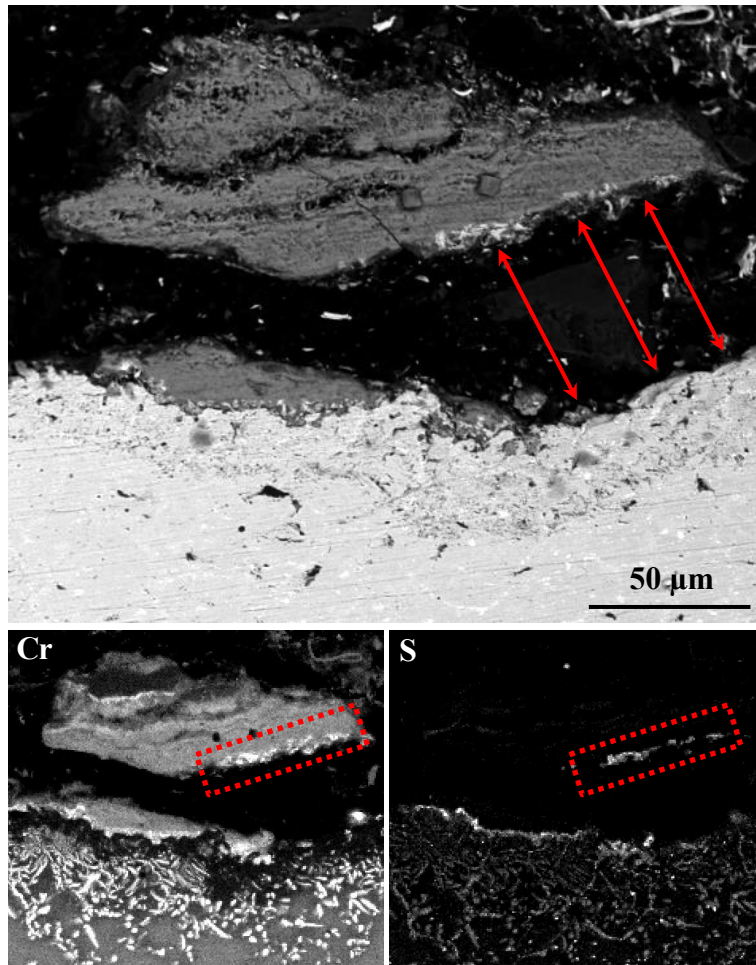
Figure 8.39 SEM-BSE micrograph and EDX elemental maps of a cross-section of pre-oxidized APMT (24 hours, 1100 °C) exposed for 1000 hours at 700 °C.

9 Conclusions

The investigated FeCrAl alloys formed protective oxide scales in both O_2 and $O_2 + H_2O$ in the absence of alkali salt at 600-1100 °C. The oxidation was slightly accelerated in the presence of water vapour at all temperatures. The FeCrAl alloys formed aluminium-rich oxide scales at 600 and 700 °C, and no crystalline forms of aluminas were detected after exposures. Oxidation at 900 and 1100 °C resulted in a two-layered α-Al_2O_3 scale with chromia-rich particles in the interface between the inward- and outward- grown alumina. α-Al_2O_3 was detected after only 1 hour at both 900 and 1100 °C, and no metastable aluminas were detected. The effect of water vapour was only initial, thus oxide growth was initially faster in $O_2 + H_2O$ than in the O_2 environment at both 900 and 1100 °C. The faster initial oxidation in the presence of water vapour resulted in that a protective oxide scale formed faster, and a slower oxidation kinetics was observed earlier in $O_2 + H_2O$ than in O_2, both at 900 and 1100 °C. The effect of water vapour on the early oxidation kinetics was attributed to water acting as an oxidant at the scale gas interface, simultaneously with O_2.

KCl strongly accelerated the corrosion of the investigated FeCrAl alloys in O_2 and $O_2 + H_2O$ environments at 600 °C. The protective aluminium-rich oxide formed in the absence of KCl was replaced with a rapidly growing oxide scale dominated by iron and chromium when KCl was present. In the $O_2 + H_2O$ environment, chromia in the scale reacted rapidly, forming K_2CrO_4 and gaseous HCl. The formation of chromate depleted the protective scale in Cr, thus triggering the formation of a fast-growing iron-rich scale. Iron oxide grew both inward and outward, on either side of the initial oxide in the $O_2 + H_2O$ environment. With time, a chromia layer formed underneath the iron oxide and an aluminium enrichment always occurred closest to the alloy surface. The formation of chromate also occurred in dry O_2, but was slower because only traces of water vapour were present. Alloy chlorination was observed both on top of and below the oxide scale. Alloy chlorination was more pronounced in dry O_2 than in $O_2 + H_2O$. This was because chromate formation rapidly consumed KCl in the latter environment. Thus, KCl will be present on the surface for a longer time in the dry O_2 environment, resulting in a higher degree of alloy chlorination. It is proposed that the chlorination reaction is electrochemical, involving the migration of chloride ions in the grain boundaries of the scale. The greater alloy chlorination in the dry

environment resulted in the formation of a porous and multi layered oxide scale with poor adhesion to the alloy substrate.

Pre-oxidizing the FeCrAl alloys increased their resistance to alkali-induced corrosion at 600 °C. The pre-formed Al-rich/α-alumina scales were, however, unable to protect the alloy against corrosion when subjected to repeated exposure to KCl in an O_2 +H_2O environment at 600 °C. Corrosion was initiated at flaws in the pre-formed alumina scales; the alumina was protective in itself. Consequently, KCl-induced corrosion started locally, and, subsequently, spread laterally over the sample surface. Corrosion can be explained by an electrochemical mechanism by which transition metal chloride forms at the scale/alloy interface and K_2CrO_4 forms at the scale/gas interface. The electrochemical process is conditioned by the presence of a flaw in the scale that allows KCl to penetrate the alumina scale, putting the scale/gas and scale/alloy interfaces into electrochemical contact. KCl acts as an electrolyte that transports chloride ions from the scale/gas interface to the alloy. The formation of transition metal chloride is associated with a large expansion in volume which causes de-cohesion of the scale/alloy interface and scale cracking. The alloy substrate becomes exposed to the gas environment after de-cohesion due to the formation of the transition metal chloride, and this results in the rapid growth of iron-rich oxide below the alumina layer. The associated expansion in volume contributes to alumina scale cracking.

Exposures of alloy APMT with and without pre-oxidation in a waste-fired boiler showed good correlation with the laboratory results. The pre-formed alumina scales failed after only 24 hour of operation in the boiler at metal temperatures of 600 and 700 °C. The alumina scale had only an initial beneficial effect, the alloys corroded in a similar way after the initial stage. A layered iron, chromium-rich oxide scale formed which was enriched in aluminium at the bottom. Transition metal chlorides and metal sulphides or sulphates were enriched at the scale/alloy interface, leading to reduced adhesion of the oxide scales. The degree of alloy chlorination was higher at 600 °C than at 700 °C. The FeCrAl alloy performed well if compared to the FeNiCr alloy Sanicro 28, with about 2-4 times less metal loss at both 600 °C and 700 °C. The oxide scale was denser and more aluminium-rich at 700 °C than at 600 °C. Consequently, higher exposure temperatures in the waste-fired boiler might be favourable in order to establish a more corrosion resistant oxide scale.

76

10 Acknowledgements

11. References

1. H. P. Michelsen, F. Frandsen, K. Dam-Johansen and O. H. Larsen, Fuel Processing Technology **54**, 95 (1998).
2. B. Sander, Biomass and Bioenergy **12**, 177 (1997).
3. L. L. Baxter, T. R. Miles, T. R. Miles Jr, B. M. Jenkins, T. Milne, D. Dayton, R. W. Bryers and L. L. Oden, Fuel Processing Technology **54**, 47 (1998).
4. R. L. Bain, R. P. Overend and K. R. Craig, Fuel Processing Technology **54**, 1 (1998).
5. B. M. Jenkins, L. L. Baxter, T. R. Miles Jr and T. R. Miles, Fuel Processing Technology **54**, 17 (1998).
6. H. Kassman, J. Pettersson, B.-M. Steenari and L.-E. Åmand, Fuel Processing Technology **105**, 170 (2013).
7. P. Viklund, A. Hjörnhede, P. Henderson, A. Stålenheim and R. Pettersson, Fuel Processing Technology **105**, 106 (2013).
8. M. Montgomery and A. Karlsson, Materials and Corrosion **50**, 579 (1999).
9. F. Frandsen, H. Nielsen, P. Jensen, L. Hansen, H. Livbjerg, K. Dam-Johansen, P. B. Hansen, K. Andersen, H. Sørensen, O. Larsen, B. Sander, N. Henriksen and P. Simonsen, *Deposition and Corrosion in Straw- and Coal-Straw Co-Fired Utility Boilers*. (Springer US, 1999).
10. H. Asteman, J.-E. Svensson, M. Norell and L.-G. Johansson, Oxidation of metals **54**, 11 (2000).
11. C. Pettersson, L.-G. Johansson, J.-E. Svensson and Oxidation of metals **70**, 241 (2008).
12. S. Karlsson, J. Pettersson, L.-G. Johansson and J.-E. Svensson, Oxidation of metals **78**, 83 (2012).
13. M. Halvarsson, J. E. Tang, H. Asteman, J.-E. Svensson and L.-G. Johansson, Corrosion Science **48**, 2014 (2006).
14. Y. S. Li, Y. Niu and M. Spiegel, Corrosion Science **49**, 1799 (2007).
15. Y. S. Li, M. Sanchez-Pasten and M. Spiegel, Materials Science Forum **461-464**, 1047 (2004).
16. F. Liu, J. E. Tang, T. Jonsson, S. Canovic, K. Segerdahl, J.-E. Svensson and M. Halvarsson, Oxidation of Metals **66**, 295 (2006).
17. P. Kofstad, *High Temperature Corrosion*. (Elsevier Applied Science Publishers Ltd, London and New York, 1988).
18. D. J. Young, *High Temperature Oxidation and Corrosion of Metals*. (Elsevier, Amsterdam, The Netherlands, 2008).
19. R. Prescott and M. J. Graham, Oxidation of metals **38**, 233 (1992).
20. D. P. Whittle and J. Stringer, Philosophical Transactions of the Royal Society A **295**, 309 (1980).
21. N. Birks and G. H. Meier, *Introduction to High Temperature Oxidation of Metals*, 2. ed. ed. (Cambridge: Cambridge University Press 2006).
22. A. S. Khanna, *Introduction to High Temperature Oxidation and Corrosion*. (ASM International, Materials Park, OH, USA, 2002).
23. W. H. Gitzen, *Alumina as a Ceramic Material*. (John Wiley Sons, 1970).
24. M. J. Bennet, R. Newton, J. R. Nicholls, H. Al-Badairy and G. J. Tatlock, Materials Science Forum **461-464**, 463 (2004).
25. J. Stringer, B. A. Wilcox and R. I. Jaffee, Oxidation of Metals **5(1)**, 11 (1972).
26. F. H. Stott, G. C. Wood and J. Stringer, Oxidation of metals **44**, 113 (1995).
27. G. Berthomé, E. N' Dah, Y. Wouters and A. Galerie, Materials and Corrosion **56**, 389 (2005).
28. G. J. Tatlock, H. Al-Badairy, M. J. Bennett, R. Newton, J. R. Nicholls and A. Galerie, Materials Science and Technology **21**, 893 (2005).
29. J. R. Nicholls, M. J. Bennett and R. Newton, materials at high tempertaures **20**, 429 (2003).

30. H. Josefsson, F. Liu, J. E. Svensson, M. Halvarsson and L. G. Johansson, Materials and Corrosion **56**, 801 (2005).
31. W. J. Quadakkers and L. Singheiser, Material Science Forum **369-372**, 77 (2001).
32. B. A. Pint, in Proc. John Stringer Symposium on High Temperature Corrosion, edited by P.T. Tortorelli, I.G. Wright and P.Y. Hou, ASM International, Materials Park, OH, pp. 9-19, 9 (2003).
33. P. Y. Hou, Materials Science Forum **696**, 39 (2011).
34. S. Chevalier, Materials and Corrosion **65**, 109 (2014).
35. B. A. Pint, A. J. Garratt-Reed and L. W. Hobbs, Materials at High Temperatures **13**, 3 (1995).
36. P. Y. Hou, Journal of the American Ceramic Society **86**, 660 (2003).
37. J. P. Buban, K. Matsunaga, J. Chen, N. Shibata, W. Y. Ching, T. Yamamoto and Y. Ikuhura, Science **311** (2006).
38. I. Milas, B. Hinnemann and E. A. Carter, Materials Research **23**, 1494 (2008).
39. P. Y. Hou, Materials Science **19**, 577 (2000).
40. A. W. Funkenbusch, J. G. Smeggil and N. S. Bornstein, Metallurgical Transactions A **16A**, 1164 (1985).
41. D. G. Lees, Oxidation of metals **27**, 75 (1987).
42. G. Lai, *High Temperature Corrosion And Materials Application*. (ASM International, 2007).
43. H. Asteman, Svensson, J. E., Norell, M., Johansson, L. G., Oxidation of metals **54**, 11 (2000).
44. F. Liu, H. Josefsson, J. E. Svensson, L. G. Johansson and M. Halvarsson, Materials at High Temperatures **22**, 521 (2005).
45. H. P. Nielsen, F. J. Frandsen, K. Dam-Johansen and L. L. Baxter, Progress in Energy and Combustion Science **26**, 283 (2000).
46. H. J. Grabke, E. Reese and M. Spiegel, Corrosion Science **37**, 1023 (1995).
47. C. Pettersson, L. G. Johansson and J. E. Svensson, Oxidation of metals **70**, 241 (2008).
48. C. Pettersson, J. Pettersson, H. Asteman, J. E. Svensson and L. G. Johansson, Corrosion Science **48**, 1368 (2006).
49. J. Pettersson, C. Petersson, H. Asteman, J. E. Svensson and L. G. Johansson, Materials Science Forum **461-464**, 965 (2004).
50. A. Zahs, M. Spiegel and H. J. Grabke, Corrosion Science **42**, 1093 (2000).
51. B. Jönsson, R. Berglund, J. Magnusson, P. Henning and M. Hättestrand, Materials Science Forum **461-464** 455 (2004).
52. B. Jönsson, Q. Lu, D. Chandrasekaran, R. Berglund and F. Rave, Oxidation of metals **79**, 29 (2013).
53. I. M. Watt, *The principles and practice of Electron Microscopy 2nd edition*. (Cambridge University press, 1997).
54. J. Goldstein, *Scanning Electron Microscopy and X-Ray Microanalysis*, Third Edition ed. (Springer US, 2003).
55. D. B. Williams and C. B. Carter, *Transmission Electron Microscopy*, 2nd ed. (Springer, New York, 2009).
56. H. Asteman, R. Norling, J.-E. Svensson, A. Nylund and L. Nyborg, Surface and Interface Analysis **34**, 234 (2002).
57. R. Jenkins and R. L. Snyder, *Introduction to X-ray Powder Diffractometry*. (John Wiley & Sons Inc, 1996).
58. H. Asteman and M. Spiegel, Corrosion Science **50**, 1734 (2008).
59. S. Canovic, J. Engkvist, F. Liu, H. Lai, H. Götlind, K. Hellström, J.-E. Svensson, L.-G. Johansso, M. Olsson and H. Halvarsson, journal of the electrochemical society **157**, C223 (2010).
60. T. M. Besmann, N. S. Kulkarni and K. E. Spear, Journal of the American Ceramic Society **89**, 638 (2006).

61.   F. Liu, H. Götlind, J.-E. Svensson, L.-G. Johansson and M. Halvarsson, Corrosion Science **50**, 2272 (2008).
62.   T. Åkermark and G. Hultqvist, Oxidation of metals **47**, 117 (1997).
63.   J. Pettersson, J. E. Svensson and L. G. Johansson, Oxidation of metals **72**, 159 (2009).
64.   P. Viklund and R. Pettersson, Oxidation of metals **76**, 111 (2011).